Prototype of real-time monitoring system for dynamic line rating

Electrical Shielding and Communication verification

G.J. van Raamsdonk

TUDelft
Delft
University of
Technology

Challenge the future

Prototype of real-time monitoring system for dynamic line rating

ELECTRICAL SHIELDING AND COMMUNICATION VERIFICATION

by

G.J. van Raamsdonk

to obtain the degree of Master of Science in Electrical Engineering

at the Delft University of Technology,
in collaboration with Siemens Expert Center High Voltage,

to be defended publicly on Wednesday November 17, 2017 at 10:30 AM

An electronic version of this thesis is available at http://repository.tudelft.nl/.

*TU*Delft Delft University of Technology   SIEMENS

ABSTRACT

The load of the electric grid in increased by the connection of more renewable energy sources and less controlled power stations. The transmission operator has to decide where and when new overhead lines are required. However the operator can also chose to utilize existing lines more by increasing the transport capacity. This can be accomplished by applying dynamic line rating. In this case the conductor temperature and sag will increase but should not not violate the safety limits. Therefore a device can be installed on overhead lines to monitor the temperature and sag in real-time. Several devices are already manufactured and tested. However these devices require a reliable communication.

In this thesis the feasibility and reliability of communication with Low Power Wide area Network (LoRaWAN) protocol in an overhead line environment is studied. The first objective is to determine the consequences of DLR on overhead lines. Second shielding of the electric and magnetic field in an overhead line is evaluated. Finally an antenna is chosen and a prototype is designed to evaluated its thermal behavior, low frequency magnetic shielding capabilities and communication feasibility and reliability.

The first objective is to understand how the conductor temperature, the sag and magnetic field increases in respect to the transport capacity. The change in conductor temperature is examine by considering several heating gains and losses mechanisms. The sag is approached by a sagging and parabola curve to evaluate the decrease of distance to the ground. The maximum magnetic field is determined for close distances from the conductor.

Two methods are examine to shield form the electric and magnetic field from the overhead lines. Therefore the materials copper, aluminum, steel and mu-metal are evaluated on their conductivity and permeability. The antenna is determined by comparing a dipole, loop and slot antenna on their complexity and expected radio noise interference. The prototype is exposed to a test setup in which the surface temperature, and magnetic field, is measured. The reliability of communication is evaluated by analyzing the amount of send and received packages.

In case of an increased transport capacity the conductor temperature of an overhead line mostly increase by Joule heating. For a conductor temperature increase and concentrated weight the sag increases with negligible tents of centimeters. The maximum magnetic field was calculated and resulted in a required shielding effectiveness. The thickness of shield was determined for each material to reduce the magnetic field inside an enclosure. A slot antenna was designed and made in the prototype and compared with simulations in respect to the reflection coefficient. The surface temperature of the prototype did barely gain heat by the generated induced currents. However the prototype does reduce the magnetic field inside and confirms the theory of low frequency magnetic shielding. Furthermore the communication is tested and resulted in reliable data transfer in the case of a 0.5 cm distant from the conductor through which a current of 800 A flow. Furthermore corona discharges were generated up to 130 kV in which data still was transferred successfully.

ACKNOWLEDGMENTS

This thesis is written for the completion of the Master of Science in Electrical Engineering at Delft University of Technology. The research was in collaboration with the department of DC systems, Energy conversion & Storage at TU Delft and with Siemens Energy Management division in Amersfoort.

I would like to thank several people who helped me achieving this degree. First my supervisor from Siemens B. Brand who steered my focus back to the problems I should solve. I am also grateful for the help of Ir. J. Langedijk who saw my potential inside Siemens. I hope for his quick recovery.

Furthermore I would like to thank the technical staff of the High Voltage Laboratory. In collaboration with these technicians I was able to perform the test. They where very helpful by building up the test setup, asking critical questions and soldering several other prototypes.

Last but definitely not least I would like to thank my mother, farther and sister who saw my struggle through the thesis but were always able to cheer me up and motivate me to press forward.

The journey to thesis defense was long and hard. But when I look back to the progress I made and the people I met and I expect a exciting and bright future.

Gert-Jan van Raamsdonk

Spijkenisse, 17th November 2017

"When you can measure what you are speaking about and express it in numbers you know something about it, but when you cannot measure it, when you cannot express it in numbers your knowledge is of merge and unsatisfactory kind; it may be the beginning of knowledge but you scarcely processed in your thoughts to the stage of science whatever the matter may be."

Sir William Thomson

Glasgow, 21th December 1888

CONTENTS

LIST OF FIGURES

LIST OF TABLES

1

INTRODUCTION

Contents

This chapter provides the background information of the thesis. First the motivation to research dynamic line rating is given in section 1.1. Secondly the chosen objectives are explained in section 1.2 and lastly the structure of the thesis is discussed in section 1.3.

1.1. MOTIVATION

For the motivation of the thesis the necessity of dynamic line rating will be explained by highlighting two decisions which are published in the Energy-Agreement: *grow to sustainability* [2] in September 2013. This agreement describes an alteration of electricity generation. As last part of the motivation the method of line rating is explained.

The Energy-Agreement has been published to combine the interests and willingness of multiple organizations to increase the Dutch sustainability in respect with society and the economy. Organizations from five different sectors can be identified: non-governmental organizations, industry organizations, government, energy organizations, employer/employee organizations and financial institutions. The motivation of this collaboration brings also improvement in their export expansion, employment growth and competitive position in the long term. To increase the sustainability targets are set. The following two targets of the Energy-Agreement are in regarding to this thesis:

- Reduction of CO_2 emission by 80 to 95 % in 2050 compared to the emission of 1990.

Plant	Year (closed)	Power
Willem Alexander	1994 (2013)	253 MW
Borssele	1988 (2015)	406 MW
Amercentrale 8	1981 (2016)	645 MW
Gelderland 1	1985 (2016)	570 MW
Maasvlakte 1	1988 (2017)	500 MW
Maasvlakte 2	1989 (2017)	500 MW
Hemweg	1995	630 MW
Amercentrale 9	1994	600 MW
Maasvlakte	2015	800 MW
Maasvlakte 3	2016	1.070 MW
Eemshaven	2015	1.560 MW

Table 1.1: The opening (closing) of coal plants in the Netherlands [1]

Figure 1.1: Location coal plants [1]

- The percentage of electricity generation by renewable sources has to be increased to from 4 % in 2013 to 14 % in 2020 and to 16 % in 2023.

CO_2 EMISSION

In the Energy-Agremeent of 2013 the deceision was made to close the coals plants which were build before 1990. These plants have a low efficiency to generate electricity from fossil fuel and have a high CO_2 emission. In the beginning of 2016 and in July of 2017 five coal plants were put out of operation. These coal plants had a efficiency of around the 38 %. The remaining coal plants from the nineties have around 42 %, while the new plants are 46 % efficient [1]. The coal plants which are closed down or are in operation can be seen table 1.1 and figure 1.1.

Coal plants have the highest CO_2 emission rate compared to sources from fossil fuel. The three remaining coal plants with the highest efficiency have an emission rate of 740 to 910g/kWH. Compared to gas plants which has a CO_2 emission rate of 396 g/kWH and with co-generation of heat even 298g/kWh [?].

Regarding the power of the closed power plants a total capacity of 2.621 MW was shut down. The remaining installed plants are able generate 4.660 MW. However to achieve the reduction of CO_2 emission it is currently discussed to close the remaining coal plants as well. Without compromising the supply of electricity the removed capacity has to be transported from another source in the Netherlands or imported from the neighboring electric grids.

RENEWABLE ENERGY SOURCES

As part to reach the second target it is stated in the Energy-Agreement electricity generation by offshore wind energy has to be increased to a capacity of 4.450 MW in 2023. At the time of publication of the Energy-Agreement around 1.000 MW was generated by windmills offshore[2].

The transmission system operator (TSO) of the Netherlands has the responsibility to establish the grid connection from the offshore wind area to the Dutch high voltage grid. The TSO is building five platforms with each carries a 700 MW offshore AC substation which are connected by 66 kV cables to the wind turbine sites. Cables with a voltage level of 220 kV will connect the offshore substation to substation on land in which the voltage level is converted to 380 kV of the high voltage grid [3]. The first platform is planned to be in operation in 2019. In figure 1.2 the five locations of the platforms are visualized.

The TSO has planned to install 3.500 MW of capacity by offshore wind energy. However windmills generate a certain level of electricity depending on the wind speed. A minimum is necessary to start turning the blades, a certain speed provides the maximum output and maximum speed is defined before damage can be inflicted to the turbine. In case the wind speed is to low no electricity can be generated from offshore wind energy and has to be transported from another source.

Name	Year	Power
Borssele Alpha	2019	700 MW
Borssele Beta	2020	700 MW
Hollandse Kust Zuid Alpha	2021	700 MW
Hollandse Kust Zuid Beta	2022	700 MW
Hollandse Kust Noord	2023	700 MW

Table 1.2: Offshore wind substations

Figure 1.2: Location wind farms and substations

TRANSITION TRANSPORTATION

Closing the coal plants and increasing offshore wind energy are two examples which shows the transition of electricity generation in the Netherlands. Electricity has to be transported from another source to secure the need of supply. In respect to the coal plants the Energy Research Center of the Netherlands (ECN) and the TSO concluded that the closure will be provided by gas plants and imported from other countries [1]. The electric grid including the coal open coal plants and the offshore wind substations can be seen in appendix **??**. This re-route of transmission capacity increases the load on other transmission lines to a level they were not designed to. The asset manager of the grid owner has the following possibilities in regards of overhead lines [4]:

- Uprating: increase of thermal or voltage rating

- Upgrading: improvement of reliability in structural or electrical performance

- Refurbishment: complete structural replacement

- Expansion: install new transmission lines

In regarding of this thesis the method of **uprating in thermal ratings** will be used to increase the transmission capacity. There are many methods to increase the thermal rating. Replacement of the conductor to increase conductivity area or installing high temperature conductors are methods of thermal rating increase. However here an **real-time monitor system** will be designed to increase the transmission capabilities.

The monitoring device allows to utilize the existing grid better. Without real time measurement data assumptions are made to minimize the risk of exceeding the designed temperature. These assumptions are based on the probability of a worst case scenario and will be described in more detail in the next chapter. Regardless an overhead line operates rarely operates in the worst case scenario. Therefore additional capability can be used. The maximum capacity which is assumed under the worst case scenario is called static rating and can be seen in orange in figure 1.3, remained risk in red and the additional available capability which can be used when a real time monitoring is used in green.

Installing of a real time monitoring system allows to improve the thermal rating. Utilizing otherwise unused capacity prevents expensive upgrades or installation of additional overhead lines. Furthermore, improvements in measurement sensors and communication possibilities only makes real time monitoring possible since the last decade [5].
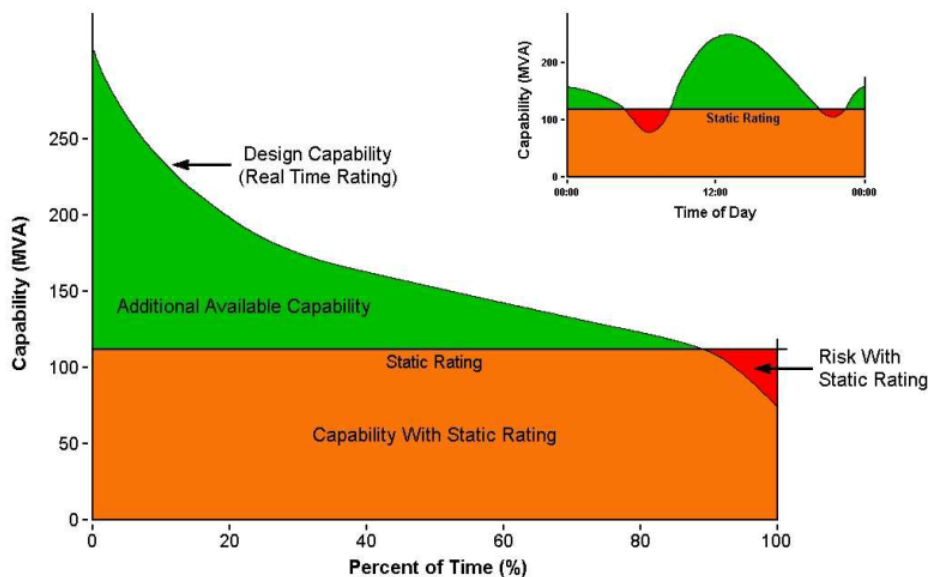
Figure 1.3: Transmission capability by static and real time rating [4]

1.2. THESIS GOAL AND OBJECTIVE

The previous section explained the motivation to develop a real-time monitoring system on a overhead line. In this section the thesis goal and objectives are defined.

The main goal of this thesis is to examine if a Low Power Wide Area Network can function in an overhead line environment for dynamic line rating applications. The main objective is to design a prototype as real-time monitoring system which can validate the reliability.

1.2.1. THESIS GOALS

To design a real-time monitoring system the device requires at least an energy supply, measurement equipment, antenna and an enclosure. Each part can be used to fill an entire thesis study. Therefore several goals are set which will be answered during this thesis:

- What parameters are used at the moment to determine static and dynamic line rating and which real-time monitoring system can be applied?

- What are the consequences of dynamic line rating for the heat balance of the conductor and the sag of the overhead line?

- How can the electronics be protected from the low frequency magnetic shield?

- Which antenna can operate and how does a prototype perform in an overhead line environment?

1.2.2. THESIS SCOPE

The scope of this thesis is limited in designing a prototype by the following aspects.

First the maximum magnetic field from the conductor is determined at **distant of 5 cm and only consider 50 Hz**. Lightning strikes and short circuit events results in an impulses with high magnetic field (as result of the current). These faults result in high induced voltages inside the prototype and can damage or destroy the electronics. Exact calculations with these impulses can become very extensive and can only conclude of the electronics survive or not.

Second the **maximum magnetic field inside the prototype is set** to be $10\,\mu T$. Reducing the external maximum magnetic field to this value provides insight on the feasibility of shield thicknesses.

Third the used **communication protocol operate at 868 MHz**. Other communication methods are not considered. However then antenna will be designed in order on this operation frequency in order to transmit data.

Four the **prototype is simplified** in order to validate the feasibility and reliability of the communication. A prototype with a designed energy supply, measurement equipment and enclosure will taken to much time and resources. Electronics with a temperature sensor and a by rectangular steel box will be used test validation.

Last the **thermal calculations on the heat transfer between the conductor and the prototype are omitted**. The real-time monitoring device will be connected on the overhead line. The prototype does not consist of a mechanical part which is in contact with the line.

1.3. Thesis Structure

The previous section discussed the objectives and scope of the thesis. The following section provides a short description of every chapter.

Chapter 2: In chapter 2 the line rating methods is discussed by comparing with a static and dynamic. The type of sensors in order to apply dynamic line rating are discussed.

Chapter 3: In chapter 3 the heat gains and losses mechanisms of a conductor are studied. The equations are evaluated to provide an understanding of their origins.

Chapter 4: In chapter 4 the curve of the conductor which is made between two supporters is examine. The effect on the sag in case of a temperature increase and extra weight on the conductor are determined.

Chapter 5: In chapter 5 the magnetic field at 5 cm below the conductor is determined. Furthermore the required shielding effectiveness to reduce the field to 10 μT.

Chapter 6: In chapter 6 the theory of shielding is studied. Equations to determine the shielding effectiveness analytic are discussed. Furthermore the thickness of several materials are analyzed to provide shielding

Chapter 7: In chapter7 several antenna topologies are discussed. The dimensions and effect of the slot antenna are determined.

Chapter 8: In chapter 8 the prototype is tested with the setup of Appendix A. Here the thermal behavior of the conductor and prototype, shielding effectiveness, antenna characteristics and communication reliability are analyzed.

Chapter 9: In chapter 9 the conclusions and recommendations are provided.

Appendix A: In Appendix A the test setup is described. Furthermore an analysis of two loops are tested in order to lower the inductance.

Appendix B: In Appendix B several equations are derived. First the solution of the sagging curve, the shielding factor of the impedance method and the shielding effectiveness form the separation of variable method.

Appendix C: In Appendix C figures of the prototype and stainless steel plate are shown under the corona discharge test.

Appendix D: In Appendix D used matlab scripts are shown for the sagging curve and the simulated slot antenna. To simulate the antenna matlab Antenna Toolbox is required.

2

LINE RATING CONCEPTS

Contents

In the previous chapter the motivation to research dynamic line rating was explained. This chapter describes which parameters are used to determine the static and real-time line rating.
First section 2.1 discus the assumptions of static line rating. Second dynamic time line rating will be compared in section 2.2 and describes the indirect and direct monitoring systems in section 2.2.1 and 2.2.2 respectively.

2.1. STATIC LINE RATING

The static line rating can be applied to any overhead line to determine the maximum electrical current through the conductor which ensures safe use under the worst case scenario. Safely use is defined if there is a minimum probability which can violate the **minimum electric clearances** and **maximum conductor temperature**. The minimum clearances is defined as the smallest distance form the ground to the line. Furthermore the distance between two supporters is defined as span length and can be seen in figure 2.1. The vertical distance from the span to any point in the line is the sag. Most of the time the sag is maximum in the middle from the span. When the sag increases the clearance distance decrease. This happens in case the conductor temperature increase by an increase of electrical load through the conductor or when weather conditions changes.
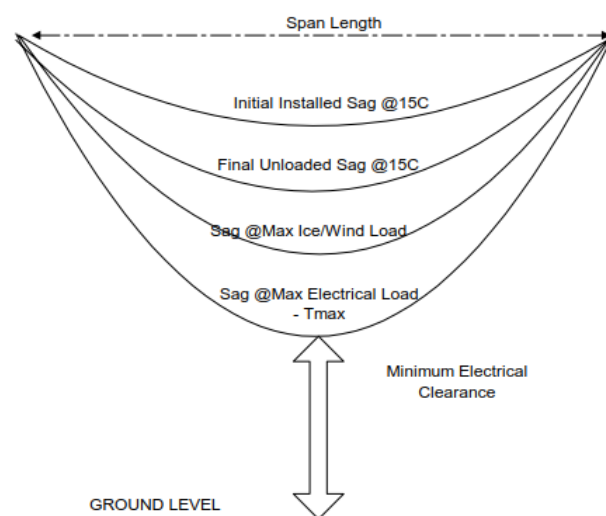
Figure 2.1: The sag between two pylons can variate [6]

However in case of static line rating the weather conditions are fixed atmospheric parameters which determine the electrical current. The parameter define the worst case scenario. The following subsections explain the fixed parameters.

AMBIENT TEMPERATURE

First the ambient temperature should be chosen as the annual maximum along the line. The ambient temperature influence how much the conductor can radiate his heat too its surrounding atmosphere. For the Netherlands the TSO has set the ambient temperature to 30 °C [7]. By allowing the conductor temperature to maximum of 100 °C the thermal current rating can be chosen for each ambient temperature. With figure 2.2 the thermal current which heats up the conductor to maximum 100 °C is approximately 1150 A at an ambient temperature of 30 °C. From the figure it can be concluded that the ambient and the conductor temperature have a linear relation up to 40 °C. However at higher ambient temperatures the conductor can transfer its heat less to his surroundings.

WIND SPEED & DIRECTION

Second an effective wind speed of 0.6 ms^{-1} is used. The effective wind speed is determined from the direction in case the wind is orthogonal to the conductor. In calculations of the effective wind the vertical component of the wind is small and is in most times neglected [7]. Cooling the conductor by movement like the wind is forced convection.

SOLAR RADIATION

Third the solar radiation intensity is set to 1000 Wm^{-2}. The radiation intensity is assumed in the case no clouds and at the time time the sun is at its highest. Thereby the conductor absorptivity is included, which is set to 0.8 and is the last parameter for static line rating.

Under the atmospheric parameters of the three previous subsections the static thermal current can be calculated. The calculations are defined in IEEE standard 738-2013: *"IEEE standard for calculating the current temperature relationship of bare overhead conductors"*. The heating gains and losses will be examine in the next chapter. The increase of thermal current result in using the conductor to operate to either its maximum conductor temperature or sag [5].
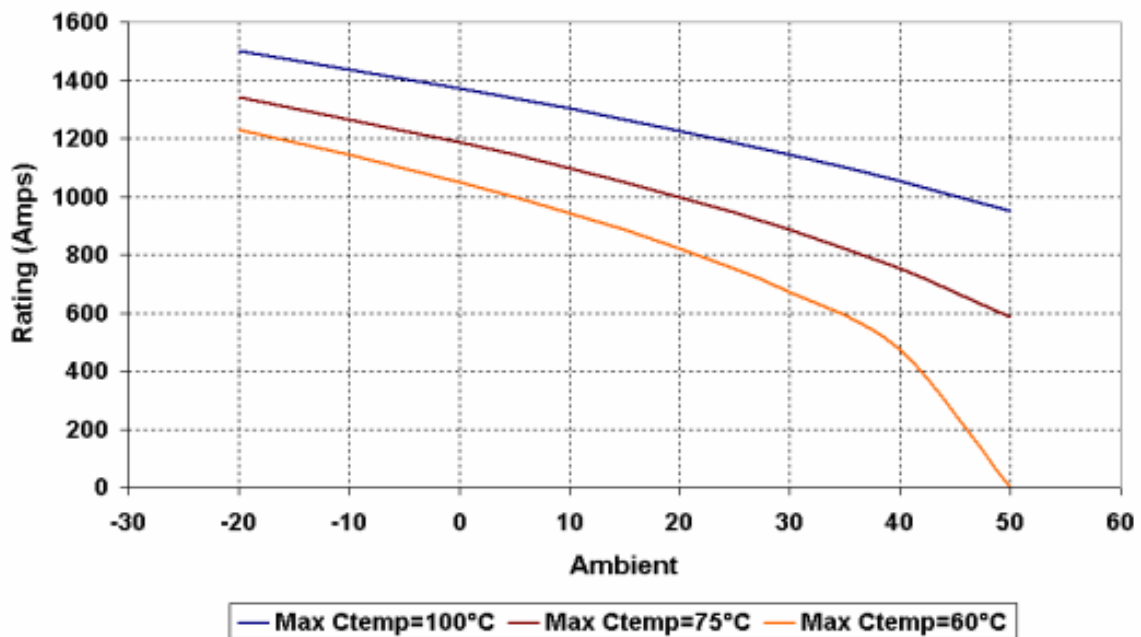
Figure 2.2: The maximum line rating current through the conductor for several maximum conductor temperature versus the ambient temperature. In case the ambient temperature is 50 °C and the maximum conductor temperature is 60 °C the line is put out of use [7].

2.2. Dynamic line rating

In dynamic line rating atmospheric conditions and other parameters are measured in real-time. With these measurements the maximum allowable thermal current through an conductor is determined. This current must not violating the safety limits of the line. The ambient temperature throughout the year is mostly lower than 30 °C. Furthermore an effective wind speed is higher than 0.6 ms^{-1} [8]. Therefore static lines rating allows to utilization more transport capacity.

Dynamic line rating can also be used to diagnose an overhead line. A line consist of several conductors and supporters. The maximum thermal current is determined by the weakest part of the line where the conductor temperature approaches its maximum or when its clearance distant to ground is minimum. Dynamic line rating can identify these critical parts in the line [5].

There are several types of monitoring systems which can measures parameters in real-time to allow dynamic line rating. The monitoring systems are divided by indirect and direct methods. Each methods takes the following features into account:

- Accurate: the measured parameter should consist of a low error margin.

- Precise: to asses the rate of the error.

- Reliable: communicate under severe conditions.

- Frequent: send real-time information multiple times .

- Cost efficient and easy in installation and maintenance.

2.2.1. Indirect monitoring systems

The indirect monitoring systems measure the atmospheric conditions by the use of weather stations. This data is used by a mathematically model in order to simulate the conductor temperature. In the Netherlands the *Royal Netherlands Meteorological Institute* (KNMI) use at least 30 weather stations which automatically measures the wind direction, speed, ambient temperature and solar intensity each ten minutes. The KNMI has installed anemometers on overhead line supporters at a height of 10 m to measure the wind speed and direction accurately [8].

Applying the data from KNMI allows a cheap and easy to use method for dynamic line rating as seen in figure 2.3. Dynamic line rating can be applied directly and reliable. In case a weather station malfunction or fail there are several other stations which can provide information of the weather conditions. However to apply dynamic line rating for low wind speeds ultrasonic anemometers are needed. These devices can measure the wind speed below 1 ms^{-1} [5] [9].
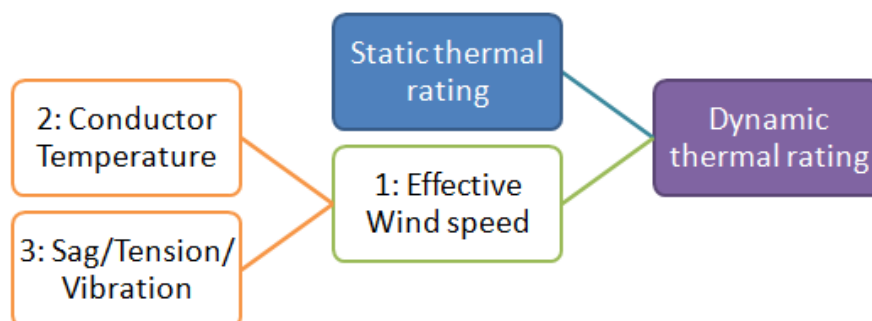
Figure 2.3: Dynamic Line Rating methods by 1: indirect monitoring the weather conditions, 2: direct monitoring the conductor surface temperature and 3: direct monitoring other paramters

2.2.2. Direct monitoring systems

The first direct monitoring systems measures the conductor surface temperature directly from the overhead line. The data can be translated to the wind speed and provides information for the cooling of the overhead line as seen in figure 2.3 [9]. By using temperature sensors on the conductor itself measures the surface temperature. These sensors more accurate than any indirect system but only measured the conductor where the monitoring system is installed. Therefore all the measurements as to be communicated to a central location in order to be processed.

As stated before the atmospheric conditions can vary along the line. Therefore measuring the conductor temperature directly on single location is not sufficient to apply dynamic line rating. Multiple sensors can be used but can become expensive in case of long lines. Fortunately the average conductor temperature can also be determined directly by monitoring the sag, tension or vibration of the overhead line.

Sag monitoring
Monitoring the sag of the line allow to measures the distance between the line and the ground. The monitoring system captures and processes images in order to calculate the sag. This is done by camera on the supporter while the conductor is marked by a target. The sag can be measured accuracy of 15 mm in both vertical as horizontal level [10] .

Tension monitoring
The tension monitoring system measures the average line temperature due to its direct relation with the conductor tension [7]. The conductor tension is measured by installing a load cell between the tower and the insulation string. Therefore the monitoring system is electrical insulated from the conductor. In section 4.1 the influence of an increased tension is analyzed to determine the behavior of the line for dynamic line rating.

Vibration monitoring
The last direct monitoring system is by measuring the line vibration frequency. The conductor vibration frequency are directly related to the sag. The monitoring system is installed on the conductor and has an typical accuracy 10 cm [11].

2.2.3. LIMITATIONS

Applying dynamic line rating requires a combination of **both direct as indirect monitoring system** in order to determine the maximum thermal current. In case only the ambient temperature or the effective wind speed is measured a different result can be obtained as shown in figure 2.4. In [5] the thermal current is determined which allows the conductor to reach 50 °C. Also the line rating current is calculate in case of 80 °C. It is observed for low ambient temperature and effective wind speed the current can be increased much less than in the case for high ambient temperature. The ambient temperature and effective wind speed are non-linear. It is therefore required to measure them both.

In the next chapter the consequences of a higher thermal current is considered by studying the thermal behavior of conductors.

2.3. LINE RATING CONCLUSIONS

To goal of this chapter was to determine the parameters of static line rating and dynamic line rating.

For static line rating fixed weather parameters are used to determine the maximum thermal current which ensures safe operation under the worst case condition. These parameters are the ambient temperature, effective wind speed, solar radiation intensity and absorptivity.

Dynamic line rating use real-time measurements an can be performed directly and indirectly on the overhead line. An indirect monitoring system can predict the coming weather conditions. However they lack the accuracy to inform the TSO for the critical spans real-time. A direct monitoring system can provide this information but is unable to predict the transmission capacity for later time. Therefore a combination of both direct and indirect monitoring systems are required to apply the dynamic line rating.
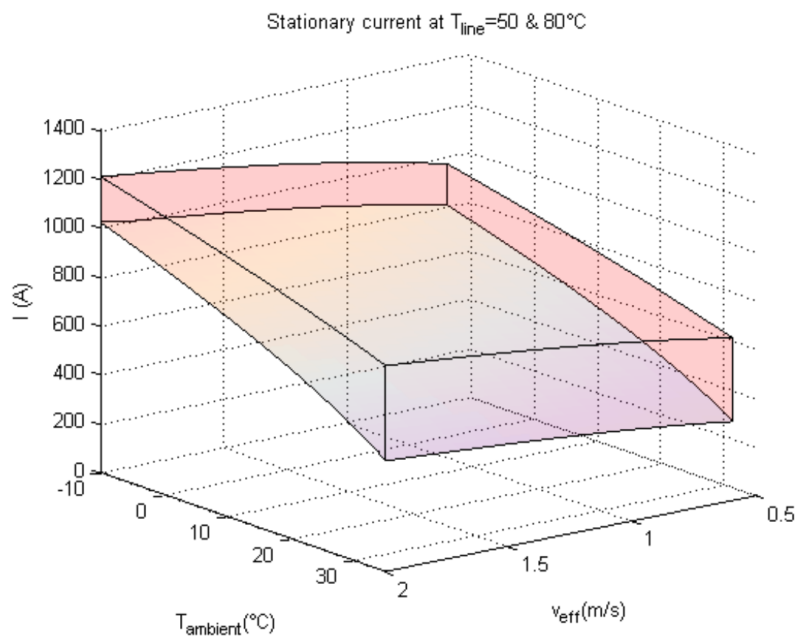
Figure 2.4: The variation of thermal current rating for maximum conductor temperature of 50 °C and 80 °C for different ambient temperatures and effectie wind speeds [5]

OVERHEAD LINE THERMAL CONCEPTS

Contents

In the previous chapter it was explained that the ambient temperature, wind and solar radiation are fixed parameters for static line. However monitoring these parameters allows a higher transport capacity.

The goal of this chapter is to examine the heating gain and loss mechanisms of a conductor to asses the thermal behavior. This also provide information of heating transfer when a real-time monitoring is installed on the overhead line.

First section 3.1 discuss the heat balance of the conductor. Then several heating gain and losses mechanisms are discussed in section 3.1.1 to 3.1.5

3.1. HEAT BALANCE

In order to evaluate the conductor temperature for increased transport capacity the thermal mechanisms are examined. The temperate of the conductor depends first on the physical properties of the conductor, second the weather conditions and last electrical current as can be seen in figure 3.1.
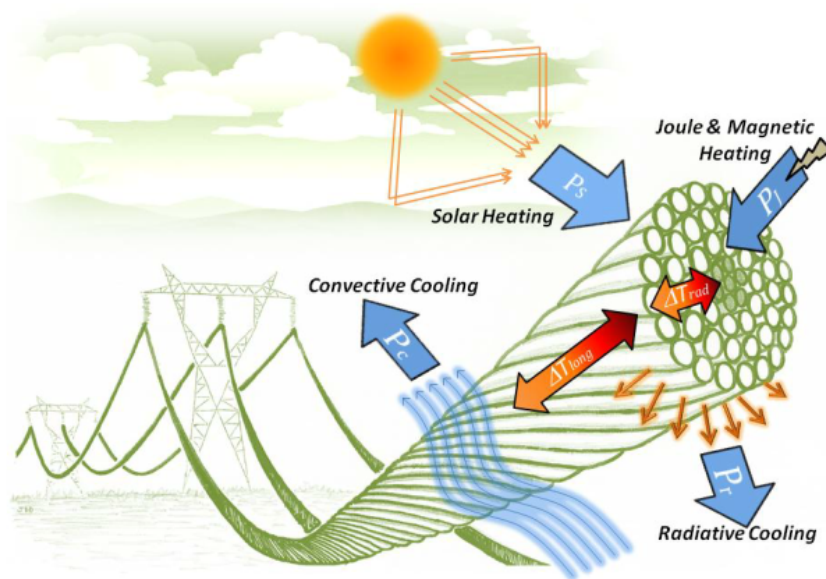
Figure 3.1: Heating and cooling of a conductor on an overhead line [12]

Physical properties can be divided by parameters which stays constant or changes over time. The constant parameters are the conductivity and diameter of the conductor while the surface of the conductor changes by the weather conditions. This influence the emissivity and absorptivity of the conductor. Weather conditions can change by the hour and season, while the the electrical current varies with the power loading and generation [13]. Different thermal models can be used with the three parameters:

- Steady State: weather conditions and electrical current constant for all times. The conductor temperature is a constant. This model is used for static line rating.

- Transient: weather conditions constant and electrical current assumed as a step wave. The conductor temperature changes exponential as seen in figure 3.2. This has a non steady state behavior.

- Dynamic: weather conditions and electrical current changes every time. The change in conductor temperature has to be calculated every time period.

The heat balance for the steady state case can be calculated by equation 3.1, while the non steady transient case with equation 3.2. In here the mechanisms are Joule heating P_j, magnetic heating P_m and solar radiation heating P_s, while the heat is lost by conductive heat loss P_c and radiation heat loss P_r. Furthermore $m \cdot C_p$ is the heat capacity of the conductor, while dT_{avg} is the change in conductor temperature during time steps t. The next sections describes the heating mechanisms.

$$P_j + P_m + P_s = P_c + P_r \quad \text{Steady state heat balance} \tag{3.1}$$

$$P_j + P_m + P_s = m \cdot C_p \frac{dT_{avg}}{dt} + P_c + P_r \quad \text{Non-Steady state heat balance} \tag{3.2}$$
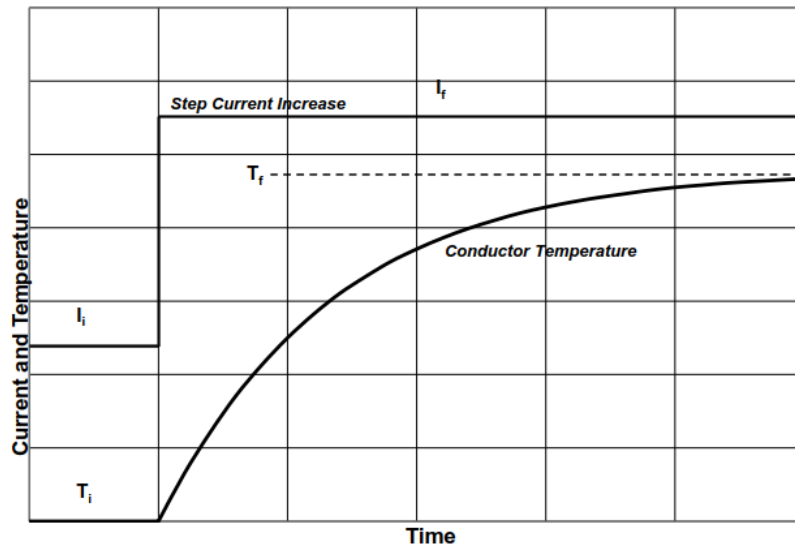
Figure 3.2: Increase of current through the conductor increases the conductor temperature after a certain time period[13]

3.1.1. JOULE HEATING

The first heating mechanism of an overhead line conductor is joule heating. This heating is relate to the current flow through the conductor. The heat gain per unit length by Joule heating is given in equation 3.3.

$$P_j = I^2 \cdot R_{dc} \cdot k_\delta \qquad (3.3)$$

Where I is the current through the conductor, R_{dc} the DC resistance per unit length and k_δ the skin effect factor. Furthermore the R_{dc} depends on resistivity ρ of the material and the cross section of the conductor. For solid cylindrical non-ferrous conductor the resistance is determined by equation 3.4. Furthermore the resistivity depends on the mean temperature of the conductor by equation 3.5.

$$R_{dc} = \frac{\rho}{A} \qquad (3.4)$$

$$\rho = \rho_{20} \cdot [1 + \alpha_{20} \cdot (T - 20) + \zeta_{20} \cdot (T - 20)^2] \qquad (3.5)$$

Where ρ_{20}, α_{20} and ζ_{20} are temperature coefficients form the material at 20 °C. Several coefficients are presented in table 3.1. Furthermore T is the temperature of the material. Equation 3.5 shows the resistivity and the resistance change by temperature which changes non-linear. The skin factor in equation 3.3 takes into account the increased resistance by AC. The skin factor can be calculated by *Bessel functions* or approximated depending on the conductor diameter. The larger the diameter the higher the skin effect factor. Still the skin factor is low (1.02 for normal range of conductor diameters and up to 1.08 for diameter over 45 mm) and will have a small effect on the Joule heating [12].

3.1.2. MAGNETIC HEATING

Aluminum conductors can be reinforced by a steel core. The use of this extra metal is to reinforce the conductor mechanically. However the steel core brings an extra heat gain to the conductor. The alternating current through the conductor spins around the steel core. This produces an alternating magnetic flux density which gains heat by the eddy currents[12]. The magnetic heating gain is given in equation 3.6.

$$P_m = C \cdot A \cdot \gamma \cdot B_{max}^{1.83} \qquad (3.6)$$

Where A is the cross section of the core, B the magnetic flux density, γ the mass density of the steel core and C the pressure at a certain conductor core temperature. Magnetic heating in a single layer conductor cause to increase the resistance by magnetic hysteresis and eddy currents. However the magnetic flux density by the alternating current in the steel core can be nullified. In case of an even number of steel layers the magnetic flux density is canceled and magnetic heating can be neglected [12].

3.1.3. SOLAR HEATING

Another mechanism is solar heating. The sun radiate to the earth and in case there are no clouds it heats up the conductor surface. The heat gain per unit length is given in equation 3.7.

$$P_s = \alpha_s \cdot I_t \cdot D \qquad (3.7)$$

Where α_s the absorptivity of the surface, I_t is solar radiation intensity and D the diameter of the conductor. The absorptivity stands for the radiation which is absorbed by the conductor surface. A perfect black body which absorbs most of the radiation has an absorptivity of one. while a white surface reflects and has a value close to zero. Depending on the environment an old aluminum conductors approach an absorptivity of 0.9, while new aluminum conductors approaches 0.3. In case for the static rating an absorptivity of no less then 0.8 should used.

	$\rho_{20}(\Omega \cdot \text{m})$	$\alpha_{20}(\text{K}^{-1})$	$\zeta_{20}(\text{K}^{-2})$
Copper	$17.24 \cdot 10^{-9}$	$3.9 \cdot 10^{-3}$	$5 \cdot 10^{-3}$
Aluminum	$28.26 \cdot 10^{-9}$	$4.03 \cdot 10^{-3}$	$6 \cdot 10^{-3}$
Galvanized Steel	$191.57 \cdot 10^{-9}$	$4.5 \cdot 10^{-3}$	$8 \cdot 10^{-3}$

Table 3.1: Temperature coefficients at 20 °C to determine the resistivity of conductor material [12]

3.1.4. CONVECTIVE HEAT LOSS

The first mechanism which loss the heat from the conductor is by convection. Convection transfer the heat of the conductor to its surrounding atmosphere through a moving medium. In this case air. Convection can be divide into natural and forced convection depending on the wind speed. Natural convection occurs when the wind speed is below 0.2 ms^{-1}, while forced convection at higher values of wind speed [13]. Heat loss by natural and forced convection are stated in equations 3.8 and 3.9 respectively.

$$P_{c-natural} = 3.645 \cdot \rho_c^{0.5} \cdot D_0^{0.75} \cdot (T_s - T_a)^{1.25} \tag{3.8}$$

$$P_{c-forced} = K_{angle} \cdot 0.754 \cdot N^{0.6} \cdot \lambda_f \cdot (T_s - T_a) \tag{3.9}$$

$$\tag{3.10}$$

Where ρ_c is the air density, D_o the outer diameter of the conductor, T_s the temperature of the conductor surface and T_a the temperature of air. Furthermore N is Reynolds number which is proportional to the conductor outer diameter, wind speed and air's density and dynamic viscosity as in equation 3.11 [13].

The thermal conductivity of air λ_f is stated in equation 3.12. While in the equation of the forced convection K_{angle} indicates the wind direction in respect to the conductor in the angle β and is stated in equation 3.13. The angle of the wind direction has a great effect on the forced convection heat loss as can be seen in figure 3.3.

$$N = \frac{D_0 \cdot \rho_c \cdot v}{\mu_c} \tag{3.11}$$

$$\lambda_f = 2.424 \cdot 10^{-2} + 3.738 \cdot 10^{-5} \cdot (T_s + T_a) - 2.204 \cdot 10^{-8} \cdot (T_s + T_a)^2 \tag{3.12}$$

$$K_{angle} = 1.194 - sin(\beta) - 0.194 \cdot cos(2\beta) + 0.368 \cdot sin(2\beta) \tag{3.13}$$

3.1.5. RADIATION HEAT LOSS

The last heat loss mechanism for the conductor is by radiation. The heat can radiate away when the surrounding temperature is lower than the temperate of the conductor. Therefore the temperature difference determines the heat of heat loss in equation equation 3.14.

$$P_r = \pi \cdot D \cdot \sigma_B \cdot \epsilon_s \cdot [(T_s + 273,15)^4 - (T_a + 273,15)^4] \tag{3.14}$$

Where σ_B is the Stefan-Boltzmann constant and ϵ_s the emissivity of the conductor surface. The Stefan-Boltzmann constant is expressed in Kelvin for which a constant as to be added to calculate the radiation cooling in degrees. The emissivity of a material surface is a factor which explain how much thermal radiation is emitted. Like absorptivity emissivity has a low initial value but increases when used in operation. However this increase in emissivity improves the rate of radiation to loss the heat from the conductor and has a value of 0.7 [12].
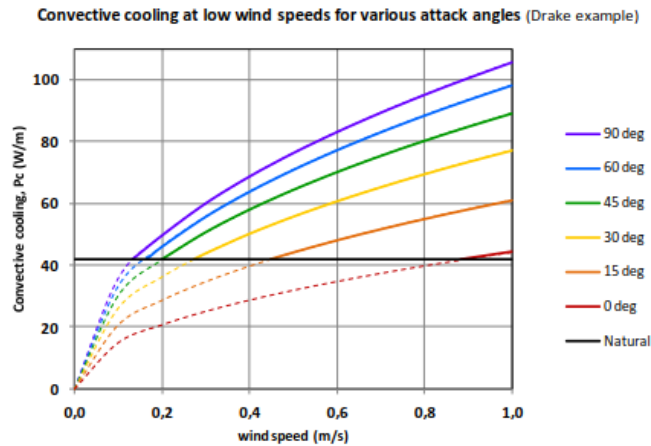
Figure 3.3: Forced convection heat loss by low wind speed and different angles [12]

3.2. HEAT EVALUATION

Depending on the rate of heat gains and losses the conductor will reach a stable temperature in case the weather conditions and electrical load are assumed constant. For the static line rating the steady state heat balance of equation 3.1 can be used to calculate the thermal current in equation 3.15.

$$I = \sqrt{\frac{P_c + P_r - P_M - P_s}{R_{dc} \cdot k_\lambda}} \qquad (3.15)$$

For dynamic line rating the non-steady state heat balance of equation 3.2 can be used when sufficient small steps in time are taken [13]. These steps should be smaller than the thermal time constants and allows to calculate the final conductor temperature after a certain time interval. Exact calculations of the of the final temperature can be evaluated in with Cigre paper [12].

3.3. THERMAL CONCEPTS CONCLUSION

The goal of this chapter to understand how the thermal current can be determined from the heat balance equations.

The different heat gains and losses were evaluated. By applying dynamic line rating the thermal current is safely increased. Joule heating increases by a higher thermal current due to the current with the power of two. Furthermore the resistivity also increases at a higher conductor temperature. Magnetic heating increases indirectly by a higher magnetic flux density. Solar heating does not change in case of an increased thermal current. However an increase of conductor temperature increases the radiation and convective heat losses. This follows from the temperature difference between the conductor and surrounding. In the next chapter the consequence of a higher conductor temperature is considered. The line will hang closer to the ground.

4

OVERHEAD LINE SAG EVALUATION

Contents

In chapter 2 several direct monitoring systems were evaluated. Furthermore in the previous chapter the heating gains and losses of the conductor were examined.

The goal of this chapter is to determine the sag of a conductor in case the conductor temperature is increased and concentrated weight is added. This ensures dynamic line rating to be applied safety.

First the sagging curve and the conductor length will be derived in sections 4.1 and 4.2 respectively. Second the influence of an increased temperature will be examine in section 4.4 and last the added weight of the real time monitoring system is determined in section 4.3.

4.1. SAGGING CURVE

A conductor which hang between two supporters will form a sagging curve as was seen in figure 2.1. To determine the change in the sagging curve the equilibrium of tensile forces is assumed. In figure 4.1 the vertical and horizontal components are derived for a small conductor element. The balance of the vertical tensile force V is stated in equation 4.1 while for the horizontal force H in equation 4.2. The infinitesimal length of the conductor can be divided as equation 4.3.
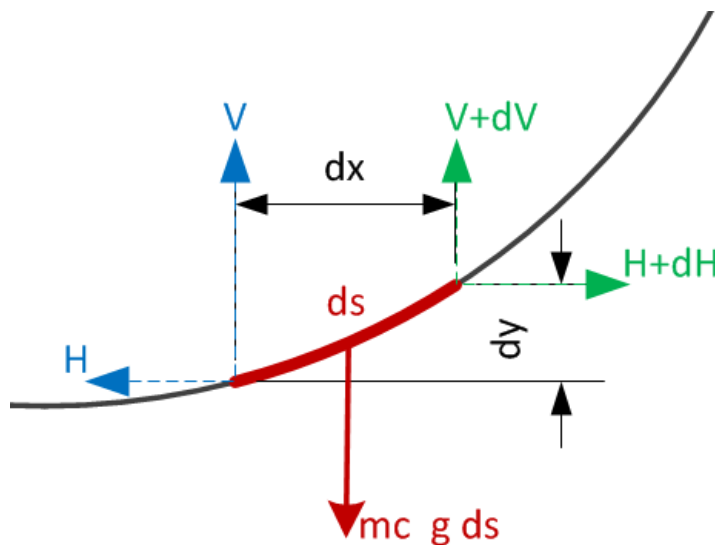
Figure 4.1: Tensile forces are in equilibrium at a small element on the conductor

$$V + dV - V = m_c \cdot g \cdot ds \tag{4.1}$$

$$H + dH - H = 0 \tag{4.2}$$

$$ds = \sqrt{dx^2 + dy^2} = dx\sqrt{1 + \left(\frac{dy}{dx}\right)^2} \tag{4.3}$$

Where m_c is the conductor mass per unit length, g the gravitational acceleration and ds the infinitesimal length of the conductor. The horizontal component of the tensile force does not change along the curve [14]. Furthermore the balance of moments at the the center of a conductor element can be written as equation 4.4

$$H \cdot dy = dV \cdot dx \tag{4.4}$$

$$\frac{dy}{dx} = \frac{V}{H} \tag{4.5}$$

By taking the derivative to x in equation 4.5 to x and inserting equations 4.1 and 4.3 a second order differential equation of the sagging curve is obtained in equation 4.6

$$\frac{d^2 y}{dx^2} = \frac{m_c \cdot g}{H}\sqrt{1 + \left(\frac{dy}{dx}\right)^2} \tag{4.6}$$

The solution of the sagging curve can be found in Appendix B.1 but result in equation 4.7.

$$y = \frac{H}{m_c \cdot g} \cdot cosh\left(\frac{m_c \cdot g}{H} \cdot x\right) \tag{4.7}$$

4.1.1. PARABOLA

With the sagging curve the distance from ground to conductor can be determined at any point in the line. However for practical applications the sagging curve of equation B.8 is replaced by a parabola in equation 4.8 [6].

$$y = \frac{m_c \cdot g \cdot x^2}{2H} \tag{4.8}$$

The approximation is valid as long as $(m_c \cdot g \cdot x)^2 / 12H^2 <<< 1$ [6]. The parabola simplifies the calculations of the sag in case of increased heat and weight and for calculators which do not have the hyperbolic functions. Now with a span of length S the maximum sag f_s can be calculated. For both the sagging curve and parabola in the equations 4.9 and 4.10 the lowest point of the line is the middle.

$$f_s = \frac{H}{m_c \cdot g}\left[\cosh\frac{m_c \cdot g \cdot S}{2H} - 1\right] \tag{4.9}$$

$$f_s = \frac{m_c \cdot g \cdot S^2}{8H} \tag{4.10}$$

4.2. CONDUCTOR LENGTH

The conductor length between the supporters will expand or contract by a change in temperature or tension of the conductor. Assuming the the span has a length the integral to dx of the sagging curve and parabola is found in equations 4.11 and 4.12 respectively.

$$L = \frac{2H}{m_c \cdot g} \sinh\left(\frac{m_c \cdot g \cdot S}{H}\right) \tag{4.11}$$

$$L = S\left[1 + \frac{(m_c \cdot g \cdot S)^2}{24H^2}\right] \tag{4.12}$$

With the definition of the conductor length the initial condition L_1 is found. With the effect of an increased temperature and weight the thermal and elastic expansions are used for the final conductor length L_2 in equation 4.13.

$$L_2 = L_1 \cdot [1 + \epsilon_t \cdot (T_2 - T_1)] \cdot \left[1 + \frac{H_2 - H_1}{E \cdot A}\right] \tag{4.13}$$

Where ϵ_t is the thermal expansion coefficient, $T_{1,2}$ the conductor temperature, $H_{1,2}$ the horizontal conductor tensile forces, E the elasticity modulus and A the cross section of the conductor. From equation 4.13 the conductor state of change can be found in equation 4.14 to determine the final horizontal tension force. The conductor mass per unit length m_{c2} does not change with an increased temperature.

$$H_2^2\left[H_2 - H_1 + \frac{E \cdot A \cdot (S \cdot m_{c1} \cdot g)^2}{24H_1^2} + E \cdot A \cdot \epsilon_t(T_2 - T_1)\right] = \frac{E \cdot A \cdot (S \cdot m_{c2} \cdot g)^2}{24} \tag{4.14}$$

4.3. WEIGHT INCREASE

Installing the real time monitoring system adds weight to the overhead line at a single point. This can be treated as a concentrated load G. The sag with a concentrated load can be determined by the equivalence between the sag and the bending moments of an equivalent beam with equivalent loads [14]. Therefore the conductor length is now determined by equation 4.15

$$L = S + \frac{1}{2H^2} \int_0^S Q^2 dx \tag{4.15}$$

Where Q is the transverse force. The conductor state of change can be determined with equation 4.13. Next the horizontal tensile force can be determined for the conductor with concentrated load in equation 4.16.

$$H_2^2 \left[H_2 - H_1 + \frac{E \cdot A}{2S \cdot H_1^2} \int_0^S Q_1^2 dx + E \cdot A \cdot \epsilon_t (T_2 - T_1) \right] = \frac{EA}{2S} \int_0^S Q_2^2 dx \tag{4.16}$$

Where Q_1 is the transverse force in case no concentrated load is installed, while Q_2 has. The integral can be solved with Simpson rule analytically. For a single concentrated load in the middle of the span the transverse force can calculated by equation 4.17 [14]. The sag can be calculated by equation 4.18.

$$\int_0^a Q(x)^2 dx = \sum_{i=1}^n \frac{d_i}{3} (Q_{i-1}^2 + Q_i^2 + Q_{i-1}^2 \cdot Q_i) = \frac{G^2 \cdot S}{4} + \frac{G \cdot m_c \cdot g \cdot S^2}{4} + \frac{(S \cdot m_c \cdot g)^2 \cdot S}{12} \tag{4.17}$$

$$f = \frac{1}{H} \left[\frac{m_c \cdot g \cdot S^2}{8} + \frac{G \cdot S}{4} \right] \tag{4.18}$$

Assuming an overhead line with a single span of 500 m at a height of 32.5 m. In table 4.1 the sag is calculated when the real time monitoring weight is 5 kg, 10 kg or 15 kg. In figure 4.2 the effect of and added 15 kg is shown.

Span	Original	+5 kg	+10 kg	+15 kg
500 m	18.84 m	19.08 m	19.33 m	19.58 m

Table 4.1: The maximum sag for different weights of installed monitoring devices.
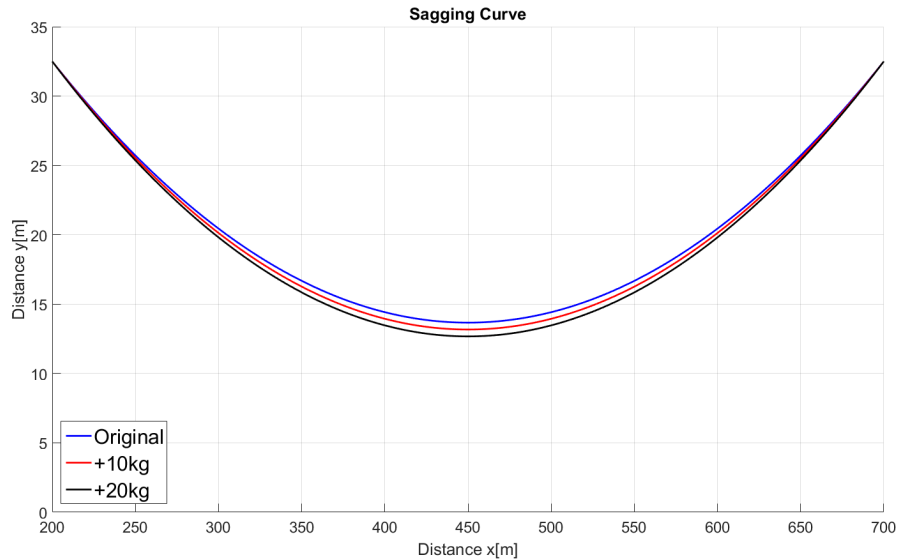
Figure 4.2: Sagging curve increased by an installed monitoring device

4.4. TEMPERATURE INCREASE

To determine the change in sag with an increased temperature the other spans of an overhead has to be taken into account. Because an overhead line can consists of one or more spans each consist of a different length and temperature variation due to cooling [6]. It is possible to calculate the increased sag individually but this is inefficient. An alternative is to apply the calculations of the conductor state on the equivalent span once and determine the sag for each span from there. The equivalent span can be used due to the natural equalization of the tension. Thereby is assumed the variation of conductor temperature is the same as the variation in tension for any span of the line [6].

The equivalent span can be determined with equation 4.19 where $S_{1,2,...n}$ is the first, second... nth span of the overhead line.

$$S_{eq} = \sqrt{\frac{S_1^3 + S_2^3 + ... + S_n^3}{S_1 + S_2 + ... + S_n}} \tag{4.19}$$

From here the equivalent sag can be determined with the equations 4.9 and 4.10 for the maximum sag. The maximum sag from any span can easily found with equation 4.20.

$$f_i = f_{eq} \cdot \left(\frac{S_i}{S_{eq}}\right)^2 \tag{4.20}$$

Assuming an overhead line with a three supporters at a height of 32.5 m with three spans of 300 m, 500 m and 200 m. In figure 4.3 the sag is drawn when the temperature of the conductor is increased by 50 °C. Furthermore the maximum sag is calculated for a increased temperature of 5 °C, 10 °C, 25 °C and 50 °C in table 4.2.
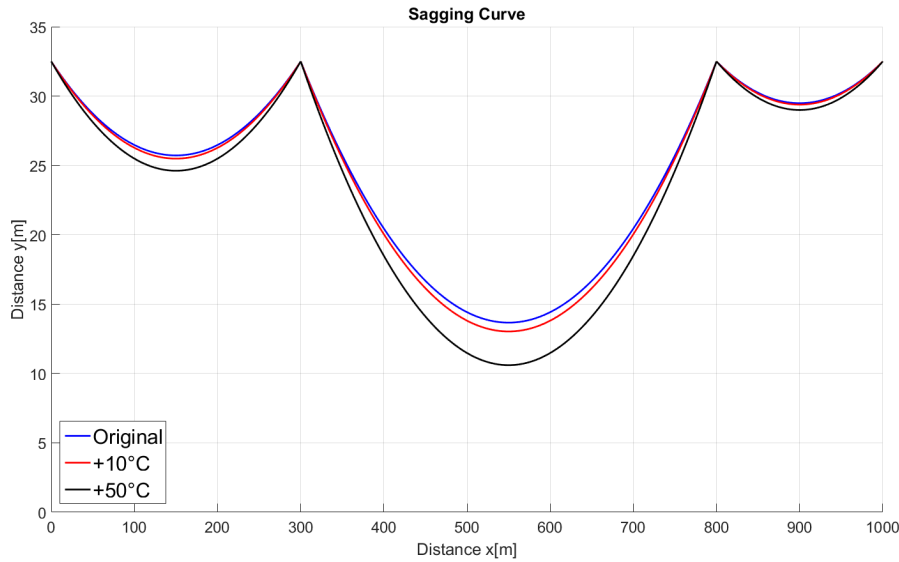
Figure 4.3: The sagging curve for a 300 m, 500 m and 200 m span when the conductor temperature is increased with 10 °C and 50 °C

Span	Original	+5 °C	+10 °C	+25 °C	+50 °C
300 m	6.78 m	6.90 m	7.01 m	7.35 m	7.88 m
500 m	18.84 m	19.15 m	19.47 m	20.40 m	21.90 m
200 m	3.01 m	3.06 m	3.12 m	3.26 m	3.50 m

Table 4.2: The maximum sag for different temperature increases

4.5. OVERHEAD LINE SAG EVALUATION CONCLUSIONS

The goal of this chapter was to determine the sag in case the conductor temperature increases and concentrated weight is added from the real-time monitoring system.

The curve of the conductor between two supporters was derived and applied on different spans. The sag of longer spans are most affected by an increase of conductor temperature: a temperature increase of 5 °C result in a increased sag of 31 cm for a 500 m span, while only 12 cm for a 300 m span. Adding a concentrated weight of 5 kg increases the sag by 24 cm. Increasing the temperature of the conductor increases the maximum sag more in respect to adding concentrated weight. It was found in [6] that an increase of sag of more than 2 m exceed the safety limits. However increasing the conductor temperature by 25 °C or more exceed the limit.

5

ELECTRICAL CONCEPTS

Contents

    In chapter 4 the consequence of a higher conductor temperature was examine. Another consequence will be a higher magnetic field around a conductor.

The goal of this chapter is to determine the magnetic field strength at 5 cm below the conductor and the required shielding. Inside the real-time monitoring the maximum magnetic field is 10 μT to reduce the risk of damaging or destroying the electronics.

First the magnetic field components are derived in section 5.1. Second the reason behind the limitation of the external magnetic field is discussed in section sec:induction. Last in section 5.3 the required shielding effectiveness is determined.

5.1. OVERHEAD LINE MAGNETIC FLUX DENSITY

The magnetic field for a three phase (3ϕ) double circuit of an overhead line will be determined. First the magnetic field components derived. First a single phase conductor is assumed in Ampere's law of equation 5.1. Here it is stated that any line integral of the magnetic field, along a closed path L, is equal to a **continuous current** enclosed by that the surface. At a distance r the magnitude of the magnetic field is equal and forms a circle around the conductor. The magnitude of the magnetic field can be determined by equation 5.3.
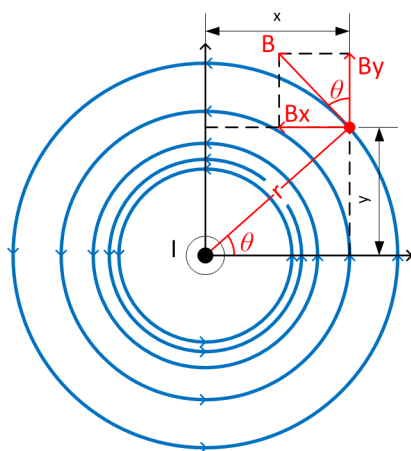
Figure 5.1: Magnetic field in Cartesian coordinate system.

$$\oint_L H \cdot dL = I \tag{5.1}$$

$$H \cdot \oint_L dL = I \tag{5.2}$$

$$B = \frac{\mu_0 \cdot I}{2\pi R} \tag{5.3}$$

Here H is the magnetic field, μ_0 the permeability of vacuum and B is the magnetic flux density which decreases inversely proportional to the distance. Furthermore the direction of the magnetic field is determined by Biot-Savart right-hand rule [15]. In case the current is in direction out of the paper the magnetic field lines are in counter clockwise. In figure 5.1 several circles are shown.

To determine the magnitude of magnetic field for a three phase double circuit the Cartesian coordinate (x, y, z) is used. The distance (x, y) and the radius of the circles can be transformed by Pythagoras as $r = \sqrt{x^2 + y^2}$. The x and y components of the magnetic field is derived in equations 5.5 and 5.6 respectively. The minus sign in equation 5.5 follows from the chosen Cartesian coordinate system in figure 5.1.

$$B = \sqrt{B_x^2 + B_y^2} \tag{5.4}$$

$$B_x = -B \cdot sin(\theta) = -\frac{\mu_0 \cdot I}{2\pi \cdot \sqrt{x^2 + y^2}} \cdot \frac{y}{r} = -\frac{\mu_0 \cdot I \cdot y}{2\pi(x^2 + y^2)} \tag{5.5}$$

$$B_y = B \cdot cos(\theta) = \frac{\mu_0 \cdot I}{2\pi \cdot \sqrt{x^2 + y^2}} \cdot \frac{x}{r} = \frac{\mu_0 \cdot I \cdot x}{2\pi(x^2 + y^2)} \tag{5.6}$$

5.1.1. 3ϕ CURRENT

In figure 5.1 it is assumed that the direction of the current is out of the paper. However an overhead line carries alternating current with a frequency f of 50 Hz. Therefore each half of the time period the current varies direction from outside and inside the paper. Furthermore the electric grid use 3ϕ alternating currents for the transmission and distribution grid. The advantage of a 3ϕ system is that the same amount of power can be transported with only three conductors instead of three single phase systems which would requires six conductors [16]. Assuming a balanced 3ϕ system in which currents are equal in magnitude and only shifted by 120 degree from each other. This result in equation 5.7 .

$$
\begin{aligned}
I_a &= \sqrt{2} \cdot |I| \cdot cos(2\pi \cdot f \cdot t) & &= \sqrt{2} \cdot |I| \\
I_b &= \sqrt{2} \cdot |I| \cdot cos(2\pi \cdot f \cdot t - \frac{2\pi}{3}) & &= \frac{-\sqrt{2}}{2} \cdot |I| \\
I_c &= \sqrt{2} \cdot |I| \cdot cos(2\pi \cdot f \cdot t - \frac{4\pi}{3}) & &= \frac{-\sqrt{2}}{2} \cdot |I|
\end{aligned}
\tag{5.7}
$$

Here $|I|$ is the root-mean-square current(RMS) and $\sqrt{2} \cdot |I|$ the peak value of the alternating current. With a conductor peak current of 800 A the magnetic field components 1 m above ground result in figure 5.3. This result in a magnetic field is 7.1 μT. Furthermore the magnetic field 5 cm below the conductor result in figure 5.4. Here the maximum magnetic field is 3.2 mT and consist of the x-component only.
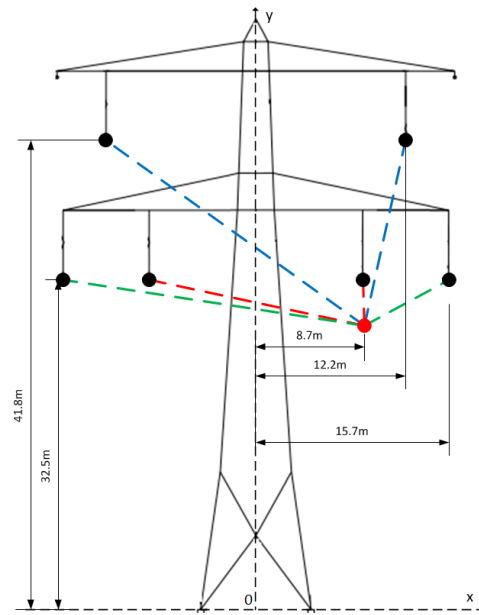
Figure 5.2: A 3 phase double circuit overhead line. The conductors are in phase when the color of the dotted line to the red point is the same.
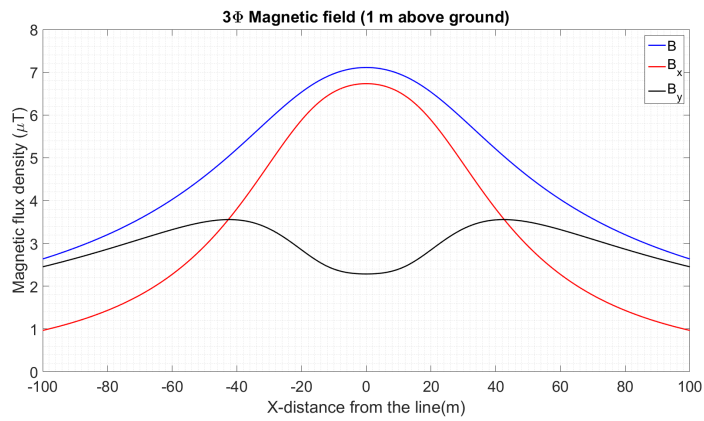
Figure 5.3: Magnetic field components very close to the ground.
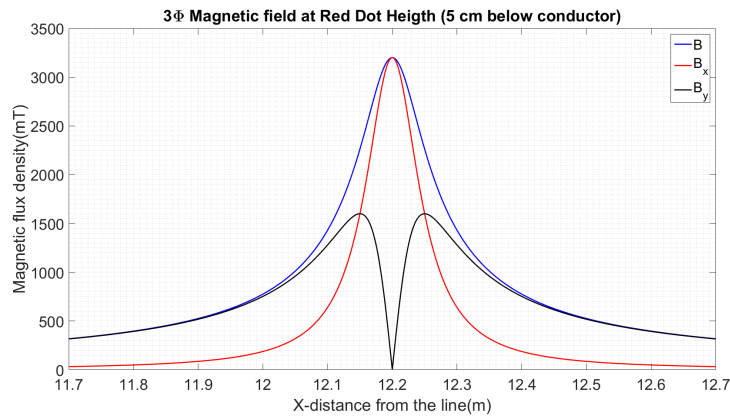
Figure 5.4: Magnetic field components very close to the conductor.

5.2. INDUCTION

In the scope of the thesis it was set that the magnetic field inside the real-time monitoring device has to be reduced to 10 μT. This reduction is required to reduce the possible induced voltage on the electronics. To understand this voltage Faraday's law of induction is used in equation 5.8. In this equation it is stated that a line integral of an electric field along a closed path L is equal to the rate magnetic flux ϕ change through the surface which is the enclosed by the line. This generates and electromotive force (emf) around the closed contour.

$$\oint_L E \cdot dL = -\frac{d\phi}{dt} \tag{5.8}$$

$$emf = -\frac{d}{dt}\int_s B \cdot dS \tag{5.9}$$

Here the minus sign follows from Lenz's law and symbolize the direction of induced current along its path. These currents create a magnetic field on its own and tends to oppose the original magnetic field. The emf is a distributed quantity and cannot be measured, but can be represented by a lumped voltage source as can be seen in figure 5.5 [17]. Furthermore an emf can also be induced by an alternating magnetic field in case the surface is open. A voltage will appear at the terminals as can be seen in figure 5.6.
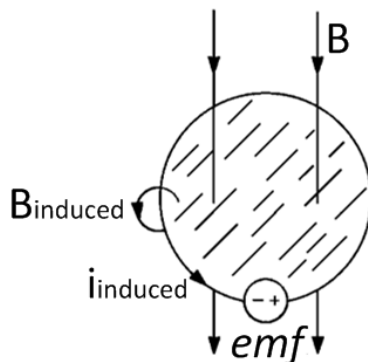
Figure 5.5: A time varying magnetic field induced voltage and a current which oppose the original magnetic field B [17]
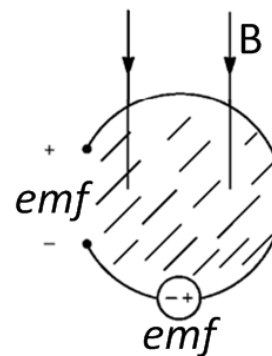
Figure 5.6: A time varying magnetic field induced voltage on the terminals but no current will flow[17]

5.3. Prototype emf

The electronics of the real-time monitoring system consist of a printed circuit board (PCB) with a micro controller, power supply, loads etc. The PCB has several input/output pins to which a battery, an external antenna or other loads can be connected by traces. However the traces forms an enclosed area in which a emf can be induced as can be seen in figure 5.7 .

   In normal conditions a 50 Hz current flow through the conductors of an overhead line. The current has a time period of 20 ms and result in a low emf. However phenomenas like short-circuits, lightning and switching impulse are faults on the overhead line with times period of only several micro seconds. Furthermore the current are much higher than what the conductor normally transport. As discussed in section 5.1 the magnetic field is proportional to the current. The combination of high magnetic field and fast change in time result in an high emf in the electronics. By limiting the maximum magnetic field inside the real-time monitoring system the emf can reduced. Another method is by reducing the possible enclosed area. This can be done by routing the traces of the signals which goes inward and outwards closer together like in figure 5.7 [18].
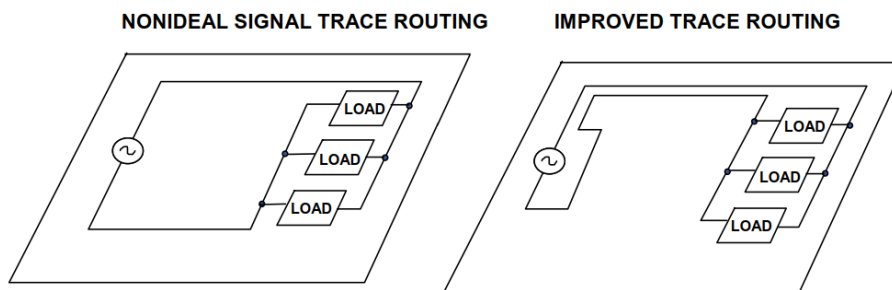
Figure 5.7: Rerouting the traces to reduce the area [18]

   With the target of 10 μT inside the real-time monitoring system and an external field of 3.2 mT the amount of reduction can be determined. The reduction of magnetic field is called shielding effectiveness (SE) and is expressed in decibels in equation 5.10.

$$SE = 20 \cdot log \left[\frac{3.2\, mT}{10\, \mu T} \right] = 50.1 \text{ dB} \qquad (5.10)$$

5.4. Electrical concept conclusions

The goal of this chapter was to determine the magnetic field below a conductor and to determine the required shielding.
The magnetic field was derived in its components and simulated which resulted at 3.2 mT for a distance of 5 cm below the conductor. Furthermore the reason behind reducing the magnetic field to 10 μT was explained. Reducing the magnetic field reduces the possible emf but requires a shielding effectiveness of 50.1 dB. In the next chapter the theory for shielding will be explained.

PROTOTYPE SHIELD CONCEPT

Contents

In the previous chapter the required shielding effectiveness was determined.
The goal of this chapter is to evaluate two different shielding mechanisms to reduce the magnetic field and to determine which material and corresponding thicknesses is required. First shielding by the impedance method will be discussed. Second more insight is given at electric shielding in section 6.2. Third magnetic shielding with the method of separation of variable is examine in section 6.3. Last several materials are considered for the prototype and the effect of holes are examine in the sections 6.4 and 6.5 respectively.

6.1. ELECTROMAGNETIC SHIELDING

In this section shielding of an electromagnetic wave by the impedance method will be discussed. This method describes how much an incoming wave is reflected or transmitted through a medium. First the source is located at a far distance to assume an uniform plane wave. Second the source is located close to conductive barrier. For this the intrinsic impedance will be separated for a electric and magnetic source. In the last part the used method will be discussed for low frequency magnetic shielding.

6.1.1. SHIELDING EFFECTIVENESS FAR FIELD

To determine the shielding effectiveness an uniform plane wave incident on a conductive conductive barrier with thickness t in figure 6.1. This is the impedance method. However an uniform plane does not physically exist. Uniform plane wave will propagate to infinity with an infinite amount of energy [19]. Fortunately for the propagation of waveguides the uniform plane wave provide acceptable approximation. Furthermore these assumptions allows to treat the electric and magnetic field independently of their position in each plane[17].

In figure 6.1 the uniform plane wave propagate in medium 1 along the $+y$ direction and incident on medium 2 the conductive barrier at $y = 0$ and medium 3 at $y = t$. Medium 1 & 3 are assumed to be free space. At these boundaries the incident wave will be reflected back or transmitted through the medium. The wave equations are showed in 6.1.

$$\mathbf{E}_i(y) = E_i \cdot e^{-\gamma_1 y}\hat{\mathbf{z}} \quad \text{then} \quad \mathbf{H}_i(y) = \frac{E_i}{\eta_1} \cdot e^{-\gamma_1 y}\hat{\mathbf{x}} \tag{6.1a}$$

$$\mathbf{E}_r(y) = E_r \cdot e^{\gamma_1 y}\hat{\mathbf{z}} \quad \text{then} \quad \mathbf{H}_r(y) = \frac{E_r}{\eta_1} \cdot e^{\gamma_1 y}(-\hat{\mathbf{x}}) \tag{6.1b}$$

$$\mathbf{E}_1(y) = E_1 \cdot e^{-\gamma_2 y}\hat{\mathbf{z}} \quad \text{then} \quad \mathbf{H}_1(y) = \frac{E_1}{\eta_2} \cdot e^{-\gamma_2 y}\hat{\mathbf{x}} \tag{6.1c}$$

$$\mathbf{E}_2(y) = E_2 \cdot e^{\gamma_2 y}\hat{\mathbf{z}} \quad \text{then} \quad \mathbf{H}_2(y) = \frac{E_2}{\eta_2} \cdot e^{\gamma_2 y}(-\hat{\mathbf{x}}) \tag{6.1d}$$

$$\mathbf{E}_t(y) = E_t \cdot e^{-\gamma_3 y}\hat{\mathbf{z}} \quad \text{then} \quad \mathbf{H}_t(y) = \frac{E_t}{\eta_3} \cdot e^{-\gamma_3 y}\hat{\mathbf{x}} \tag{6.1e}$$

Here γ is the propagation constant and η the intrinsic impedance of the medium. For the free space the conductivity is zero and therefore the attenuation constant also in equation 6.2 [19]. The conductive barrier is assumed a good conductor for which the properties are summarized in 6.3.

$$\text{Medium 1 \& 3:} \quad \gamma_{1,3} = \beta_0 = \omega\sqrt{\mu_0\epsilon_0} \qquad \text{and} \quad \eta_{1,3} = \sqrt{\frac{\mu_0}{\epsilon_0}} = \eta_0 \tag{6.2}$$

$$\text{Medium 2:} \quad \gamma_2 = \sqrt{j\omega\mu(\sigma + j\omega\epsilon)} = \frac{1}{\delta} + j\beta \quad \text{and} \quad \eta_2 = \sqrt{\frac{j\omega\mu}{\sigma + j\omega\epsilon}} \tag{6.3}$$

The exact solution follows from the continuity equation (which will described in more detail in equation 6.12) of the electric and magnetic field at the boundaries $y = 0$ and $y = t$. In short the continuity equation describes how the tangential components between two different medium are equal. From this the following four equation are found in 6.4.
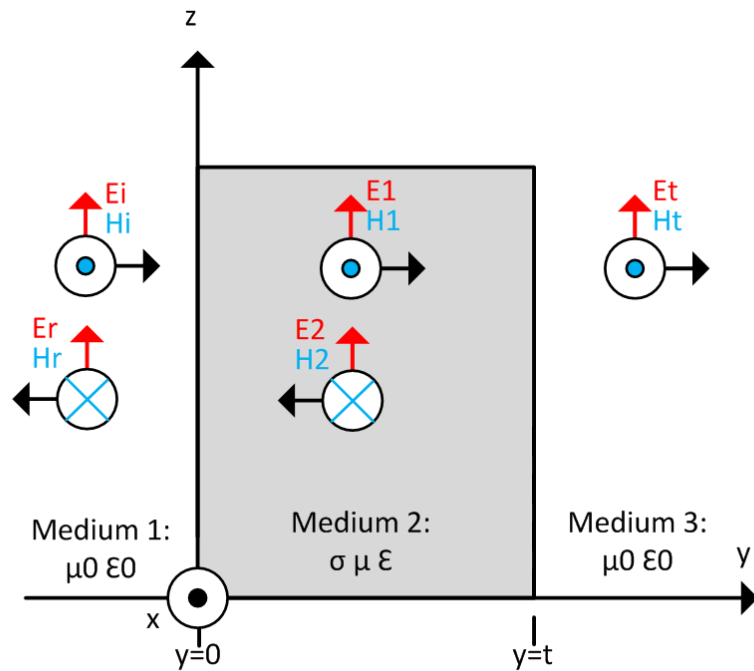
Figure 6.1: An incident plane wave interaction between free spaces and a conductor

$$E_i + E_r = E_1 + E_2 \tag{6.4a}$$

$$\frac{E_i}{\eta_0} - \frac{E_r}{\eta_0} = \frac{E_1}{\eta_2} - \frac{E_2}{\eta_2} \tag{6.4b}$$

$$E_1 \cdot e^{-\gamma_2 t} + E_2 \cdot e^{\gamma_2 t} = E_t \cdot e^{-\gamma_3 t} \tag{6.4c}$$

$$\frac{E_1}{\eta_2} \cdot e^{-\gamma_2 t} - \frac{E_2}{\eta_2} \cdot e^{\gamma_2 t} = \frac{E_t}{\eta_0} \cdot e^{-\gamma_3 t} \tag{6.4d}$$

From the four equations an expression of the ratio between the incident and transmitted wave can found in equation 6.5. The required steps to derive this solution can be found in Appendix B.2.

$$\frac{\mathbf{E}_i}{\mathbf{E}_t} = \frac{(\eta_0 + \eta_2)^2}{4\eta_0\eta_2} \cdot e^{\frac{t}{\delta}} e^{j\beta t} e^{-j\beta_0 t} \cdot \left[1 - \left(\frac{\eta_0 - \eta_2}{\eta_0 + \eta_2} \right)^2 e^{\frac{-2t}{\delta}} e^{\frac{-j2t}{\delta}} \right] \tag{6.5}$$

Equation 6.5 is the exact solution of the electric field which incident on the conductive barrier and remain to propagate in $+y$ direction. From the exact solution the shielding effectiveness can be determined by taking the logarithm. The absolute value of a complex exponential function can be solved by equation B.20 of the Appendix. Furthermore the impedance of any conductor is much less than the intrinsic impedance($\eta_2 \ll \eta_0$), which simplifies equation 6.1. The result is shown in equation 6.6. Where R is the reflection losses at both side of the surfaces, A is the absorption loss through the material and M the losses from multiple reflections and transmission within the shield.

$$SE = \underbrace{20 \cdot log_{10} \left| \frac{\eta_0}{4\eta_2} \right|}_{R} + \underbrace{20 \cdot log_{10}(e^{\frac{t}{\delta}})}_{A} + \underbrace{20 \cdot log_{10} \left| 1 - e^{\frac{-2t}{\delta}} \right|}_{M} \tag{6.6}$$

6.1.2. SHIELDING EFFECTIVENESS NEAR FIELD

The shielding effectiveness was determined for a source which was located in the far field. In the far field a plane wave has an electric and magnetic field component which are orthogonal and can be characterized as the intrinsic impedance ($\mathbf{E_z}/\mathbf{H_x} = \eta_0$). However the far field region starts for distances from the source when further than approximately $3\lambda_0$ [17]. This means for an electromagnetic wave with a frequency of 50 Hz the far field starts after several kilometers. Therefore the intrinsic impedance cannot be used to characterize the wave impedance. For the near field the source is separated as an electric dipole and small magnetic loop. The wave impedance of these sources are stated in equation 6.7.

$$Z_{WE} = \frac{1}{2\pi f \epsilon_0 r} \qquad \text{Near field electric source} \tag{6.7a}$$

$$Z_{WH} = 2\pi f \mu_0 r \qquad \text{Near field magnetic source} \tag{6.7b}$$

Here r is the distant from the source. The real time monitoring system will be installed on the overhead line. Assuming the electronics will be installed at approximately 5 cm away and in a copper(Cu) barrier with thickness $t = 1$ mm. The shielding effectiveness from equation 6.6 is applied with the replacement of the intrinsic impedance over several frequencies.

ELECTRIC FIELD

The shielding effectiveness in the near field of electric sources is shown in figure 6.2. As can be seen the reflection is dominant in the lower frequencies, while absorption is for the high frequencies the dominant mechanism which determine the shield effectiveness. The reason for the high shielding effectiveness for all frequencies will be discussed in more detail in section 6.2.

MAGNETIC FIELD

For the magnetic sources in the near field the shield effectiveness result in figure 6.3. For high frequencies absorption is dominant factor for the shielding effectiveness. However for the low frequencies both reflection and absorption is small to zero. Shielding from a low frequency magnetic source can be performed by using the following two methods:

- Generate a opposing magnetic flux to oppose the magnetic field

- Redirect the magnetic flux with high permeability material

An opposing magnetic flux will be generated by a conductor loop which was already discussed in 5.2. Redirecting the flux can be done by providing a reluctance path materials high permeability . However using such material does not solve low frequency magnetic shielding if applied by the method of this section.

6.1.3. LIMITATION TRAVELING METHOD

To determine the required shielding thickness the impedance method does not provide a solution in the case of practical applications. There are several reasons for this.

First the shield is assumed to be an single infinite sheet of metal[20]. To shield a finite sized region from an electromagnetic wave it will enclosure the region by several walls. Every wall will absorb or reflect the electromagnetic wave. This complicate the calculations and is not taken into account in the impedance method. Second shielding by reflection follows from the currents in the metal [21]. A current can only flow in the metal when a return path is available.
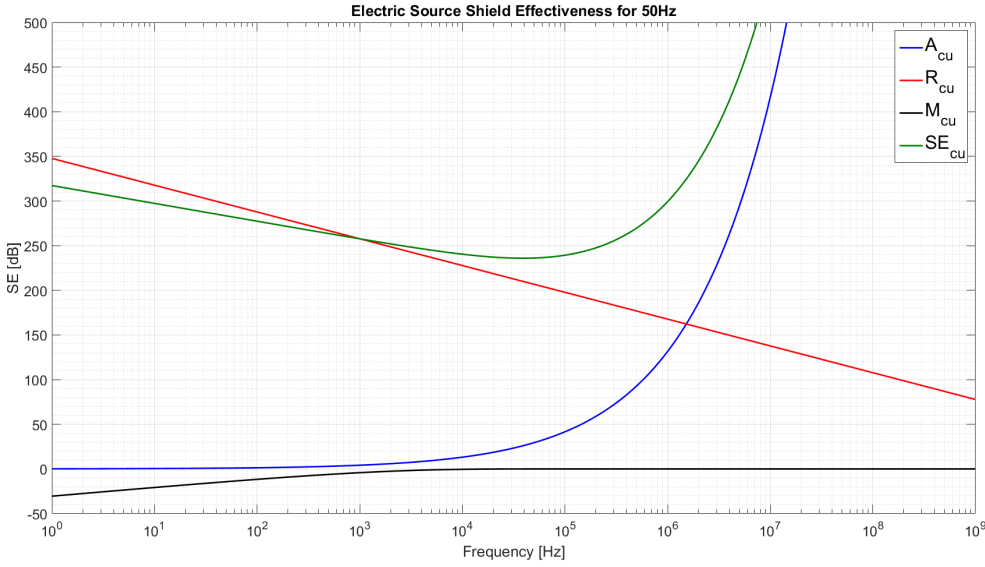
Figure 6.2: Shielding effectiveness for an electric source in the near field. For the low frequency reflection is the dominant factor while for high frequency absorption determines.
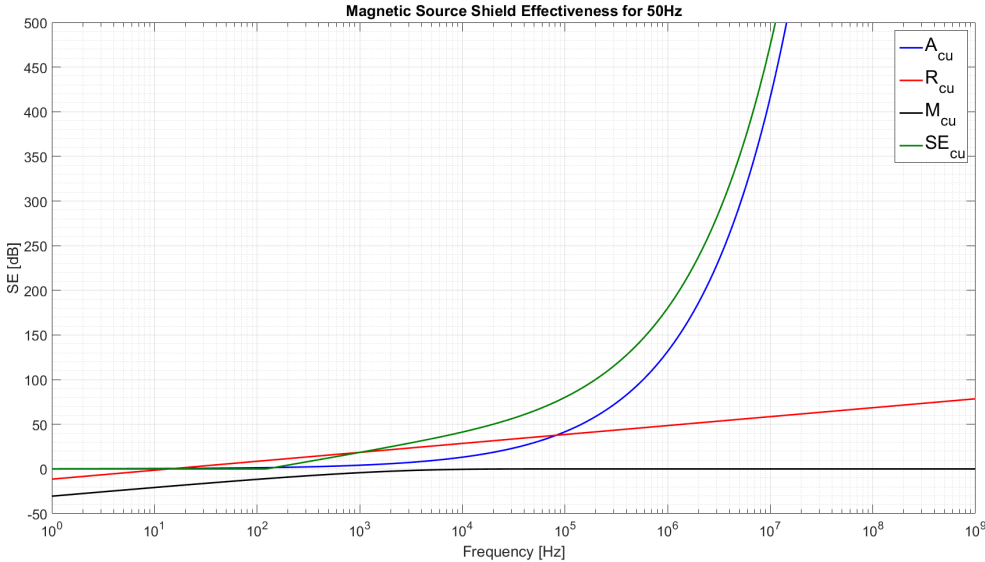
Figure 6.3: Shielding Effectiveness for a magnetic source in the near field. For the low frequency no shielding is possible while for high frequency absorption determines

6.2. ELECTRIC SHIELDING

In the previous section electric shielding with the impedance method provided a high shielding effectiveness for all frequencies. Regardless of the limitations of this method electric shielding can easily performed. Starting with a positive charge close to a conductor. In the presence of a external charge the free charges inside the conductor are moving to oppose the external charge. In case of a positive point charge the negative charges of the conductor move to the surface as can be seen in figure 6.4. The movement of charges result in a electric current in the conductor. This is proportional to the electric field and the conductivity of the material in equation 6.8.

$$J = \sigma E \tag{6.8}$$

The current density J and the charges inside a conductor are related by the continuity equation. The derivation of this equation starts with the divergence of the curl of the magnetic field in equation 6.10. For any vector field this is equal to zero. Second by applying the divergence both side and substituting the equation of Ampere's law of equation 6.9 in the time domain the continuity equation is obtained in equation 6.12.

$$\nabla \times H = \sigma E + j\omega\epsilon E \tag{6.9}$$

$$\nabla \cdot (\nabla \times H) = 0 \tag{6.10}$$

$$\nabla \cdot \left(\frac{\partial D}{\partial t} + J \right) = 0 \tag{6.11}$$

$$\nabla \cdot J = -\frac{\partial \rho}{\partial t} \tag{6.12}$$

The continuity equation describes the case when a current enters a region the amount of charges inside that region are increasing. With the continuity equation, equation 6.8 and Gauss's law of equation 6.13 an expression for the charge density can be obtained in equation 6.14. This differential equation can be solved analytically. The result is obtained in equation 6.16.

Here $\tau = \epsilon/\sigma$ is the relaxation time in which the charges move and redistributed themselves to oppose the external electric field. After the relaxation time the conductor is in electrostatic equilibrium [15]. The relaxation time depends on the conductivity and permittivity of the conductor's material. For copper this takes $\approx 1.5 \cdot 10^{-19}$ s and for aluminum $\approx 2.5 \cdot 10^{-19}$ s. The relaxation time of these materials are so short that the electric field inside a conductor can be assumed zero for any time varying electric field [22].
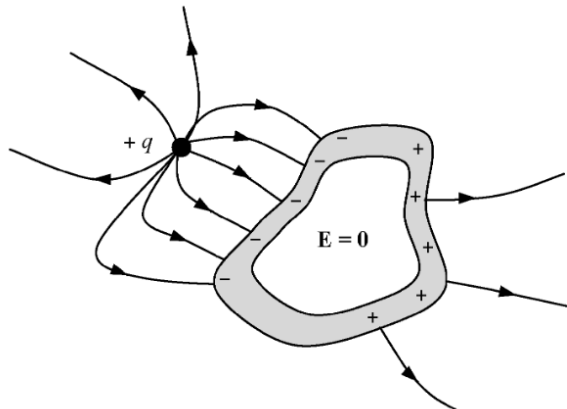
$$\nabla \cdot E = \frac{\rho}{\epsilon} \tag{6.13}$$

$$\nabla \cdot J = \sigma (\nabla \cdot E) \tag{6.14}$$

$$-\frac{\partial \rho}{\partial t} = \frac{\sigma}{\epsilon} \rho \tag{6.15}$$

$$\rho(t) = \rho(0) \cdot e^{-\frac{t}{\tau}} \tag{6.16}$$

Figure 6.4: The free charges in the conductor move to oppose the positive point charge
[23]

6.3. MAGNETIC SHIELDING

In section 6.1 magnetic shielding with the impedance method resulted in no shielding at all. However this method did not considered a finite size region and was therefore not useable for practical use. In this section the method of variable separation will be determined.

First several assumptions and boundary conditions are considered. Then the geometry to be shielded will be described. Last for each region a second order differential equation has to be solved to determine the shielding effectiveness.

First Ampere's law of equation 5.1 was valid for continuous currents. However for the seperation of variables method non-continuous current have to be considered as well. Therefore Ampere's law is defined as equation 6.17.

$$\oint_L H \cdot dL = I + I_d = I + \epsilon \frac{d\phi_e}{dt} \tag{6.17}$$

Where ϵ is the permittivity of the material which consist of the relative permittivity ϵ_r and the permittivity of vacuum ϵ_0 and ϕ_e the flux of the electric field though the same surface the contour enclosed. Inclusing Stokes's theorem in the frequency domain in 6.18 and 6.19 and adding Gauss laws for electrical charges and magnetism makes the Maxwell equations are complete:

$$\nabla \times H = \sigma E + j\omega\epsilon E \tag{6.18}$$

$$\nabla \times E = -j\omega\mu H \tag{6.19}$$

$$\nabla \cdot E = \frac{\rho}{\epsilon} \tag{6.20}$$

$$\nabla \cdot H = 0 \tag{6.21}$$

Here σ the material conductivity, $\sigma E = J$ is the current density j and ρ the charge density. For shielding applications the induced currents in the metallic shield and surrounding magnetic field in the air are of interest. Therefore the assumption of **quasi-stationary** currents is used. There are two conditions before quasi-stationary currents can be applied.

First the currents are equal in magnitude at any position in the conductor and can be time varying [24]. Second the currents can be separated into variables in equation 6.22. Under these assumptions in quasi-stationary the displacement currents are disregard in equation 6.18.

- Geometrical dimensions are much smaller than the wavelength of the electromagnetic field

- Mutual coupling of the electric and magnetic field can be neglected.

$$j(r,t) = j(r) \cdot j(t) \tag{6.22}$$

6.3.1. SOLVING MAXWELL EQUATIONS

To determine the shielding effectiveness for magnetic shielding the Maxwell equations are solved in each region: the inner, outer and shielding region. Furthermore the boundary conditions between the regions have to be defined.

The inner and outer region are normally filled by air. The conductivity of air is normally zero. Therefore including the assumption of quasi-stationary in equation 6.9 it can be stated that the magnetic field has a potential field in air [25]. Instead of deriving the shield equations with three components of the magnetic field strength a scalar function can be defined as scalar potential X where $H = \nabla X$. The differential equation of the scalar potential is found by taking the divergence in equation 6.19 on both side. It is known the divergence of the curl is equal to zero (Gauss's law of magnetism in equation 6.21) the equation 6.23 is designed.

$$\nabla \cdot H = \nabla \cdot (\nabla X) = \Delta X = 0 \tag{6.23}$$

The region of the shield is mostly metallic which has a finite conductivity. Therefore the scalar potential can not be used. The differential equation which has to be solved in this region under the quasi-stationary condition follows from the equations 6.18 and 6.19. Here $k^2 = j\omega\mu\sigma$ is defined as the eddy current constant and is related to the skin depth by $k = \frac{1+j}{\delta}$ where $\delta = \sqrt{\frac{2}{\omega \cdot \mu \cdot \sigma}}$ [25].

$$\gamma^2 = j\omega\mu(\sigma + j\omega\epsilon) \qquad k^2 = j\omega\mu\sigma = \omega\mu\sigma e^{i\frac{\pi}{2}} \tag{6.24}$$

$$k = \sqrt{\omega\mu\sigma}\, e^{i\frac{\pi}{4}} = \sqrt{\omega\mu\sigma}\left(\frac{1+i}{\sqrt{2}}\right) \tag{6.25}$$

$$\nabla \times \nabla \times H = \sigma(\nabla \times E) \quad \text{or} \quad \nabla \times \nabla \times E = -j\omega\mu(\nabla \times H) \tag{6.26}$$

$$\nabla \times \nabla \times H = -k^2 H \qquad \text{or} \quad \nabla \times \nabla \times E = -k^2 E \tag{6.27}$$

$$\nabla^2 H - k^2 H = 0 \qquad\quad \text{or} \quad \nabla^2 E - k^2 E = 0 \tag{6.28}$$

$$\nabla^2 H - \gamma^2 H = 0 \qquad\quad \text{or} \quad \nabla \times \nabla \times E = -\gamma^2 E \tag{6.29}$$

6.3.2. Boundary Conditions

For each of the three regions a second order differential equation has to be solved to determine the required shielding. For the regions which consist of air this is equation 6.23 while for the shield equation 6.28. Each second order differential equation will have two constants to solve. The constants can be determined by continuity requirements of the transition regions in table 6.1 and by the excitation conditions. Here $\mu = \mu_0 \mu_r$ Assuming the tangential components of the electric and magnetic field passes through the transition regions without jumps [25].

The excitation conditions clarify two solutions. If a magnetic field is excited in the outer region the solution of the differential equation has a finite value in the inner region. Second if excitation is in the inner region the solution correspond overall finite in the outer region even in the infinity [25]. In practical applications shields are not perfect conductors and can have apertures through which the outer magnetic field can reach the inner region [26].

Magnetic field transition	Tangential	Normal
Inner to shield region	$H_{t1} = H_{t2}$	$\mu_0 H_{n1} = \mu H_{n2}$
Shield to outer region	$H_{t2} = H_{t3}$	$\mu H_{n2} = \mu_0 H_{n3}$

Table 6.1: Four boundary conditions of the continuity requirements

6.3.3. Geometry

Before solving the Maxwell equations in each region with the boundary conditions, the geometry and the external magnetic field has to be defined.

- The external alternating magnetic field is homogenous distributed. Assuming a small area close to the conductor in figure 6.5 result in a small variation in direction and amplitude of the magnetic field.

- The shield is a hollow sphere with an inner radius r_0, metallic shield with thickness d and an outer space in figure 6.6. The inner and outer region is assumed to be in air.

- The spherical coordinate system (r, ϑ, φ) has the origin of the center of the sphere. In this system the field amplitudes are rotationally symmetrical to the z axis. Therefore the field is independent of φ [25]

Outer region

First the excitation source of alternating homogenous magnetic field in the outer region ($r \geq r_o + d$) is defined. The region is filled with air which allows the use of the scalar potential X_0 in figure 6.6. On this field an opposed magnetic field from the induced currents on the surface of the sphere is superimposed [25]. Here the opposed magnetic field is defined as the feedback field X_w, which results in the potential of equation 6.30.

$$X = X_0 + X_w = H_a \cdot z + X_w = H_a \cdot r \cdot cos\vartheta + X_w \tag{6.30}$$

The potential X can be determined by the Laplace operation of equation 6.23 by using the separation of variables $X = f(r) \cdot cos; \vartheta$. With the spherical coordinate system in figure 6.6 the cosinus is used such that for an angle of 0° the potential is maximum. Furthermore the Laplace operation with $\partial X / \partial \varphi = 0$ is stated in equation 6.32.

$$\nabla^2 X = 0 \tag{6.31}$$

$$\frac{1}{r^2} \frac{\partial}{\partial r} \left(r^2 \frac{\partial X}{\partial r} \right) + \frac{1}{r^2 sin \vartheta} \frac{\partial}{\partial \vartheta} \left(sin \vartheta \frac{\partial X}{\partial \vartheta} \right) + \frac{1}{r^2 sin^2 \vartheta} \frac{\partial^2 X}{\partial \varphi^2} = 0 \tag{6.32}$$

$$r^2 f''(r) + 2 r f'(r) - 2 f(r) = 0 \tag{6.33}$$

$$f(r) = C_1 r + \frac{C_2}{r^2} \tag{6.34}$$

Where C_1 and C_2 are the two constants to be find. The first constant follows from the excitation condition for long distances where the magnetic field returns into the homogenous magnetic field. The second constant has to contain the influence of the feedback field which can be solved with the boundary conditions. For now the feedback factor W is introduced. Therefore the solution of the potential for the outer region result in equation 6.35. Furthermore the magnetic field components in the spherical coordinate system are stated in equations 6.36 and 6.37.

$$X = H_a \left(r + \frac{(r_0 + d)^3}{r^2} W_e \right) cos \vartheta \qquad \text{for } r \geq r_0 + d \tag{6.35}$$

$$H_r = \frac{\partial X}{\partial r} = H_a \left(1 - \frac{2 (r_0 + d)^3}{r^3} W \right) cos \vartheta \qquad \text{for } r \geq r_0 + d \tag{6.36}$$

$$H_\theta = \frac{\partial X}{r \partial \vartheta} = -H_a \left(1 + \frac{(r_0 + d)^3}{r^3} W \right) sin \vartheta \qquad \text{for } r \geq r_0 + d \tag{6.37}$$

The magnetic field which is generated by the eddy currents in the outer region is proportional to the feedback factor. This field decrease with the power of three over the distance .
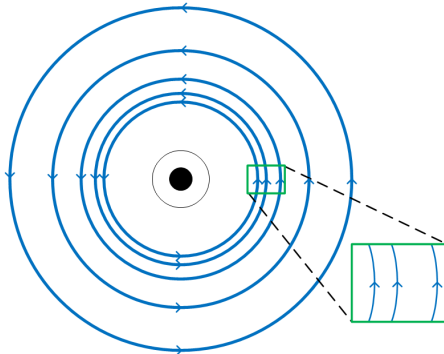
Figure 6.5: In close proximity the magnetic field is homogenous distributed
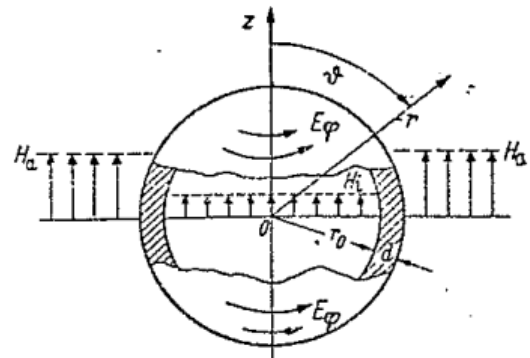
Figure 6.6: Hollow Thin walled sphere in homogenous alternating magnetic field [25]

INNER REGION

The second region for which the differential equation is solved is inside the shielding ($0 \leq r \leq r_0$). The magnetic field strength inside the shield following figure 6.6 is H_i. This field will be reduced compared to the outer region by the shielding factor Q in the equations 6.38 and 6.39.

$$H_r = H_i \cdot \cos\vartheta \qquad = Q \cdot H_a \cdot \cos\vartheta \qquad \text{for } 0 \leq r \leq r_0 \qquad (6.38)$$

$$H_\vartheta = -H_i \cdot \sin\vartheta \qquad = -Q \cdot H_a \cdot \sin\vartheta \qquad \text{for } 0 \leq r \leq r_0 \qquad (6.39)$$

At this moment the factor Q can not be solved without the field strengths of the shield region.

SHIELD REGION

The last region is the shield itself ($r_0 \leq r \leq r_0 + d$). In section 5.2 it was stated that the direction of the induced current oppose the original magnetic field. These currents and therefore the electric field must circulate around the z axis as seen in figure 6.6. Therefore the electric field has only one component in the φ direction.

In the shield region the differential equation of 6.28 has to be solved. First the electric field is separate in variables $E_\varphi = g(r) \cdot \sin\vartheta$. In respect with figure 6.6 the sinus is used instead of the cosines cause the magnetic flux increases for an increasing φ. Second the Laplace operator is applied in equation 6.41. The result is given in equation 6.42

$$\nabla^2 E_\varphi = 0 \qquad (6.40)$$

$$\frac{1}{r^2}\frac{\partial^2}{\partial r^2}(r^2 E_\varphi) + \frac{1}{r^2}\frac{\partial}{\partial\varphi}\left(\frac{1}{\sin\varphi}\frac{\partial}{\partial\varphi}(\sin\varphi\, E_\varphi)\right) - k^2 E_\varphi = 0 \qquad (6.41)$$

$$g''(r) - \frac{2}{r}g'(r) - \left(\frac{2}{r^2} + k^2\right)g(r) = 0 \qquad (6.42)$$

$$(6.43)$$

The solution of the Laplace operation in equation 6.42 can be simplified. The shield thickness d is much smaller than the sphere radius r_0. Assuming the shield is a thin wall the components of $1/r$ and $1/r^2$ can be disregarded in equation 6.44 [25]. The solution of this second order differential equation is an exponential function in equation 6.45

$$g''(r) - k^2 g(r) = 0 \qquad (6.44)$$

$$g(r) = C_3 e^{kr} + C_4 e^{-kr} \qquad (6.45)$$

Where C_3 and C_4 are the two constant which has to be found with the boundary conditions. First the electric field is transformed by equation 6.19 to the magnetic field components of the spherical coordinate system in equations 6.47 and 6.48 .

$$E_\varphi = (C_3 e^{kr} + C_4 e^{-kr})\sin\vartheta \qquad\qquad \text{for } r_0 \leq r \leq r_0 + d \qquad (6.46)$$

$$H_r = -\frac{1}{j\omega\cdot\mu\cdot r_0\cdot\sin\vartheta}\frac{\partial}{\partial\vartheta}(\sin\vartheta\, E_\varphi) = -\frac{2}{j\omega\cdot\mu\cdot r_0}(Ae^{kr} + Be^{-kr})\cos\vartheta \qquad \text{for } r_0 \leq r \leq r_0 + d \qquad (6.47)$$

$$H_\vartheta = \frac{1}{j\omega\cdot\mu}\frac{\partial E_\varphi}{\partial r} = \frac{k}{j\omega\cdot\mu}(Ae^{kr} - Be^{-kr})\sin\vartheta \qquad\qquad \text{for } r_0 \leq r \leq r_0 + d \qquad (6.48)$$

TRANSITIONS

The magnetic field components are defined in all the regions in the spherical coordinate system. However there are four unknowns left: the constants C_3, C_4, the feedback factor W and shielding factor Q. Therefore continuity requirements are applied between the two transition regions from table 6.1 . The first region is between the shield and the outer region. Second transition region is between the shield and inner region.

The first transition region combines the equations of the sections 6.3.3 and 6.3.3. The tangential and normal components of both regions are combined in equations 6.49 and 6.50 respectively for $r = r_0 + d$.

$$H_a(1 - 2W) = \frac{2}{j\omega\mu r_0}(C_3 e^{k\cdot(r_0+d)} + C_4 e^{-k\cdot(r_0+d)}) \tag{6.49}$$

$$\mu_0 \cdot H_a(1 + W) = \mu \cdot \frac{k}{j\omega\mu}(C_3 e^{k\cdot(r_0+d)} - C_4 e^{-k\cdot(r_0+d)}) \tag{6.50}$$

The second transition region combines the equations of the sections 6.3.3 and 6.3.3. Again the tangential and normal components are combined in equations 6.51 and 6.52 respectively for in for $r = r_0$.

$$Q \cdot H_a = \frac{2}{j\omega\mu r_0}(C_3 e^{kr_0} + C_4 e^{-kr_0}) \tag{6.51}$$

$$\mu_0 Q \cdot H_a = \mu \cdot \frac{k}{j\omega\mu}(C_3 e^{kr_0} - C_4 e^{-kr_0}) \tag{6.52}$$

The equations for both transition regions allows to solve the unknowns for the second order differential equations. So simplify the derivations the substitutions of equation 6.53 are used. What remains are four equations with four unknowns in 6.54. The solutions for the feedback and shielding factor are stated in equations 6.55 and 6.56 respectively.

$$A = \frac{e^{kr_0}}{j\omega \cdot \mu \cdot r_0 \cdot H_a}, \quad B = \frac{e^{-kr_0}}{j\omega \cdot \mu \cdot r_0 \cdot H_a}, \quad K = \frac{k \cdot \mu}{\mu_0 \cdot r_0} = \frac{\mu_r \cdot k}{r_0} \tag{6.53}$$

$$1 - 2W = 2(Ae^{kd} + Be^{-kd}) \qquad 1 + W = K(Ae^{kd} - Be^{-kd}) \tag{6.54}$$
$$Q = 2(A + B) \qquad Q = K(A - B)$$

$$W = \frac{\frac{1}{3}\left(\frac{K}{2} - \frac{2}{K}\right)\sinh kd}{\cosh kd + \frac{1}{3}\left(K + \frac{2}{K}\right)\sinh kd} \tag{6.55}$$

$$Q = \frac{1}{\cosh kd + \frac{1}{3}\left(K + \frac{2}{K}\right)\sinh kd} \tag{6.56}$$

To apply the shielding factor for applications the shielding effectiveness has to be derived. This is a mathematically transformation and can be read in Appendix B.3. The result is the shielding effectiveness SE in equation 6.57 expressed in dB.

$$SE = \frac{1}{2}ln[\frac{1}{9}[(\frac{r_0}{\mu_r\delta})^2 + (\frac{\mu_r\delta}{r_0})^2](\cosh\frac{2d}{\delta} - \cos\frac{2d}{\delta})$$
$$+ \frac{r_0}{3\mu_r\delta}(\sinh\frac{2d}{\delta} - \sin\frac{2d}{\delta}) + \frac{\mu_r\delta}{3r_0}(\sinh\frac{2d}{\delta} + \sin\frac{2d}{\delta})$$
$$+ \frac{1}{2}\cosh\frac{2d}{\delta} + \cos\frac{2d}{\delta})] \tag{6.57}$$

6.4. MATERIALS

The shielding effectiveness of equation 6.57 depends on the size of the sphere, the frequency of the homogenous alternating magnetic field and the the thickness and skin depth of the material. The radius of the sphere is chosen to be 105 mm. Later in section 8.3 this radius will also be used to analyze the prototype. Furthermore in order to reduce the magnetic field with 50.1 dB (section 5.3) four materials are analyzed: aluminum, copper, steel and mu-metal. The conductivity σ and relative permeability μ_r of these materials are summarized in table 6.2 [21] [27]. For each material the skin depths, the shield effectiveness in case of 1 mm thickness and the shield effectiveness at 50 Hz will be considered.

In this chapter the skin depth σ of equation 6.58 has been mentioned several times. It is know that the skin depth is the distant through which an electromagnetic wave amplitude is decreased by a factor e^{-1} (37%). While the conductivity of steel and mu-metal are lower than copper and aluminum, the relative permeability are many times higher. Therefore for any frequency the skin depth of steel and mu-metal are lower than copper and aluminum as can be seen in figure 6.7. For high frequencies the skin depth of all materials become very small.

$$\delta = \sqrt{\frac{1}{\pi \cdot f \cdot \mu_r \mu_0 \cdot \sigma}} \tag{6.58}$$

MAGNETIC SATURATION

However the relative permeability of mu-metal and steel depend on the presence of the external magnetic field. These materials are ferromagnetic and interact strongly by aligning their magnetic dipole [15]. However these materials can saturate when the external field is too high in which case the electrons spins are aligned. As result their relative permeability drops. Fortunately the magnetic field in which mu-metal saturates is approximately 760 mT [27] while steel saturates 1.6 T. As seen earlier the magnetic field remain far below these values. Therefore saturation is not considered further.

Second for practical application the materials will be compared when by using a 1 mm shield thickness in figure 6.8. At low frequencies the shield effectiveness remain constant, then increases slowly (not in the case of steel and mu-metal due to their high relative permeability) and last increases fast at high frequencies. These three phenomenas can be explained as follow:

- In case the *SE* remains constant at low frequencies the magnetic field lines are absorbed by the shield due to the low reluctance path it provides.

- The thickness of the shield and skin depth becomes equal. Induced currents starts to reflect the magnetic field lines by their own induced magnetic field lines the frequency is stated in table 6.2.

- Induced currents flow closer to the surface of the shield due to decreased skin depth. The magnetic field lines are reflected.

Last the frequency of the magnetic field which has to be reduce is 50 Hz. In figure 6.9 the *SE* over several shield thicknesses are considered. In the previous chapter the required *SE* was determined to be 50.1 dB. Due to the characteristics of the materials at this frequency only mu-metal with 1.25 mm thickness can reduce the magnetic field of 3.2 mT to 10 μT in a sphere with a radius of 105 mm.

	ρ $(\Omega \cdot m)$	σ $(S \cdot m^{-1})$	μ_r	δ * (mm)	$f_{d=\delta}$ (Hz)	SE ** (dB)
Aluminum	$28.3 \cdot 10^{-9}$	$35.34 \cdot 10^6$	1	11.97	$7.2 \cdot 10^3$	0.99
Copper	$17.2 \cdot 10^{-9}$	$58.14 \cdot 10^6$	1	9.33	$4.35 \cdot 10^3$	2.22
Steel	$101 \cdot 10^{-9}$	$9.90 \cdot 10^6$	180	1.68	142.1	6.83
Mu-metal	$700 \cdot 10^{-9}$	$1.43 \cdot 10^6$	20.000	0.42	8.9	46.37

Table 6.2: Conductivity and relative permeability from different metals. (* Skin deth value at 50 Hz, ** SE at 50 Hz and 1 mm thickness)
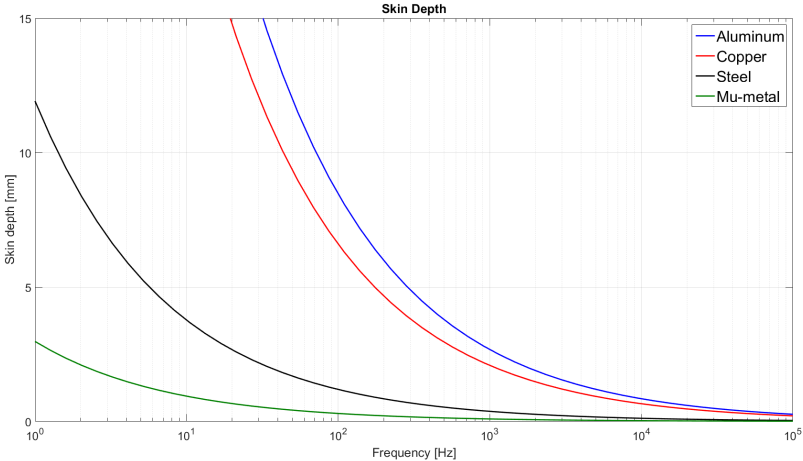
Figure 6.7: The skin depth against the frequency with the parameters of table 6.2
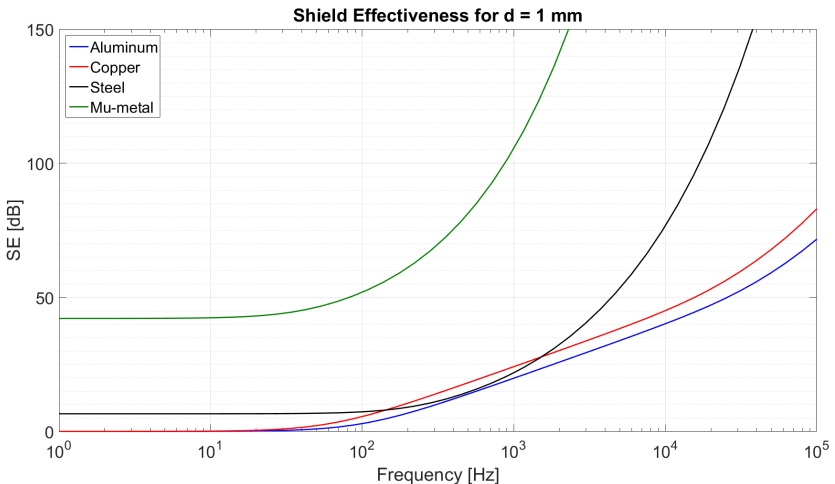
Figure 6.8: The shielding effectiveness for a 1 mm shield over several frequencies. Magnetic field lines are absorbed or repelled by the shield
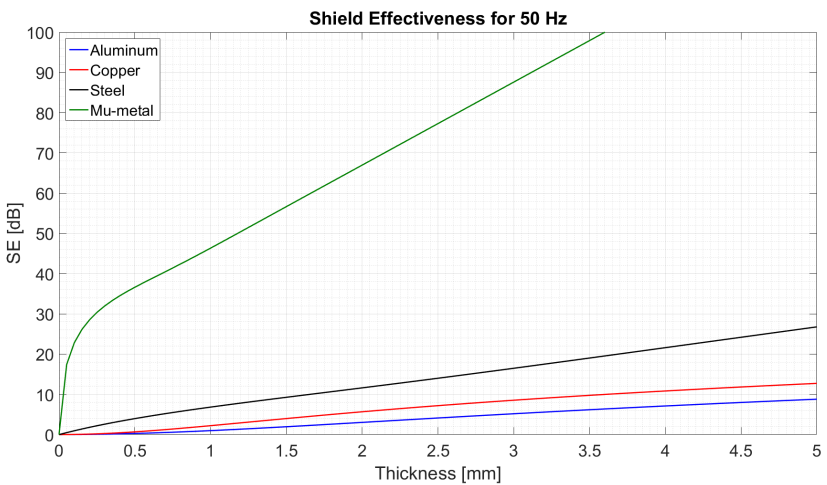
Figure 6.9: The shielding effectiveness for 50 Hz over several shield thicknesses

6.5. HOLES

The shielding effectiveness was determined for a closed enclosure. However openings in the form of holes and slots will effect the shielding capabilities. However these holes may be necessary for air ventilation or opening mechanisms. Welding joints can also be a result in an opening in the enclosure [21]. In either case the path of the induced current is interrupted at the surface of the shield. Furthermore an electromagnetic wave with a frequency higher than the cutoff frequency f_c can enter the enclosure. Assuming a rectangular slot with length d. The cutoff frequency is determined by equation 6.59 [28].

$$f_c = \frac{c}{2 \cdot d} \tag{6.59}$$

The path of induced current in respect to a slot can be seen in figure 6.10. The currents on the surface have to go around in order to propagate. The induced currents reflect the magnetic field due to their own induced magnetic field. Therefore re-routing the induced currents result in a reduced shielding effectiveness [17]. The new route of the induced current is mostly increased when the slot is placed orthogonal in respect to the path.
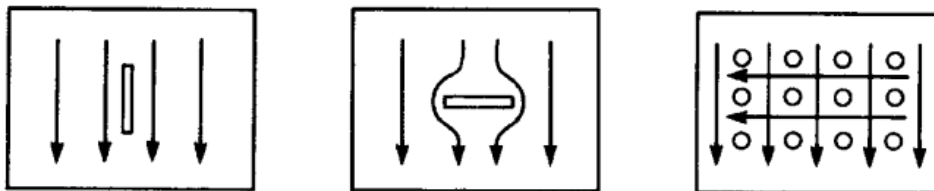
Figure 6.10: The path of induced current on the surface will be increased by a slot [17]

6.6. ELECTRICAL CONCEPT CONCLUSIONS

The goal of this chapter was to examine the theory to reduce an external low frequency magnetic field.
First the impedance method was analyzed and resulted in the insight of reflection and absorption of an electromagnetic waves. However this theory was not applicable for practical cases. Next electric shielding was discussed. The section explained that electromagnetic waves form almost all frequencies are blocked by the enclosure. After electric shielding magnetic shielding was considered. In order to determine the shielding effectiveness a second order differential equation has to be solved for each region. As result an expression was found which depends from the radius of the volume to be protected, frequency and material properties. Aluminum, copper, steel and mu-metal were considered. Only mu-metal of 1.25 mm thickness is able to reduce the magnetic field by 50.1 dB as seen in table 6.2. Last the effective of holes and slot were considered.

In a later chapter the actual magnetic field inside an enclosure without and with a shield will be measured for a single conductor. But first in the next chapter a slot will be placed deliberately in order to transmit data.

7

PROTOTYPE ANTENNA CONCEPT

Contents

In the previous section the shielding effectiveness for the prototype was discussed. However adding slots and holes may be required for other applications like openings for antenna connections. In order to apply DLR the measured data from the real-time monitoring system has to be transferred to a central location. An antenna located close to an overhead line has to be able to transmit data.

The goal of this chapter is to design an antenna for the 868 MHz. First noise form the overhead line which can interference with the antenna signal is examine. Second several antennas are evaluated in section 7.2. Furthermore the characteristics of the chosen antenna is examine in section 7.3.

7.1. OVERHEAD LINE NOISE

The real-time monitoring system will be placed on the overhead line. Due to the small distant electric and magnetic shielding was discussed in the previous chapter. However the mean frequency for shielding was 50 Hz while the communication operates at 868 MHz.

The source of radio noise from the overhead lines are spark gaps and corona discharges [29]. Discharges from a spark occurs in case the breakdown voltage over a gap is exceeded. Corona is a partial discharge when the voltage increases above inception voltag and thereby result in a too high voltage gradient [30]. In [29] spark gaps and corona discharges where measured for overhead lines up to 345 kV and 1 GHz. These measurements concluded that radio noise from either corona nor spark gap discharges were significant, but were measured 200 feet($\approx$ 61 m) away from the conductor. Furthermore discharges from spark gaps can be

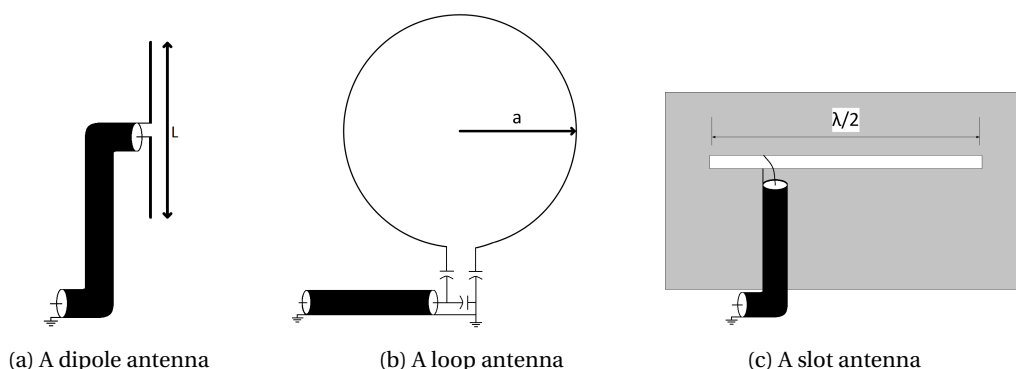(a) A dipole antenna   (b) A loop antenna   (c) A slot antenna

Figure 7.1: The three antennas which will be compared with each other

found and removed. To test the reliability of the communication an antenna has to be selected and tested in the presences of corona discharges.

7.2. ANTENNA COMPARISON

Furthermore the real-time monitoring system requires an antenna to send its measured data. This antenna can be installed at three locations: inside the enclosure where the electronics are also installed, outside the enclosure or in the enclosure itself. First an antenna inside the enclosure is examine.

The antenna has to operate at a frequency of 868 MHz. For this frequency the shielding effectiveness can be determined with the figures 6.2 and 6.3. As can be seen for this frequency both the electric and magnetic shielding effectiveness is high. Therefore the electromagnetic wave from the antenna can not pas through the enclosure.

An antenna on the outside of the enclosure can be done by several antennas. Two wire based antennas are compared: the dipole and loop antenna. The last position where an antenna can be placed is in the enclosure itself. By making a slit in the enclosure an slot antenna is made. The dipole, loop and slot antenna are roughly compared in table 7.1. Each antenna will be reviewed by first discussing their functionality, second the advantages and last the disadvantages. The antennas are compared based on the ease of use, affected by expected noise and radiation resistance. The radiation resistance and reactance provide an inside of the efficiency.

7.2.1. DIPOLE ANTENNA

The dipole antenna is a wire type antenna fed at center as can be seen in figure 7.1a. The length L of the dipole antenna consist of two parts and is a half wavelength long. This result in a length of 17,3 cm. The size of an dipole antenna can be reduced by connecting half of the antenna to a ground plane. This also called a quarter wave monopole [31]. The advantages of this antenna type are the size and simplicity to manufacture. Furthermore the radiation resistance and reactance of dipole antenna is approximately 70 Ω and zero respectively [31]. A source impedance is normally 50 Ω. Therefore only a very small impedance mismatch will occur. In case of a mismatch energy is reflected back to the source and is dissipated lost as heat.

However the shape of an dipole/monopole can become a problem when placed close to an overhead line. At the end side of the dipole antenna the wires are open circuit. These wires have a certain radius and can be seen as a sharp edge. On a sharp edge corona discharges can be generated when the absolute voltage is higher than the inception voltage. The inception voltage depends on the radius of the end wire [30]. Applying the dipole antenna for the real time monitoring system will generate losses in the form of corona discharges. These losses has to be avoided.

7.2.2. LOOP ANTENNA

The loop antenna is a wire type antenna and forms a close loop as can be seen in figure 7.1b. Other forms like a square or octagon are also possible as long as the current has a constant distributed along the loop. For a small loop antenna the radius a has to be smaller than $0.03 \cdot \lambda$ [32]. The loop is due to its geometry highly inductive. Therefore the electromagnetic wave is dominated by the magnetic field and will not be affected by electric interference [33].

The high inductive reactance requires capacitors to tune the antenna. Furthermore the bandwidth of a loop antenna is narrow which makes tuning difficult. The radiation resistance of a loop antenna is very small and is less than 1 Ω while the reactance is very high. Even with the use of capacitors to match with the 50 Ω source impedance very little active power can be delivered from the source to the antenna. Loop antenna are therefore mostly used as receiving antennas [34].

	Dipole/monopole	Loop	Slot
Complexity	Simple (+)	Tuning capacitors (-)	Feed-in placement (+)
Noise level	Corona (-)	Electric immune (+)	Neutral (0)
$R_r^{(1)}$	73/36.5 Ω (+)	<1Ω (-)	Feed-in placement (+)

Table 7.1: Overall comparison between the dipole, loop and slot antenna.
1: radiation resistance. 2: When feed-in placed correctly

7.2.3. SLOT ANTENNA

The slot antenna is an aperture antenna and use a metallic surface as can be seen in figure 7.1c. The slot is a half wavelength long and is fed at approximately a quarter wavelength from the side. This feed-in placement follows from the antenna impedance. If feed in the center the impedance will be approximately 500 Ω [35], which follows from the relation between the slot and complementary dipole in equation 7.1.

$$R_{r(dipole)} \cdot R_{r(slot)} = \frac{\eta_0^2}{4} \tag{7.1}$$

However connection at the side of the slot result in a impedance of approximately 0 Ω because here the circuit is short-circuited. Therefore feeding the antenna between these two positions allows to match the source impedance. The only disadvantage is the dimension of slot which can make it difficult or impractical to manage [36]. In case of the real time monitoring device the wavelength will be 0.3456 m. The length of the slot will be 172.8 mm long .

7.3. DESIGN ANTENNA

The antenna which will be used for the prototype is the slot antenna. This antenna can be made out of any metallic surface and is relative easily to tune. The characteristics of the antenna depend on the length, width W and feed-in location L as can be seen in figure 7.2. In this section the width and feed-in location are considered. The length of the slot has chosen to be fixed at $0.5 \cdot \lambda$. Because the resonant frequency is determined by the circumference of the slot. The width is assumed electrical small and has to be smaller then $1/20 \cdot \lambda$ [34]. In this case a current is short circuit and the voltage zero at the ends of the slot .

Before examining the feed-in location and width of the slot antenna the measurement method will be discussed. As discussed in section 6.1.1 an incident wave can be transmitted or reflected when it encounter a different medium. An antenna radiates an electromagnetic wave by applying an current to its terminals. This energy is transmitted mostly at the resonance frequency. Energy at other frequencies are reflected back. Measuring the reflection of an antenna provide insight in which frequency the antenna losses its energy. Therefore a high negative reflection means that energy is mostly transmitted at this frequency.

The feed-in is located at a distance L from the left side. As discussed in the previous section the antenna impedance will be maximum in the center and minimum at the end sides of the slot. Therefore first between these two extremism will be considered. The starting position of the feed-in location is a at $0.125 \cdot \lambda$. Furthermore the feed-in positions of 1 cm larger and smaller are examine in figure 7.3. The results are summarized in table 7.2. It can be concluded that moving the feed-in location result in shifting the resonance frequency, but does not not influence the magnitude of the reflection. The lowest reflection coefficient (most energy transmitted) at 868 MHz is found in case of a feed-in location at 43.2 mm and has a magnitude of -12 dB.
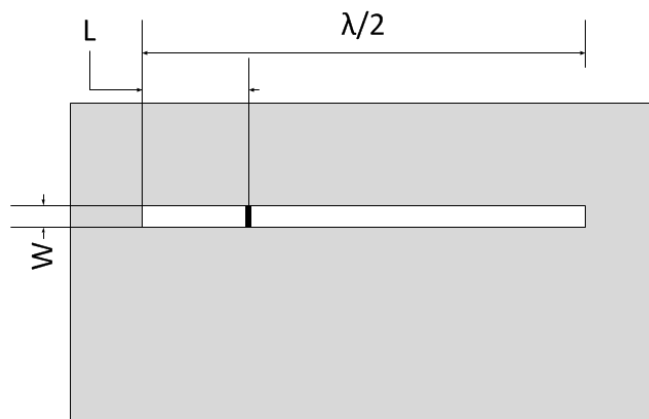
Figure 7.2: Slot antenna with a fixed length and a variated feed-in distance L and width W.

Next the width of the slot W is considered. First the reflection coefficient with a width of $1/20 \cdot \lambda$. Decreasing the width result in figure 7.4 and is summarized in table 7.3. In this case both the resonance frequency as the magnitude of the reflection coefficient changes. It can be concluded that a smaller width of the slot decrease both the resonance frequency as the reflection coefficient magnitude. Here the lowest reflection coefficient at 868 MHz is at a width of 8.6 mm and has a magnitude of -15 dB.

7.4. PROTOTYPE ANTENNA CONCLUSIONS

The goal of this chapter was to design an antenna which could be use in an overhead line environment and transmitted most of its energy at 868 MHz. Radio noise from the overhead line is formed by spark gaps and corona discharges. Only by own tests the reliability of the communication can be concluded.

Three antennas were considered to be used for the real time monitoring system. A dipole antenna cannot be used do to its sharp end which can increase corona discharges at high voltage. A loop antenna is by its tuning and radiation resistance impractically to use as transmitting antenna. However the slot antenna can easily be made and tuned. This antenna was further analyzed by its feed-in position and width of the slot. In ideal case a slot with a small width should be chosen. In order to transmit most of the energy at the resonance frequency the position of the feed-in location has to be shifted.

In the next chapter a slot of approximately $L = 0.125 \cdot \lambda$ and $W = 0.025 \cdot \lambda$ is made in a metallic enclosure to test for its characteristics and reliability under corona discharges.
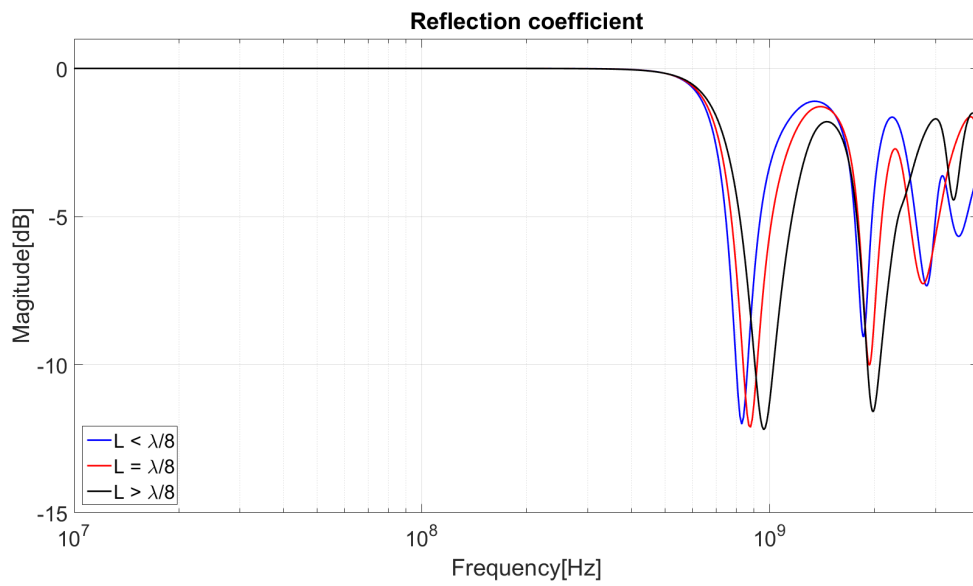
Figure 7.3: Influence of different feed-in locations. L < $\lambda/8$ = 33.2 mm, L = $\lambda/8$ = 43.2 mm and L > $\lambda/8$ = 53.2 mm. The width of the slot wasset to $\lambda/40$.

	L < $\lambda/8$	L = $\lambda/8$	L > $\lambda/8$
Resonant Frequency	830.2 MHz	880.2 MHz	960.2 MHz
Magnitude	-12.0 dB	-12.1 dB	-12.2 dB

Table 7.2: Resonance frequency and magnitude of figure 7.3
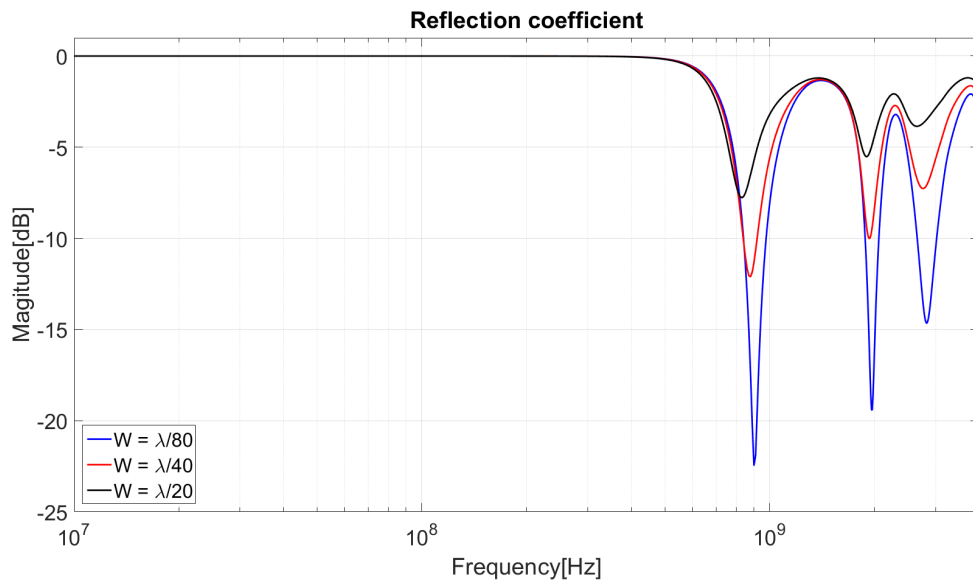
Figure 7.4: Influence of different width of the slot. W = $\lambda/80$ = 4.3 mm, W = $\lambda/40$ = 8.6 mm and W = $\lambda/20$ = 17.3 mm. The feed-in location was set as $\lambda/8$.

	W = $\lambda/80$	W = $\lambda/40$	W = $\lambda/20$
Resonant Frequency	900.2 MHz	880.2 MHz	830.2 MHz
Magnitude	-22.5 dB	-12.1 dB	-7.8 dB

Table 7.3: Resonance frequency and magnitude of figure 7.4

8

PROTOTYPE ANALYSIS

Contents

In the previous chapters the shield effectiveness and antenna concepts were explained. The goal of this chapter is to test a prototype and find its characteristics in respect to shielding and communication. For these tests the setup of Appendix A is used.

First the prototype is discussed. Second the thermal behavior of the prototype and conductor are analyzed. Third the capability of reducing the magnetic field is determined and comparing the theory and simulations. Last the prototype antenna characteristics and functionality is tested in different environments.

8.1. PROTOTYPE

The prototype has the dimensions of 200x200x120 mm and consist of hollow rectangular box with a cover which is the box by the use of screws. This size was chosen in order place the antenna slot and allows a magnetic field probe inside. Furthermore the box is made from sheet steel and has a thickness of 1 mm. In the cover from the prototype the slot is made. The length of the slot is 172 mm has a width of 8.0 mm and is feed-in 40.5 mm from the side. Furthermore a stainless steel plate of 230x125x2 mm is used for the first test. The dimensions of slot antenna in this plate is 172.5 mm by 8.6 mm and has a feed-in position of 41 mm. Both the prototype and the stainless steel plate can be seen in Appendix C

8.2. THERMAL ANALYSIS

In chapter 3 the thermal behavior of the conductor was examined. Furthermore it was shown that induced currents will reduces the external magnetic field. However these currents can also heat up the prototype.

The goal of this chapter is to determine the end temperature on the surface of the prototype and conductor in case a current flows through the conductor. First measurement equipment is discussed. Then the conductor and prototype temperature are measured and evaluated.

8.2.1. THERMOCOUPLES

Measuring the temperature will be done by the use of thermocouples. A thermocouple determines the temperature by translating a potential difference between two different metals. This potential is caused by the movement of charges from one metal to the other when a temperature is applied. The used thermocouple

consist of metals copper and constantan (T-type). A standard T-type as a accuracy of ±1°C [37].

8.2.2. THERMAL RESULTS

The thermal behavior will be examine in case 800 A through the conductor is applied at t = 0. Before t = 0 the conductor was at room temperature. The prototype is located 0.5 cm away from the conductor. Every 5 minutes a sample is saved in which the current and temperatures are recorded until the temperature of the conductor is in thermal equilibrium. This means the temperature does not change more than ±1° over 60 minutes. The result can be seen in figure 8.1 and is summarized in table 8.1. During the test several observation are made. First the current through the conductor is decreased by 8 A. This can be explained by section 3.1.1. An increase of temperature result in a increase of resistivity following equation 3.5.

The temperature of the prototype increases with 1.9 °C. This increase is caused by heat transfer from the conductor. In chapter 3 heat can be generated by Joule heating. Induced currents heats up the prototype by I^2R. However due to the small distance between the prototype and conductor heat is transferred by natural convection or radiation. However no wind was measured during the test. Heat transfer by radiation is more likely. Lastly measurement inaccuracy for a standard T-type thermocouple was ± 1 °C. In conclusion of the thermal analysis the conductor reaches thermal equilibrium in 150 minutes and increases with 34.9 °C. The prototype only increased 1.9 °C by heat transfer in the form of radiation.

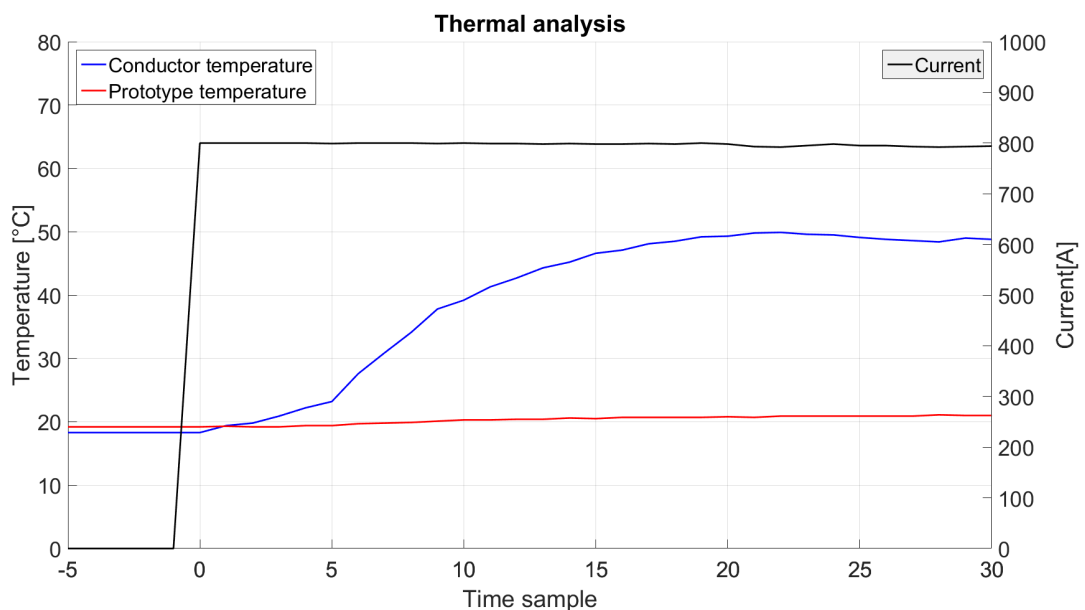|	$I_{conductor}$	$T_{conductor}$	$T_{prototype}$
Begin	800 A	18.4 °C	19.2 °C
End	792 A	53.3 °C	21.1 °C

Table 8.1: Results temperature analysis

Figure 8.1: Thermal analysis of conductor(blue) and prototype(red) of a current(black) at t=0. Each sample is taken at steps of 5 minutes

8.3. SHIELDING ANALYSIS

In section 6.3 the theory behind low frequency magnetic shielding was discussed. The goal if this section is to validating the shielding theory by simulation and measurements with the prototype.

First the prototype characteristics will be used in theory and simulation. Second the magnetic field is measured with and without the prototype. This test was performed before cutting out the slot antenna. Third the effect of the slot antenna will be simulated. Last the magnetic field is measured again however now with the slot. The measurements require a test setup which is explained in Appendix A. This test setup includes a analysis of inductance reduction.

In order to apply the theory of shielding the geometry of the prototype has to be addressed first. In section 6.3.3 the geometry of the shielded enclosure was a sphere. However the prototype has a rectangular shape. The shielding effectiveness of a rectangular can be approximated by a sphere with the same volume [21]. The radius of the sphere is determined by equation 8.1.

$$200 \, \text{mm} \times 200 \, \text{mm} \times 120 \, \text{mm} = \frac{4}{3} \pi r^3 \quad \rightarrow \quad r = 105 \, \text{mm} \tag{8.1}$$

The shielding effectiveness from a sphere with a radius of 105 mm, 50 Hz and 1 mm thickness of steel is 6.83 dB as can be obtained with equation 6.57. The simulation of this sphere resulted in figure 8.2. For the simulation the sphere was exposed to an homogenous alternating magnetic field of 1.0 mT. The shielding effectiveness was determined by measuring the magnetic flux density at the origin of the sphere.The magnetic field at the center of the sphere is 0.4556 mT. The shielding effectiveness can be calculated with equation 5.10 and result in 6.81 dB.

The found theoretical and simulate value of the shielding effectiveness result in a difference of 0.02 dB. To understand the influence of this difference the magnetic field inside the sphere is re-calculated. In case of a shielding effectiveness of 6.83 dB the magnetic flux density will be reduced by 0.1 μT in case of an external magnetic field of 1 mT. Therefore the difference in shielding effectiveness can be disregarded.
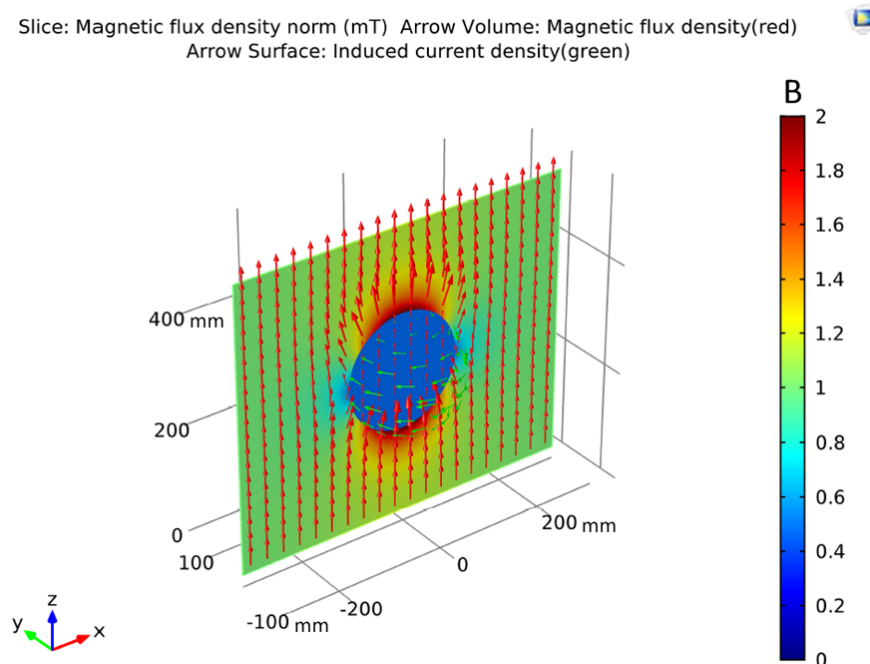
Figure 8.2: Sphere in homogenous alternating field.

8.3.1. MAGNETIC FIELD PROBE

To determine the shielding effectiveness in case of testing the measurement equipments has to be introduced. To measure the magnetic field the analyzer probe PMM EHP-50A was used. This probe has three inductors inside in order to determine x, y and z component of the magnetic field. The most important specification of the probe are the range of 10 nT and 10 mT, resolution 1 nT, sensitivity of 10 nT and absolute error of $\pm$ dB at 50 Hz and 0.1 mT [38].

8.3.2. SHIELDING RESULTS OF PROTOTYPE WITHOUT SLOT

The magnetic flux density inside and out the prototype is measured by placing the probe and the prototype(with the probe inside) at several distances from the conductor. Each time the 800 A is applied thorugh the conductor. This result in figure 8.11. The magnetic flux density without the prototype B_0 shows the same curve as figure 5.4: an exponential decrease in case of increased distance. The magnetic flux density inside the prototype B_p is reduced. In table 8.2 the measurements of the 800 A is summarized. The shielding effectiveness is also reduced over the distance. In section 6.4 it was explained that shielding form the magnetic field of 50 Hz in case of a steel shield follows from ferromagnetic characteristics of the material. Steel is not able to reduce the external magnetic field by 50.1 dB at 50 Hz with a thickness less than 5 mm.

Distance (cm)	B_0 (μT)	B_p (μT)	SE (dB)
5	1340	242	14.8
7.5	1050	232	13.1
10	839	220	11.6
15	640	192	10.5
20	517	170	9.66
30	361	130	8.87
40	269	104	8.65
50	210	792	8.47

Table 8.2: Measurements in the case of 800 A

Figure 8.3: Magnetic field measurement without and with shield at several distances and current levels from the conductor.

8.3.3. SLOT ANTENNA IN SIMULATIONS

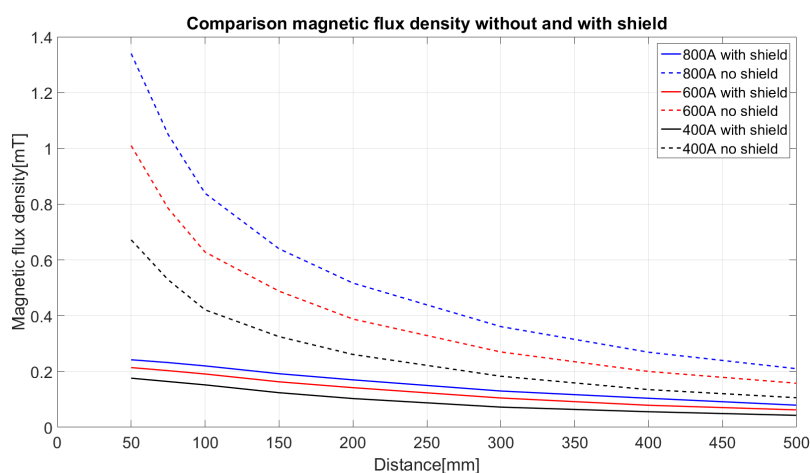In section 6.5 the effect of a slot on the surface was introduced. Later in section 7.3 a slot is required to transfer the data. Several simulations are made in order to analyze the path of the induced current on the surface of the prototype. In each simulation the following parameters are visualized:

- Geometries are in a mm scale.

- Red arrows are the magnetic field lines.

- Green arrows are the induced currents.

- Rainbow color slice (**B**) is the magnetic flux density in mT.

- Thermal color surface (**H**) is electromagnetic heating in Wm^{-3}.

First simulations in a 1 mT homogenous magnetic field for a sphere and the prototype are considered in figure 8.2 and 8.4 respectively. The simulations show a similar result: The magnetic field lines are absorbed by the shield and the path of the induced current are in clock-wise direction. The magnetic flux density is highest where the field lines enter the shield and the lowest in case of their absence. The electromagnetic heating result from the induced current density at the surfaces and is the highest at the edges of the prototype.

Second the prototype is exposed to the magnetic field from a straight conductor in figure 8.5. The magnetic field lines will encircle the conductor like figure 5.1. The electromagnetic heating is the highest close to the conductor in the xy plane and lowest in the yz plane.

Next in the following simulations the slot antenna is placed in the xz plane horizontal and vertical in figures 8.6 and 8.7. Furthermore placing the slot antenna in the yz plane horizontal and vertical result in the figures 8.8 and 8.9. In each simulation the slot antenna interrupt the path of the induced currents. When this occurs the current density is increased and result in a higher electromagnetic heating. From the figures the electromagnetic heating is increased the least in case of a vertical slot in the yz plane of figure 8.9. Therefore this placement of the slot in respect to the conductor is preferred.

8.3.4. SHIELDING RESULTS OF PROTOTYPE WITH SLOT

Shielding from the magnetic field lines in respect to the position of the slot will now be measured over the distances. The slot is located in the same position as in the simulations. The geometries are shown in the figures of 8.10. The measurements of the magnetic flux density is done by shifting the box over the distances in the several positions. Each time the current through the conductor is set to 800 A. The measurement results are shown in figure 8.11. It is obtained that a slot placed in the yz plane vertically reduce the magnetic flux density the least. In case of a steel enclose at 50 Hz frequency the magnetic field lines are absorbed by the enclosure. The presence of the slot will reduce the shielding effectiveness. The magnetic field which surrounds the conductor in circles was shown in figure 5.1. Furthermore in section 5.1 it was shown that the magnetic field reduces inversely proportional by the distance. The figures of 8.10 visualize that the magnetic field lines are orthogonal on the slot in the yz plane while parallel in the xz plane. It can be concluded that the magnetic field lines in case of the yz are less absorbed by the prototype. Furthermore magnetic field lines encounter the vertical slot in yz at the smallest distant. Therefore result in the smallest shield effectiveness and the highest remaining magnetic flux density in the prototype.
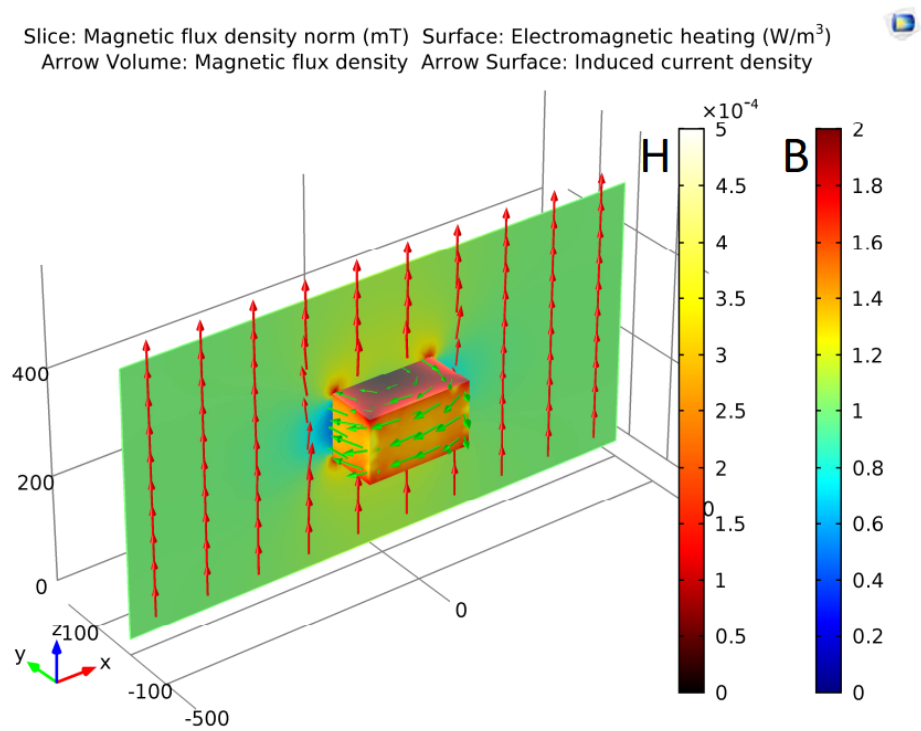
Figure 8.4: Prototype under a homogenous alternating magnetic field. The path of the induced current os in clock wise direction. Electromagnetic heating mostly occur at the corners.
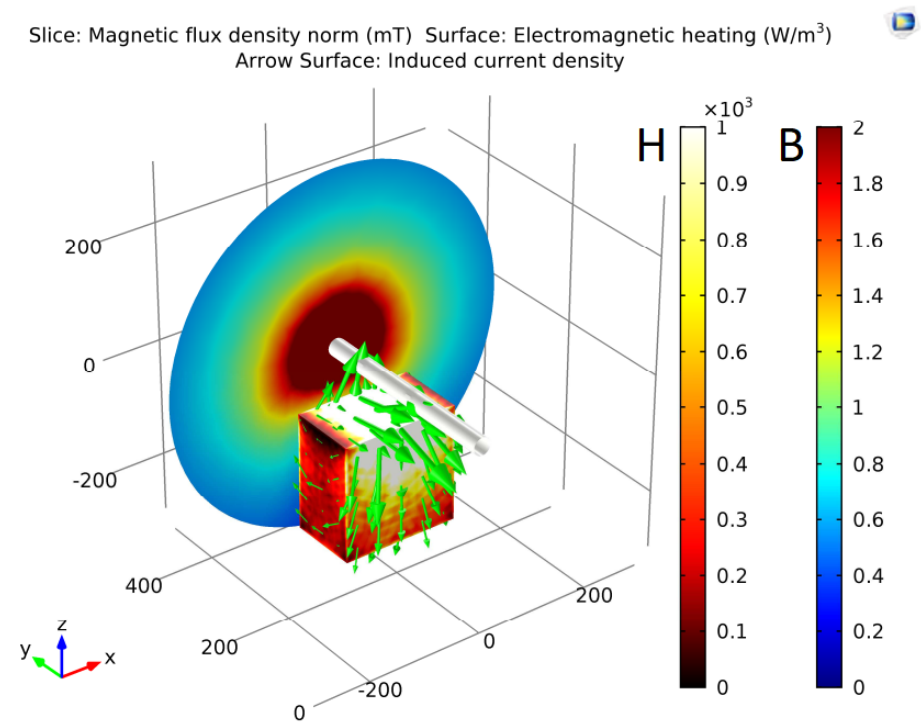
Figure 8.5: Prototype under an alternating magnetic field. The induced currents and electromagnetic heating are the high at the surface which is the closest to the conductor.
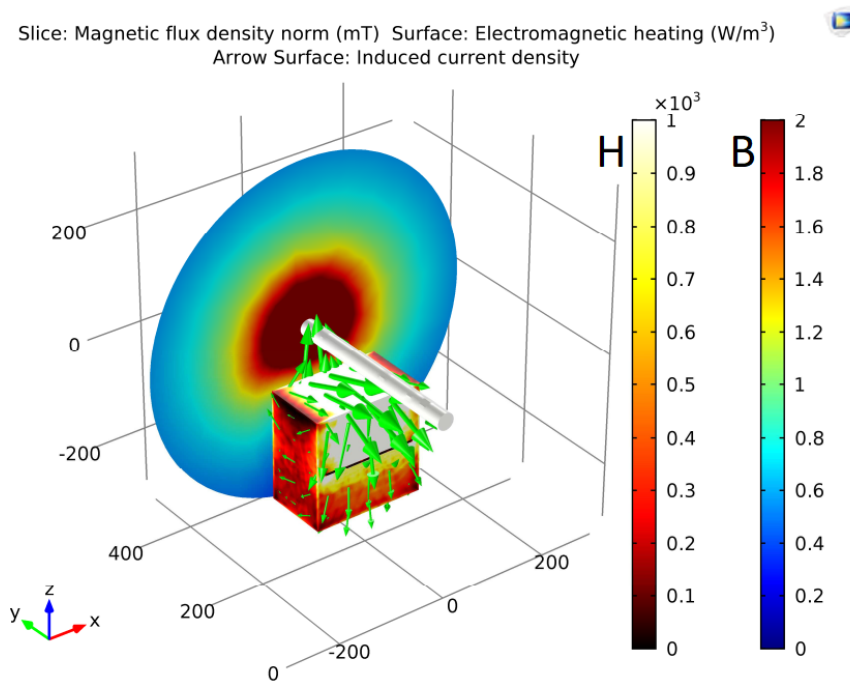
Figure 8.6: Horizontal slot antenna in the xz plane. The electromagnetic heating increases below at the end of the slot
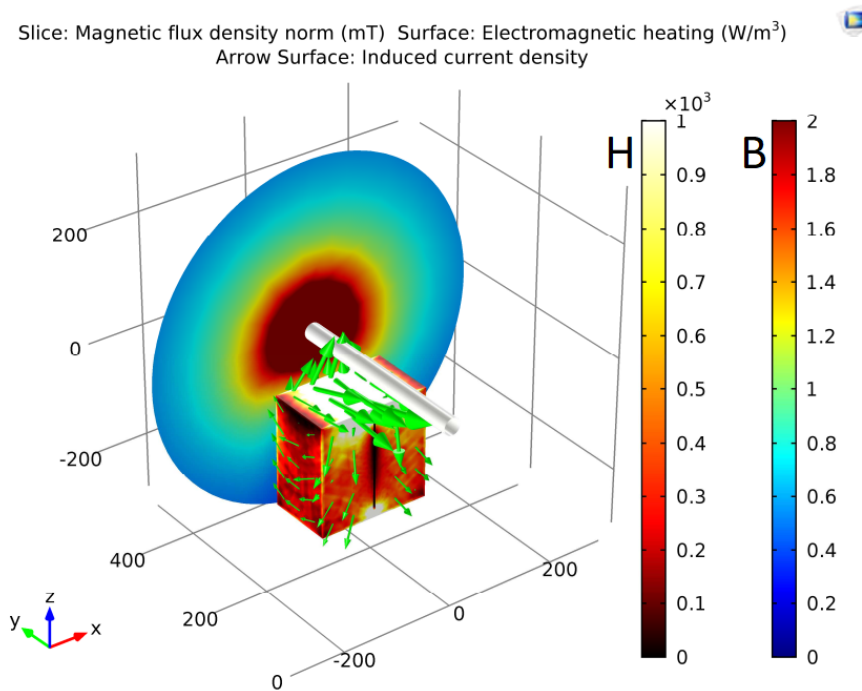
Figure 8.7: Vertical slot antenna in the xz plane. The electromagnetic heating increases at the lowest end of the slot
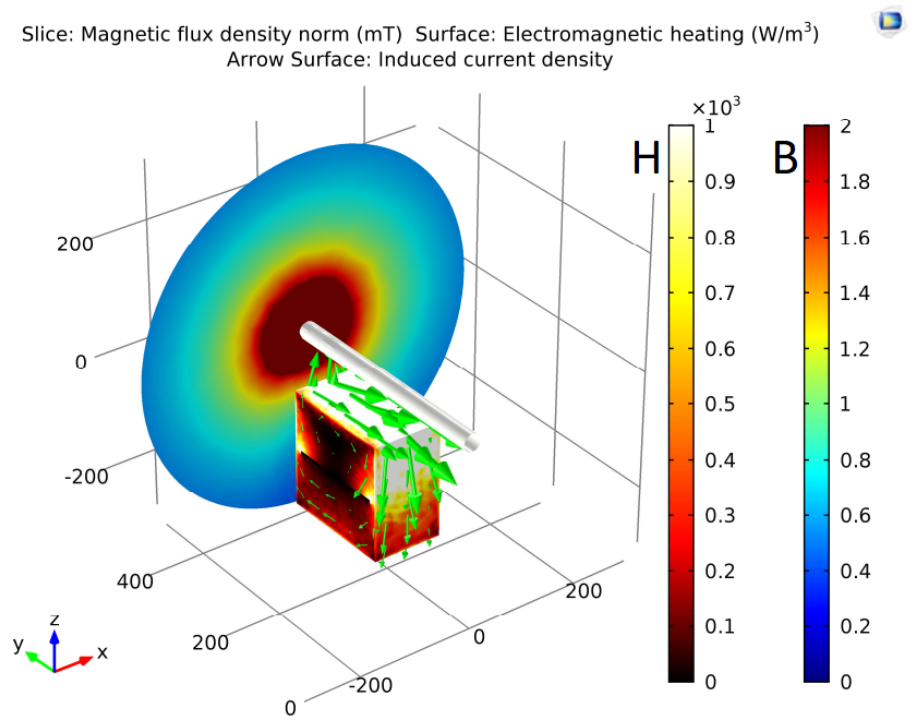
Figure 8.8: Horizontal slot antenna in the yz plane. The electromagnetic heating increases at both ends of the slot
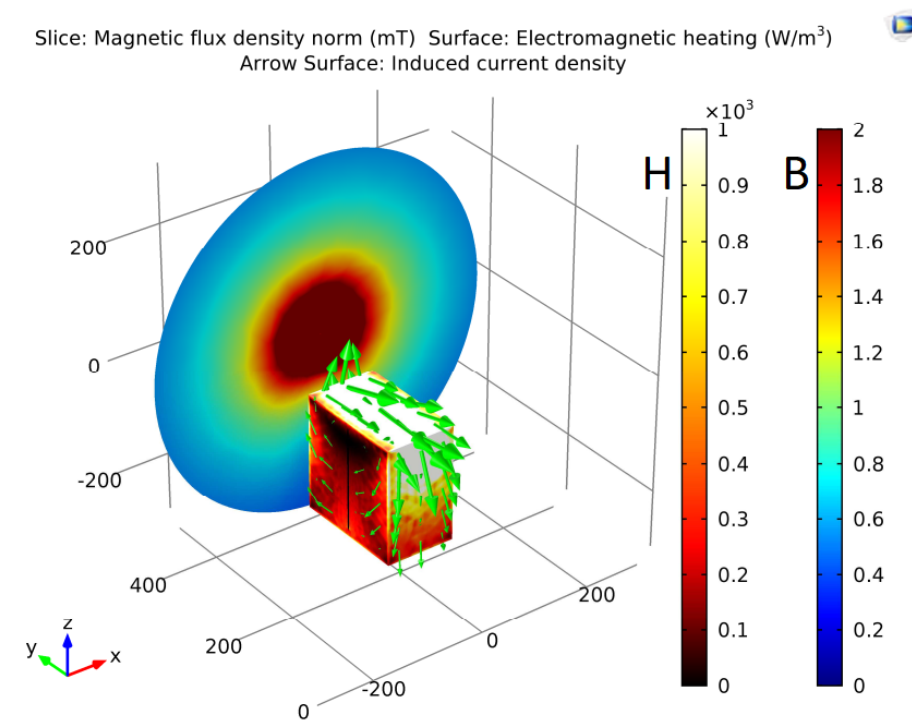
Figure 8.9: Vertical slot antenna in the yz plane. The electromagnetic heating increases at the lowest end of the slot

(a) xz plane horizontal

(b) xz plane vertical

(c) yz plane horizontal

(d) yz plane vertical
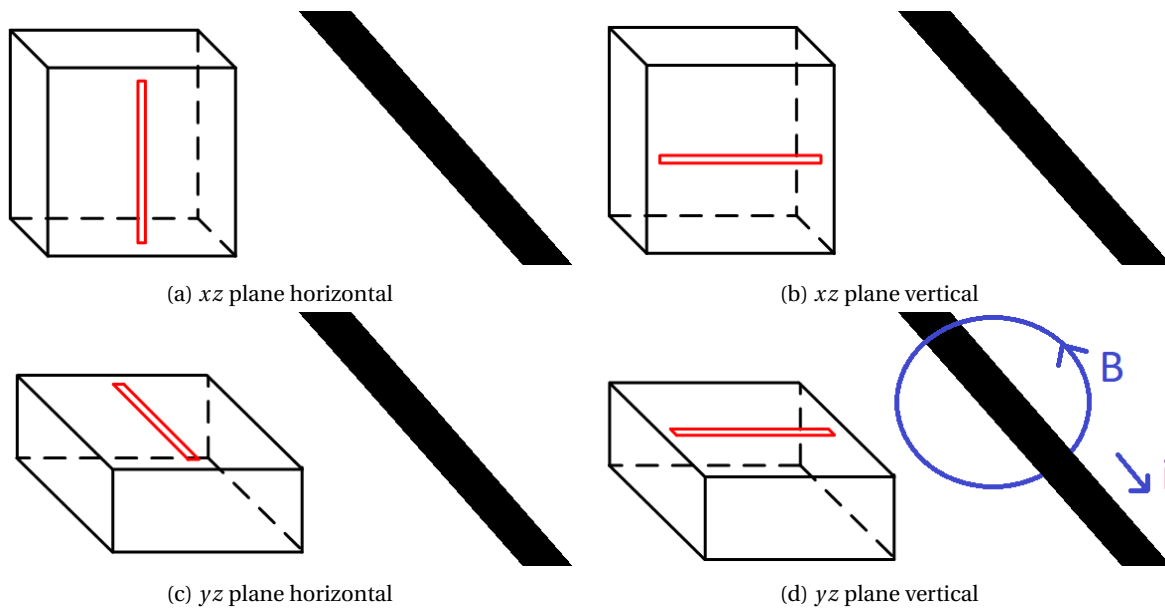
Figure 8.10: Positions of the slot (red) in respect to the conductor (black) in order to compare the simulations. In figure 8.10d one magnetic field lines is show in respect to a current direciton.
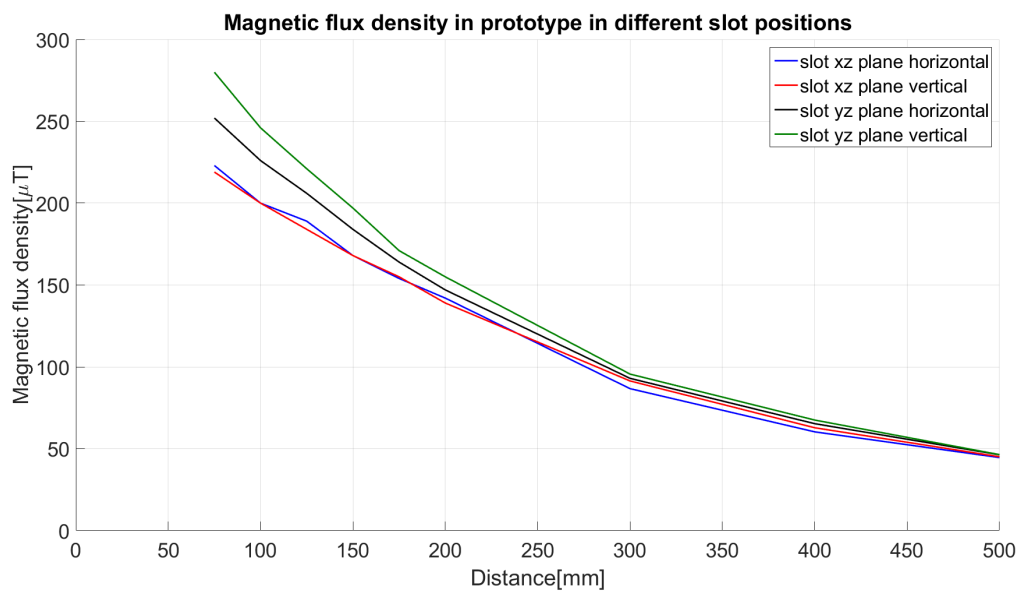
Figure 8.11: Magnetic flux density inside prototype with the slot positions as in the figures of 8.10. The current through the conductor is 800 A.

8.4. COMMUNICATION ANALYSIS

In chapter 7 the slot antenna was designed. The goal of this section is to analysis the antenna reflection coefficient and test its reliability. First the reflection coefficient from simulation is compared with the measured value for the prototype cover, complete prototype and stainless steel plate. Second the antenna is exposed corona discharges.

8.4.1. ANTENNA CHARACTERISTICS

The simulation of the antenna is based on a slot with a length of $0.5 \cdot \lambda$, width of $1/40 \cdot \lambda$ and a feed-in distance from the side of $1/8 \cdot \lambda$. The reflection coefficient is measured for the prototype in two parts: the cover which consist of the slot antenna and the prototype in its completeness. Furthermore an stainless steel plate is considered, which is directly related to the geometry of the simulation. The results are shown in figure 8.12 and are summarized in table 8.3.

The reflection coefficient from the cover of the prototype and the plate in comparison with the simulation result in a shift of resonance frequency. The shift can be explained by the feed-in location as was discussed in section 7.3. A smaller feed-in distant from the end of the slot decrease the resonance frequency. This was obtained from simulations were the distance had a difference of $\pm$ 10 mm. The measurements show a increase in resonance frequency while the feed-in distance is decreased. This contradict the theory. However the difference in distant is approximately 0.5 and 2.5 mm and includes a measuring error of 5 mm from a tapeline.

The reflection coefficient from the complete prototype and cover shows again a shift in frequency but also a strong difference in magnitude. The slot antenna radiates at two sides of the slot: to the front and back in the enclosure. In case of the complete prototype the electromagnetic wave is reflected inside the enclosure several times. Because the slot is the only hole the electromagnetic wave can leave the prototype the radiated power is increased but is shifted in resonance frequency.

	Simulation	Prototype cover	Prototype	Plate
Resonant Frequency	880.2 MHz	989.7 MHz	1054.9 MHz	949.7 MHz
Magnitude	-12.1 dB	-13.4 dB	-25.2 dB	-13.1 dB
Magnitude at 868 MHz	-12.1 dB	-4.2 dB	-3.3 dB	-8.4 dB

Table 8.3: Reflection coefficient from figure 8.12
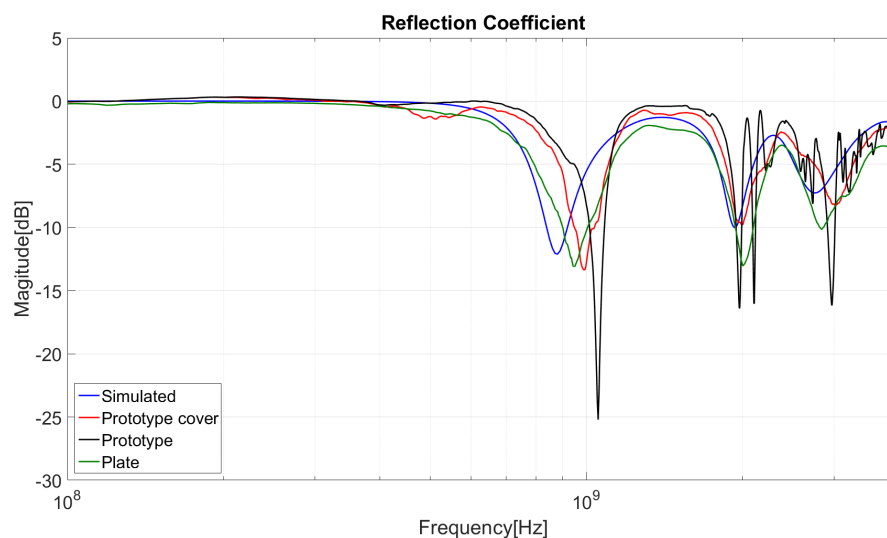
Figure 8.12: Reflection coefficients of the slot antenna in: simulation, prototype cover, prototype and stainless steel plate.

In table 8.3 the reflection coefficient of the antennas at 868 MHz is compared to the resonance frequency. The resonance frequency is not equal to 868 MHz and will therefore loss energy by reflection. In case of the prototype a coefficient of -3.3 dB is found at 868 MHz. This mean approximately half of the energy is transmitted by the antenna.

8.4.2. COMMUNICATION RELIABILITY UNDER TEST

The antenna transmits an electromagnetic wave. To interrupt the data the prototype and the plate are exposed to two tests. First by placing them 0.5 cm away from a conductor through which 800 A flows. Second by applying a potential to the surface.

However before these test the electronics of the prototype was tested with a dipole antenna at 3 cm distance from lightning and switching impulse source. These tests were determine if an external magnetic field can induce a destructive emf over the electronics. As result these test did not damage or destroy the PCB or any electronic component on it.

For the stainless steel plate the test with the high magnetic field did not result in any data lost. The plate was exposed to maximum of 48.5 kV. During the test at a potential of 22 kV the corona discharges could be heard. After losing 5 packages the potential was decreased to zero to test for permeate damage. Afterward the potential was increased to 48.5 kV and did not suffer packages lost.

The prototype did not lost any data during the high magnetic field test. For the second test the prototype was exposed to maximum of 132 kV. During the test the corona discharges were measured. Before the test a noise of 1.2 pC was measured. While increasing the potential a noise of approximately 25 pC was measured. When the potential reached 55 kV corona discharges could be heard. At 132 kV the magnitude of the discharges reached 180 pC. However no packages were lost during this test.

CONCLUSIONS AND RECOMMENDATIONS

Contents

In the previous chapter the results from simulations and measurements were discussed. The goal of this chapter is to summarize the conclusions, address the scientific contributions and provide the recommendations in the section 9.1, 9.2 and 9.3 respectively.

9.1. CONCLUSIONS

The main goal of this thesis was to examine if a Low Power Wide Area Network can function at 868 MHz in an overhead line environment for dynamic line rating applications. The main objective was to design a prototype as real-time monitoring system which can validate the reliability.

The parameters to determine static and dynamic line rating were determined. Static line rating is based on an ambient temperature of 30 °C, effective wind speed of 0.6 ms^{-1} and solar radiation of 1000 Wm^{-2}. Dynamic line rating use real-time ratings for which several monitoring devices were considered. Measuring the sag and conductor temperature directly provide information to monitor the critical spans.

The consequences of dynamic line rating affects the conductor temperature and the sag. Dynamic line rating allows a higher thermal current through the conductor. The heating gains and losses mechanism of the conductor were considered. Furthermore a method to determine the increase of sag in case of a higher conductor temperature and concentrated weight was examine. A temperature increase of 5 °C increases the sag, of a span of 500 m, by 31 cm, while installing a real-time monitoring system on the overhead line with a weight of 5 kg result in an increase of sag by 24 cm. Both increase in sag are negligible.

A method to reduce a low frequency magnetic field was determined. Two methods were examine to reduce the electric and magnetic field inside a volume. Materials with a relative permeability higher than 1 provide a low reluctance path which absorbs the magnetic field lines for low frequencies. The method also describes the reflection phenomena of magnetic field for high frequencies. In order to reduce a magnetic field, of 50 Hz 800 A at a distance 5 cm below an overhead line conductor inside a sphere with a radius 105 mm, to 10 μT a 1.25 mm mu-metal shield is required.

The performance of the prototype was evaluated on its thermal behavior, shielding effectiveness and communication reliability. To evaluate the thermal behavior the prototype was placed 0.5 cm from the conductor through which 800 A flowed. The thermal equilibrium for the conductor was reached after 150 minutes in which the conductor temperature increased 34.9 °C and the prototype surface 1.9 °C. The prototype can reduce a 50 Hz magnetic field at 5 cm distance from the conductor with a shielding effectiveness of 14.8 dB.

A basic design of a slot antenna is made. Several antennas were considered including the dipole and loop antenna. The slot antenna was designed and evaluate on its feed-in location and width of the slot. This antenna was placed on the prototype. The position of the slot has to be placed carefully in respect to the conductor in order to allow the path of the induced to continue. Therefore electromagnetic heating will be minimized. The reflection coefficient of the antenna at 868 MHz is -3.3 dB. Each package of data was received

in case the prototype was at 0.5 cm distance from a conductor through which a 800 A current flow. Furthermore also in case of corona discharges which occurred up to 132 kV.

Therefore it can be concluded that the prototype demonstrated the reliability of communication at 868 MHz. Furthermore the theory of low frequency magnetic shielding is demonstrated.

9.2. CONTRIBUTIONS

In scientific contributions of this thesis are summarized by the following aspects.

A method was derived to reduce a low frequency magnetic field inside a volume. In this thesis the method was used examine the magnetic field of 50 Hz inside a steel rectangular box. The method can also be used for another frequency, material and geometry.

An slot antenna was designed in a metallic plate. In this thesis the resonance frequency was 868 MHz. However the design was set in respect to the wavelength of the frequency. Therefore a slot antenna for another resonance frequency can be made with the design of this thesis.

The reliability of communication at 868 MHz for Low Power Wide Area Network was tested under comparable electric environment of an overhead line. The prototype and stainless steel plate was placed 5 cm away from a conductor through which 800 A flows and were exposed to a potential of 132 kV and 44 kV respectively. Under these conditions the communication reliability was shown. Under other and stronger electric environments can be done to test the reliability.

9.3. RECOMMENDATIONS

The scope and results of this thesis allows research for further studies. The recommendation to these studies are given.

The maximum magnetic flux density requires thorough evaluation. The maximum was set to 10 μT inside the prototype is not required to ensure the safety of the electronics. During the thesis several tests were performed in order to determine the maximum magnetic flux density. The electronics with a dipole antenna, without any shielding, was placed up to 3 cm away from several lightning and switching impulses. It was expected that the magnetic field from the impulse would induced a emf and damage the electronics. However this did not occurs. More researched is required to determine maximum magnetic flux density in combination in respect to the rate of change in time to damage the electronics.

Optimization of the slot antenna requires more testing. The length of the slot antenna was fixed at $0.5 \cdot \lambda$ in order to appropriate the circumference of the slot to a single λ. However measurements of the antenna characteristics resulted in a shift of resonance frequency. By the use of conductive tape the length of the slot antenna can be decreased. However the ratio of the short and long path across the slot will change. With this in mind the slot antenna can be optimized and reduces the energy losses.

Mechanical clamp, energy harvesting and sensors has to be designed and analyzed. In order to apply dynamic line rating at overhead lines the prototype requires several more aspects. Installing a real-time monitoring device at an overhead line brings the device in contact with the line. Therefore the heat transfer has to be reconsidered. An energy harvesting device introduces new challenges in energy storage and protection. The required energy harvesting will depend on the current through the conductor. Last the sensors to apply dynamic line rating has to be installed at the monitoring device. Accuracy and reliability of the sensors need to be considered.

BIBLIOGRAPHY

[1] Greenpeace, *Factsheet kolenexit in nederland,* http://www.greenpeace.nl/2017/Nieuwsberichten/Klimaat--Energie/Factsheet-Kolenexit-in-Nederland/ (2017 June).

[2] Sociaal-Economische Raad(SER), *Energie-akkoord voor duurzame groei,* http://www.energieakkoordser.nl/energieakkoord.aspx (2013 October), accessed: 2017-07-19.

[3] TenneT, *Net op zee borsesele,* http://www.tennet.eu/.../net-op-zee-borssele/ (2017), accessed: 2017-08-02.

[4] Cigre Task Force B2.12, *Guidelines for increased utilization of existing overhead transmission lines,* (2008 August).

[5] ENTSOE, *Dynamic line rating for overhead lines v6,* **6** (2015 March).

[6] Cigre Task Force B2.12.3, *Sag-tension calculation methods for overhead lines,* (2007 June).

[7] Cigre Working Group B2.12, *Guide for selection of weather parameters for bare overhead conductor ratings,* (2006 August).

[8] *Koninklijk Nederlandse Meteorlogisch Instituut (KNMI),* http://knmi.nl/nederland-nu/weer/waarnemingen (2017), accessed: 2017-09-18.

[9] E. Fernandez, , *Review of dynamic line rating systems for wind power integration,* (2015 September).

[10] EDM, *Span sentry,* http://edmlink.com/span-sentry (2017), accessed: 2017-07-18.

[11] Ampacimon, *Overhead line monitoring,* http://Ampacimom.com/datasheet-ampacimon.pdf (2003), accessed: 2016-12-16.

[12] Cigre Working Group B2.43, *Guide for thermal rating calculations of overhead lines,* (2014).

[13] IEEE Standard 738 , *Standard for calculating the current-temperature relationship of base overhead conductors,* (2012 October), pp. 7-10.

[14] F. Kiessling, P. Nefzger, J.F. Nolasco, U. Kaintzyk, *Overhead power lines,* (2002 October), pp. 540 - 551.

[15] P.A. Tipler, G. Mosca , *Physics for scientists and engineers,* **6** (2008), pp. 750 -751.

[16] P. Schavemaker and L. van der Sluis, *Electrical power system essentials,* (2009 February).

[17] C.R. Paul, *Electromagnetic compatibility,* **2** (2006).

[18] H. Zumbahlen , *Linear circuit design handbook,* (2008).

[19] A.C. Cortes, *Sistemas de comunicacion ii,* (2016 February), pp. 410-443.

[20] S. Radu, *Engineering aspects for electromagnetic schielding,* (2009 March).

[21] P.C.T. van der Laan, W.J.L Jansen, E.F. Steennis , *The design of shielded enclosures especially for high-voltage laboratories,* (1984), pp. 100-111.

[22] S. Hughes, *The electrostatic uniqueness theorem,* (2005 February), pp. 47 -50.

[23] S. Celozzi, R. Araneo, G. Lovat, *Electromagnetic shielding,* (2008), pp. 263 - 281.

[24] W. Greiner , *Quasi-stationary currents and current circuits,* (1998), pp. 276-277.

[25] H. Kaden , *Wirbelstrome und schirmung in der nachrichtentechnik,* **2** (1959), pp. 269 - 311.

[26] S. Campione, *Shielding effectiveness of multiple-shield cables with arbitrary terminations via transmission line analysis,* **65** (2016 March).

[27] Mu-Metal, *Technical data,* (2015).

[28] D.M. Pozar, *Microwave engineering,* **4** (2012), pp. 110 - 113.

[29] W.E. Pakala, V.L. Chartier, *Radio noise measurements on overhead power lines from 2.4 to 800 kv,* **PAS-90, Issue: 3** (1971 May), pp. 1155-1164.

[30] F.H. Kreuger, *Industrial high voltage volume ii,* (1992).

[31] B. Schweber, *Understanding antenna specifications and operation i,* https://www.digikey.com/ (2017 April).

[32] Unknown, *Loop antennas,* (2003 December), accessed: 2017-10-31.

[33] J.J. Carr, *Practical antenna handbook,* **4** (2001), pp. 319 - 324.

[34] P. J. Bevelacqua , *Loop antennas,* http://www.antenna-theory.com/antennas (2011).

[35] U.A.Bakshi, *Antenna and wave propagation,* (2009), pp. 66 - 68.

[36] P. De Vita, *Antenna selection guideliness,* (2012 November).

[37] Thermoucoupleinfo, *Thermocouple accuracies,* Accessed: 2017-06-28.

[38] Livingston Test Equipment, *Electric and magnetic field analyzer ehp-50a,* Accessed: 2017-07-03.

[39] Prysmian Group, *Power cables, aluminium conductor steel reinforced,* (2015 May).

[40] P.R. Clayton, *Inductance : loop and partial,* (2010), pp. 126 -130.

A

TEST SETUP

In order to validate the theory a test setup was build with a conductor through which a current can flow. For the test a high current is required to obtain a high magnetic field. Therefore two geometries are tested to decrease the inductance of the loop in section A.1. Furthermore a compensation capacitor is determined to increase the maximum current even more.

The used conductor consist of 7 steel wires in the center and a total of 48 aluminum wires build up in three outer layers (ACSR). Furthermore the diameter of the conductor is approximately $3.5cm$ and $12.9m$ long. Unfortunately the maximum current rating is unknown. However by comparing the construction data from other ACSR conductors the current rating in air can be approximated with [39] as 1000A.

A.1. INDUCTANCE

Decreasing the inductance of a overhead line result in less reactance and improve the power transfer []. The inductance depends on the loop geometry, diameter and wire diameter [40]. Two different geometries are tested to have the lowest inductance: o-shape and 8-shape loop as can be seen in figure A.1. The o-shape loop is assumed to be a circle with a radius of $12.9/(2\pi) = 2.05m$. the 8-shape loop is assumed to consist of two helices. The conductor has a fixed length. Therefore the radius of the helices will be smaller than the o-shape. The radius of the helices is $12.9/(2 \cdot 2\pi) = 1.02m$. The inductance for a circle can be calculated by equation A.1 [40]. The inductance of the 8-shape loop can be seen as two inductor in serie.

$$L \approx \mu_0 \cdot a \cdot \left(ln(\frac{8 \cdot a}{r_c}) - 2 \right) \tag{A.1}$$

Here a is the radius of the loop and r_c the radius of the conductor. The result of the calculated, simulated and measured inductance can be seen in table A.1. In the measurement the loops where placed $40cm$ above the ground. To simulate the magnetic flux density for the o- and 8-shape loop a current source of $800A$ is connected to one side of terminal while the other side is grounded. Figure A.2 shows the magnetic flux density lines in mT.

	Calculated	Simulated	Measurement
o-shape	12.50 μ H	11.10 μ H	11.3 μ H
8-shape	10.71 μ H	10.75 μ H	11.3 μ H

Table A.1: Comparison of the inductance calculated, simulated and measured for the o-shape and 8-shape loop
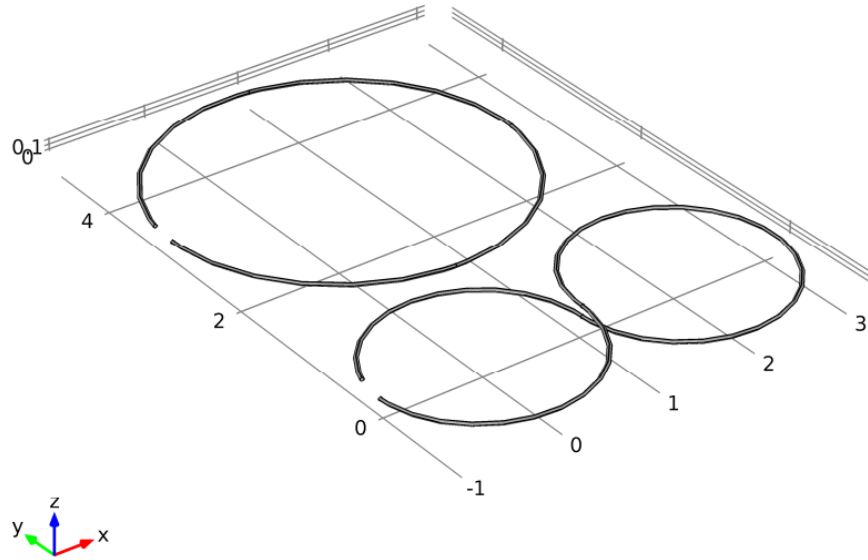
Figure A.1: The two loop geometries to be simulated and tested. Left o-shape loop. Right 8-shape loop where the conductor crosses in the middle of the loop with some distance
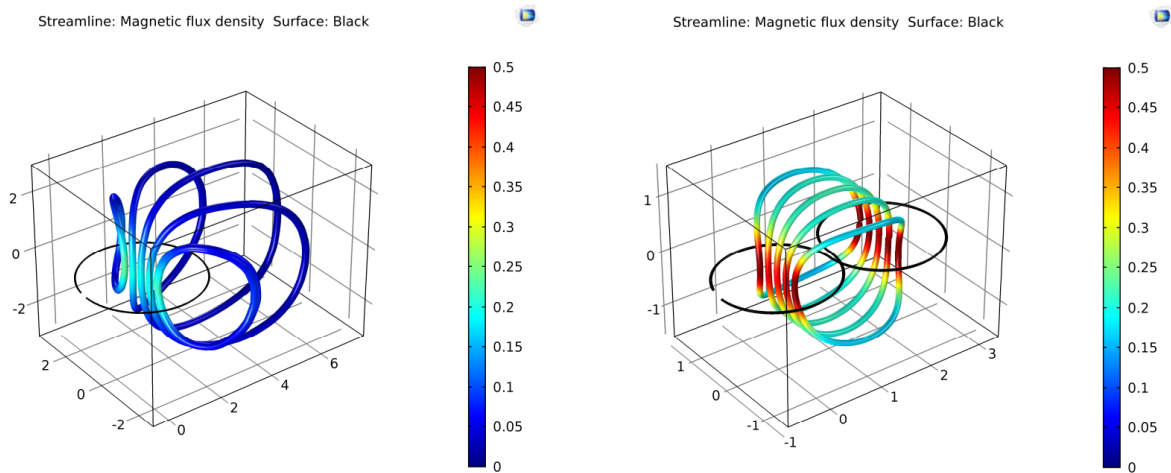

Figure A.2: The magnetic flux lines around the o-shape and 8-shape conductor

A.1.1. OBSERVATIONS

The simulation and measurement of the inductance of the 0-shape and 8-shape result in approximately equal values. The small difference can be the result of the location where the loops where placed. The floor in the High Voltage Laboratory is conductive. Therefore several heights above the ground were tested. The result are shown in table A.2. For low frequency the magnetic field lines are absorbed into the floor which effects the amount of magnetic flux through the loop.

Another observation follows from simulation result in the figures of A.2. The magnetic flux density has a higher value in the centers 8-shape loop then in the o-shape. This was expected due to the the smaller radius of the helices and the change in current direction due to the crossing point in the middle.

	Ground	5.5cm	40cm
o-shape	$7.4\,\mu\mathrm{H}$	$8.6\,\mu\mathrm{H}$	$11.3\mu\mathrm{H}$
8-shape	$8.1\,\mu\mathrm{H}$	$9.3\,\mu\mathrm{H}$	$11.3\,\mu\mathrm{H}$

Table A.2: Inductance o-shape and 8-shape loop at different heights

A.2. NO COMPENSATION

To determine the current through the loop equipment is added to the test setup. At the supply side a step-down transformer is used in combination with multimeter with a current clamp to measure the supply voltage V_s, current I_s and power factor $pf(\cos(\theta))$. To measure the current through the loop I_l a current transformer with a ration $5000:5$ is used. First the mentioned values are measured when no compensation capacitor is connected. The result of the o-shape and 8-shape loop can be seen in table A.3 and A.4 respectively.

V_s	I_s	I_l	pf
60.4V	10.3A	356A	0.254
63.5V	10.8A	370A	0.251

Figure A.3: o-shape loop measurement results without compensation

V_s	I_s	I_l	pf
60.5V	10.1A	393A	0.237
64.9V	11.5A	423A	0.236

Figure A.4: 8-shape loop measurement results without compensation

A.3. COMPENSATION

In order to maximize the current through the loop the lagging power factor has to be improved. A lagging power factor results from an inductive load and has a large positive reactance power. To compensate a capacitor is added to reduce the reactance power as shown in figure A.5. To determine the required capacitance first the lagging reactance is determined in equation A.2 and the capacitance to fully compensate is determined in equation A.3.
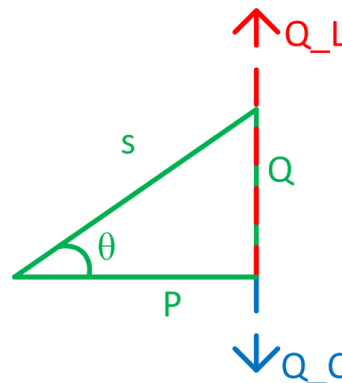

Figure A.5: The lagging power factor(θ) follows from the reactance due to the inductive load (red). In order to compensate a capacitor has to be added to lower the reactance (blue).

$$Q = V_s \cdot I_s \cdot \sin[\theta] \tag{A.2}$$

$$C = \frac{Q}{V_s^2 \cdot 2\pi \cdot f} \tag{A.3}$$

The required capacitance is in the case of o-shape loop approximately $525\mu F$ and for the 8-shape around $516\mu F$. However for practical reasons a capacitance of 231 μF, $462\mu F$ and $693\mu F$ is tested. The following results are obtained for the o-shape and 8-shape in tables A.6 and A.7 respectively. The supply voltage has been increased to approximately 100V each time.

C	V_s	I_s	I_l
231 μ F	100V	8A	590A
462 μ F	100V	4.7A	593A
693 μ F	100V	7A	600A

Figure A.6: o-shape loop measurement results with compensation

C	V_s	I_s	I_l
231 μ F	100.4V	9.8A	625A
462 μ F	100.6V	4.5A	655A
693 μ F	100.4V	6.5 A	654A

Figure A.7: 8-shape loop measurement results with compensation

From these measurements the 462μ F compensation result in the best result: the supply draws the least current for a high loop current. Furthermore it can be concluded that the 8-shape loop result in a higher loop current, which can be related to a lower inductance. The tested o-shape and 8-shape loop can seen in figure A.8 and A.9 respectively.
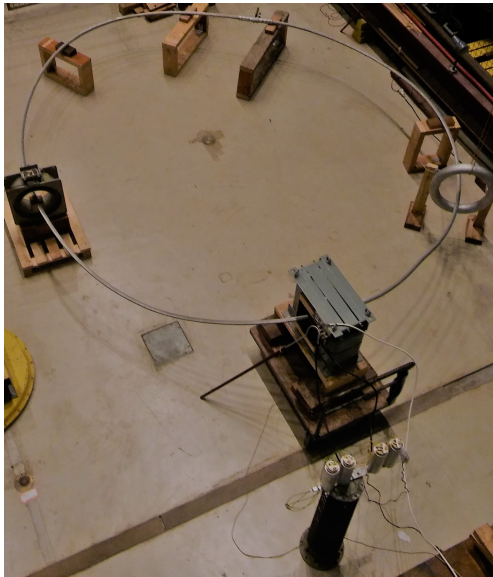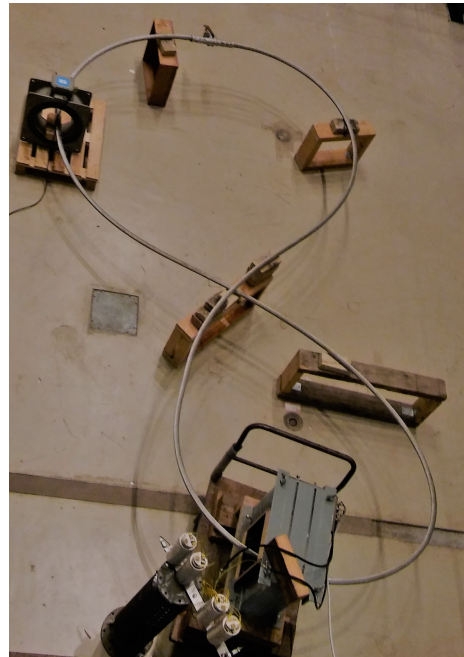

Figure A.8: The test setup with o-shape loop

Figure A.9: The test setup with 8-shape loop

B

DERIVATION OF EQUATIONS

B.1. SOLUTION SAGGING CURVE

First equation 4.6 is rearranged by moving the square root to the left and splitting the second derivative. Second the integration to dy is added and spitted into $\frac{dy}{dx} \cdot dx$ in equation B.1.

$$\frac{d}{dx} \cdot \frac{dy}{dx} \cdot \frac{1}{\sqrt{1 + \left(\frac{dy}{dx}\right)^2}} \cdot \frac{dy}{dx} \cdot dx = \frac{m_{cg}}{H} \cdot \frac{dy}{dx} \cdot dx \tag{B.1}$$

The right side of equation B.1 can be solved immediately:

$$\frac{m_c \cdot g}{H} \int dy = \frac{m_c \cdot g}{H} \cdot y \tag{B.2}$$

The left side of equation B.2 requires a substitution of $u = \frac{dy}{dx}$ to solve:

$$\frac{d}{dx} \cdot u \cdot \frac{1}{\sqrt{1 + u^2}} \cdot u \cdot dx = \int \frac{u}{\sqrt{1 + u^2}} du = \sqrt{1 + u^2} \tag{B.3}$$

Combing equations B.1 and B.3 and replacing the substitution with the original the following equation is obtained.

$$\sqrt{1 + \left(\frac{dy}{dx}\right)^2} = \frac{m_{cg}}{H} \cdot y \tag{B.4}$$

Equation B.4 can be solved to obtain $\frac{dy}{dx}$:

$$\frac{dy}{dx} = \sqrt{\left(\frac{m_c \cdot g}{H} \cdot y\right)^2 - 1} \tag{B.5}$$

The first order equation B.5 needs another substitution to further solve the sagging curve. The substitution $v = \frac{m_c \cdot g}{H} \cdot y$ used and the derivative is separated.

$$\frac{dy}{dv} \cdot \frac{dv}{dx} = \sqrt{v^2 - 1}$$
$$\frac{H}{m_c \cdot g} \cdot \frac{dv}{dx} = \sqrt{v^2 - 1} \tag{B.6}$$

By rearranging equation B.6 two integrals remain to be solved:

$$\int \frac{1}{\sqrt{v^2 - 1}} dv = \frac{m_c \cdot g}{H} \int \cdot dx$$
$$cosh^{-1} v = \frac{m_c \cdot g}{H} \cdot x \tag{B.7}$$

The left side represent the reverse of the hyperbolic cosine and can be solved for y by replacing the substitution with the original in equation B.7 the sagging curve is obtained:

$$y = \frac{H}{m_c \cdot g} \cdot cosh\left(\frac{m_c \cdot g}{H} \cdot x\right) \tag{B.8}$$

B.2. IMPEDANCE METHOD

In this appendix the exact solution will be derived from the boundary conditions of equation 6.4 again. First the wave E_1 has been shifted to the other side in the equations of B.9.

$$E_1 = E_i + E_r - E_2 \tag{B.9a}$$

$$\frac{E_1}{\eta_2} = \frac{E_i}{\eta_0} - \frac{E_r}{\eta_0} + \frac{E_2}{\eta_2} \tag{B.9b}$$

$$E_1 \cdot e^{-\gamma_2 t} = E_t \cdot e^{-\gamma_3 t} - E_2 \cdot e^{\gamma_2 t} \tag{B.9c}$$

$$\frac{E_1}{\eta_2} \cdot e^{-\gamma_2 t} = \frac{E_t}{\eta_0} \cdot e^{-\gamma_3 t} + \frac{E_2}{\eta_2} \cdot e^{\gamma_2 t} \tag{B.9d}$$

Substituting E_1 of equation B.9a in B.9b and equation B.9c in B.9d result in the two equation B.10 and B.11 in which E_2 can be shifted to the other side of the equal sign.

$$-2E_2 = E_i \cdot \left(\frac{\eta_2 - \eta_0}{\eta_0}\right) + E_r \cdot \left(\frac{-\eta_2 - \eta_0}{\eta_0}\right) \tag{B.10}$$

$$-2E_2 = -E_t \cdot e^{j\beta_0 t} \cdot e^{-\gamma_2 t} \cdot \left(\frac{-\eta_2 + \eta_0}{\eta_0}\right) \tag{B.11}$$

Next in these equations E_2 can be substituting together. This result in a single expression in equation B.12.

$$E_r = E_i \cdot \left(\frac{-\eta_0 + \eta_2}{\eta_0 + \eta_2}\right) + E_t \cdot e^{-j\beta_0 t} \cdot e^{-\gamma_2 t} \cdot \left(\frac{\eta_0 - \eta_2}{\eta_0 + \eta_2}\right) \tag{B.12}$$

Now these steps can be done again by first shifting and substituting E_2 and then substituting E_1. This result in equation B.13.

$$E_r = E_i \cdot \left(\frac{-\eta_0 - \eta_2}{\eta_0 - \eta_2}\right) + E_t \cdot e^{-j\beta_0 t} \cdot e^{\gamma_2 t} \cdot \left(\frac{-\eta_0 - \eta_2}{\eta_0 - \eta_2}\right) \tag{B.13}$$

Substituting E_r in equation B.12 and B.13 result in an expression with only E_i and E_t in B.14.

$$E_i \cdot \left[\frac{-\eta_0 - \eta_2}{\eta_0 - \eta_2} - \frac{-\eta_0 + \eta_2}{\eta_0 + \eta_2}\right] = E_t \cdot e^{-j\beta_0 t} \cdot \left[e^{-\gamma_2 t}\frac{\eta_0 - \eta_2}{\eta_0 + \eta_2} - e^{\gamma_2 t}\frac{-\eta_0 - \eta_2}{\eta_0 - \eta_2}\right] \tag{B.14}$$

$$E_i \cdot \left[\frac{-4\eta_0\eta_2}{(\eta_0 - \eta_2)(\eta_0 + \eta_2)}\right] = E_t \cdot e^{-j\beta_0 t} \cdot e^{\gamma_2 t} \cdot \left[e^{-2\gamma_2 t}\frac{\eta_0 - \eta_2}{\eta_0 + \eta_2} + \frac{\eta_0 + \eta_2}{\eta_0 - \eta_2}\right] \tag{B.15}$$

$$\frac{E_i}{E_t} \cdot \left[\frac{-4\eta_0\eta_2}{(\eta_0 + \eta_2)^2}\right] = e^{-j\beta_0 t} \cdot e^{\gamma_2 t} \cdot \left[e^{-2\gamma_2 t}\left(\frac{\eta_0 - \eta_2}{\eta_0 + \eta_2}\right)^2 + 1\right] \tag{B.16}$$

Furthermore when this equation is reorganized the result in section 6.1 is obtained in equation B.17.

$$\frac{\mathbf{E}_i}{\mathbf{E}_t} = \frac{(\eta_0 + \eta_2)^2}{4\eta_0\eta_2} \cdot e^{\frac{t}{\delta}} e^{j\beta t} e^{-j\beta_0 t} \cdot \left[1 - \left(\frac{\eta_0 - \eta_2}{\eta_0 + \eta_2}\right)^2 e^{\frac{-2t}{\delta}} e^{\frac{-j2t}{\delta}}\right] \tag{B.17}$$

B.3. Basic equations

To derive the shielding effectiveness from the founded Q-factor multiple mathematical expressions are needed. Here the equations which are required are sumed up here.

$$|\underbrace{(a_1 + a_2)}_{\text{real}} + i \cdot \underbrace{(b_1 + b_2)}_{\text{imaginary}}|^2 = (a_1 + a_2)^2 + (b_1 + b_2)^2 = a_1^2 + 2a_1 a_2 + a_2^2 + b_1^2 + 2b_1 b_2 + b_2^2 \tag{B.18}$$

where real is the $(a_1 + a_2)$ term, imaginary is the $(b_1 + b_2)$ term, and the bracketed expression is a complex number.

$$e^{x+iy} = e^x e^{i \cdot y} = \overbrace{\underbrace{(e^x cos(y))}_{\text{real}} + i \cdot \underbrace{(e^x sin(y))}_{\text{imaginary}}}^{\text{complex number}} \tag{B.19}$$

$$|e^{x+iy}| = \sqrt{(e^x cos(y))^2 + (e^x sin(y))^2} = e^x \tag{B.20}$$

$$cosh(x+iy) = \frac{1}{2}(e^{x+iy} + e^{-(x+iy)}) = cos(y) \cdot cosh(x) + i \cdot sin(y) \cdot sinh(x) \tag{B.21}$$

$$sinh(x+iy) = \frac{1}{2}(e^{x+iy} - e^{-(x+iy)}) = cos(y) \cdot sinh(x) - i \cdot sin(y) \cdot cosh(x)$$

The product rules for trigonometric and hyperbolic functions are shown in B.21 and in B.23 in case of the same argument.

$$cos(A) \cdot cos(B) = \frac{1}{2}[cos(A-B) + cos(A+B)] \quad cosh(A) \cdot cosh(B) = \frac{1}{2}[cosh(A+B) + cosh(A-B)] \tag{B.22}$$

$$sin(A) \cdot sin(B) = \frac{1}{2}[cos(A-B) - cos(A+B)] \quad sinh(A) \cdot sinh(B) = \frac{1}{2}[cosh(A+B) - cosh(A-B)]$$

$$sin(A) \cdot cos(B) = \frac{1}{2}[sin(A-B) + sin(A+B)] \quad sinh(A) \cdot cosh(B) = \frac{1}{2}[sinh(A+B) + sinh(A-B)]$$

$$cos(A) \cdot cos(A) = \frac{1}{2}[1 + cos(2A)] \quad cosh(A) \cdot cosh(A) = \frac{1}{2}[cosh(2A) + 1] \tag{B.23}$$

$$sin(A) \cdot sin(A) = \frac{1}{2}[1 - cos(2A)] \quad sinh(A) \cdot sinh(A) = \frac{1}{2}[cosh(2A) - 1]$$

$$sin(A) \cdot cos(A) = \frac{1}{2}sin(2A) \quad sinh(A) \cdot cosh(A) = \frac{1}{2}sinh(2A)$$

B.4. SHIELDING EQUATIONS IN SHORT

To determine the shielding effectiveness for the separation of variables method the shielding factor of equation B.24 is solved by applying eqation B.25.

$$Q = \frac{1}{cosh(kd) + \frac{1}{3}(K + \frac{2}{K})sinh(kd)} \tag{B.24}$$

$$SE = ln\frac{1}{|Q|} \tag{B.25}$$

The solution is obtained in equation B.26. Here K, k and R are defined in B.27

$$\begin{aligned} SE = \frac{1}{2}ln[\frac{1}{9}[(R)^2 + (\frac{1}{R})^2](cosh\frac{2d}{\delta} - cos\frac{2d}{\delta}) \\ + \frac{1}{3}R(sinh\frac{2d}{\delta} - sin\frac{2d}{\delta}) + \frac{1}{3R}(sinh\frac{2d}{\delta} + sin\frac{2d}{\delta}) \\ + \frac{1}{2}cosh\frac{2d}{\delta} + cos\frac{2d}{\delta})] \end{aligned} \tag{B.26}$$

$$K = \frac{\mu_r k}{r_0} \quad k = \frac{(1+j)}{\delta} \quad R = \frac{\mu_r k}{r_0 \delta} \tag{B.27}$$

B.5. SHIELDING EQUATION DERIVATION

First the shielding factor is divided in equation B.28

$$\frac{1}{Q} = cosh(kd) + \frac{1}{3}(K + \frac{2}{K}) \cdot sinh(kd) \tag{B.28}$$

$$= cosh(kd) + \frac{1}{3}[R(1+i) + \frac{2}{R(1+i)}] \cdot sinh(kd) \tag{B.29}$$

$$= cosh(\frac{d}{\delta}(1+i)) + \frac{1}{3}\left[R(1+i) + \frac{(1-i)}{R}\right] \cdot sinh(\frac{d}{\delta}(1+i)) \tag{B.30}$$

Equation B.30 consist of 5 parts(when seperating the real and imaginary parts). With the basic equations of the previous section these parts can be seperated with equation B.21.

$$cosh(\frac{d}{\delta}(1+i)) = cos\frac{d}{\delta} \cdot cosh\frac{d}{\delta} + i \cdot sin\frac{d}{\delta} \cdot sinh\frac{d}{\delta} \tag{B.31}$$

$$\frac{1}{3}R \cdot sinh(\frac{d}{\delta}(1+i)) = \frac{1}{3}R(cos\frac{d}{\delta} \cdot sinh\frac{d}{\delta} + i \cdot sin\frac{d}{\delta} \cdot cosh\frac{d}{\delta}) \tag{B.32}$$

$$\frac{1}{3}Ri \cdot sinh(\frac{d}{\delta}(1+i)) = \frac{1}{3}R(-sin\frac{d}{\delta} \cdot cosh\frac{d}{\delta} + i \cdot cos\frac{d}{\delta} \cdot sinh\frac{d}{\delta}) \tag{B.33}$$

$$\frac{1}{3}\frac{1}{R} \cdot sinh(\frac{d}{\delta}(1+i)) = \frac{1}{3}\frac{1}{R}(cos\frac{d}{\delta} \cdot sinh\frac{d}{\delta} + i \cdot sin\frac{d}{\delta} \cdot cosh\frac{d}{\delta}) \tag{B.34}$$

$$-\frac{1}{3}\frac{1}{R}i \cdot sinh(\frac{d}{\delta}(1+i)) = \frac{1}{3}\frac{1}{R}(sin\frac{d}{\delta} \cdot cosh\frac{d}{\delta} - i \cdot cos\frac{d}{\delta} \cdot sinh\frac{d}{\delta}) \tag{B.35}$$

Reordering the real and imaginary part of the complete sum of equation B.31.

$$cos\frac{d}{\delta} \cdot cosh\frac{d}{\delta} + \frac{1}{3}(R + \frac{1}{R}) \cdot cos\frac{d}{\delta} \cdot sinh\frac{d}{\delta} - \frac{1}{3}(R - \frac{1}{R}) \cdot sin\frac{d}{\delta} \cdot cosh\frac{d}{\delta} \tag{B.36}$$

$$+i[sin\frac{d}{\delta} \cdot sinh\frac{d}{\delta} + \frac{1}{3}(R + \frac{1}{R}) \cdot sin\frac{d}{\delta} \cdot cosh\frac{d}{\delta} + \frac{1}{3}(R - \frac{1}{R}) \cdot cos\frac{d}{\delta} \cdot sinh\frac{d}{\delta}] \tag{B.37}$$

$$a + Zb - Yc + i(d + Zc + Yb) \tag{B.38}$$

By taking the absolute value like in equation B.18 a total twelve equation has to be summed up.

$$\sqrt{a^2 + d^2 + (Zb)^2 + (Zc)^2 + (Yb)^2 + (Yc)^2 + 2Zab - 2Yac - 2YZbc + 2Zcd + 2Ydb + 2YZbc} \tag{B.39}$$

$$a^2 = (cos\frac{d}{\delta} \cdot cosh\frac{d}{\delta})^2 = \frac{1}{2}(1 + cos\frac{2d}{\delta}) \cdot \frac{1}{2}(cosh\frac{2d}{\delta} + 1) = \frac{1}{4}(1 + cosh\frac{2d}{\delta} + cos\frac{2d}{\delta} + cosh\frac{2d}{\delta} \cdot cos\frac{2d}{\delta}) \tag{B.40}$$

$$d^2 = (sin\frac{d}{\delta} \cdot sinh\frac{d}{\delta})^2 = \frac{1}{2}(1 - cos\frac{2d}{\delta}) \cdot \frac{1}{2}(cosh\frac{2d}{\delta} - 1) = \frac{1}{4}(-1 + cosh\frac{2d}{\delta} + cos\frac{2d}{\delta} - cosh\frac{2d}{\delta} \cdot cos\frac{2d}{\delta}) \tag{B.41}$$

Combining equation B.40 and B.41 gives: $= \frac{1}{2}(cosh\frac{2d}{\delta} + cos\frac{2d}{\delta})$ (B.42)

$$(Zb)^2 = [\frac{1}{3}(R + \frac{1}{R}) \cdot cos\frac{d}{\delta} \cdot sinh\frac{d}{\delta}]^2 = \frac{1}{9}(R^2 + 2 + \frac{1}{R^2}) \cdot \frac{1}{2}(1 + cos\frac{2d}{\delta}) \cdot \frac{1}{2}(cosh\frac{2d}{\delta} - 1) \tag{B.43}$$

$$= \frac{1}{36}(R^2 + 2 + \frac{1}{R^2})(cosh\frac{2d}{\delta} - cos\frac{2d}{\delta} - 1 + cos\frac{2d}{\delta} \cdot cosh\frac{2d}{\delta})$$

$$(Zc)^2 = [\frac{1}{3}(R + \frac{1}{R}) \cdot sin\frac{d}{\delta} \cdot cosh\frac{d}{\delta}]^2 = \frac{1}{9}(R^2 + 2 + \frac{1}{R^2}) \cdot \frac{1}{2}(1 - cos\frac{2d}{\delta}) \cdot \frac{1}{2}(cosh\frac{2d}{\delta} + 1) \tag{B.44}$$

$$= \frac{1}{36}(R^2 + 2 + \frac{1}{R^2})(cosh\frac{2d}{\delta} - cos\frac{2d}{\delta} + 1 - cos\frac{2d}{\delta} \cdot cosh\frac{2d}{\delta})$$

Combining equation B.43 and B.44 gives:

$$\frac{1}{18}(R^2 + 2 + \frac{1}{R^2})(cosh\frac{2d}{\delta} - cos\frac{2d}{\delta}) \tag{B.45}$$

$$(Yb)^2 = [\frac{1}{3}(R - \frac{1}{R}) \cdot cos\frac{d}{\delta} \cdot sinh\frac{d}{\delta}]^2 = \frac{1}{9}(R^2 - 2 + \frac{1}{R^2}) \cdot \frac{1}{2}(1 + cos\frac{2d}{\delta}) \cdot \frac{1}{2}(cosh\frac{2d}{\delta} - 1) \tag{B.46}$$

$$= \frac{1}{36}(R^2 - 2 + \frac{1}{R^2})(cosh\frac{2d}{\delta} - cos\frac{2d}{\delta} - 1 + cos\frac{2d}{\delta} \cdot cosh\frac{2d}{\delta})$$

$$(Yc)^2 = [\frac{1}{3}(R - \frac{1}{R}) \cdot sin\frac{d}{\delta} \cdot cosh\frac{d}{\delta}]^2 = \frac{1}{9}(R^2 - 2 + \frac{1}{R^2}) \cdot \frac{1}{2}(1 - cos\frac{2d}{\delta}) \cdot \frac{1}{2}(cosh\frac{2d}{\delta} + 1) \tag{B.47}$$

$$= \frac{1}{36}(R^2 - 2 + \frac{1}{R^2})(cosh\frac{2d}{\delta} - cos\frac{2d}{\delta} + 1 - cos\frac{2d}{\delta} \cdot cosh\frac{2d}{\delta})$$

Combining equation B.46 and B.47 gives:

$$\frac{1}{18}(R^2 - 2 + \frac{1}{R^2})(cosh\frac{2d}{\delta} - cos\frac{2d}{\delta}) \tag{B.48}$$

Combining equation B.45 and B.48 gives:

$$\frac{1}{9}(R^2 + \frac{1}{R^2})(cosh\frac{2d}{\delta} - cos\frac{2d}{\delta}) \tag{B.49}$$

$$2Zab = \frac{2}{3}(R + \frac{1}{R}) \cdot cos\frac{d}{\delta} \cdot cosh\frac{d}{\delta} \cdot cos\frac{d}{\delta} \cdot sinh\frac{d}{\delta} = \frac{2}{3}(R + \frac{1}{R}) \cdot \frac{1}{2}(1 + cos\frac{2d}{\delta}) \cdot \frac{1}{2}sinh\frac{2d}{\delta} \tag{B.50}$$

$$= \frac{1}{6}(R + \frac{1}{R})(sinh\frac{2d}{\delta} + cos\frac{2d}{\delta} \cdot sinh\frac{2d}{\delta})$$

$$2Zcd = \frac{2}{3}(R + \frac{1}{R}) \cdot sin\frac{d}{\delta} \cdot cosh\frac{d}{\delta} \cdot sin\frac{d}{\delta} \cdot sinh\frac{d}{\delta} = \frac{2}{3}(R + \frac{1}{R}) \cdot \frac{1}{2}(1 - cos\frac{2d}{\delta}) \cdot \frac{1}{2}sinh\frac{2d}{\delta} \tag{B.51}$$

$$= \frac{1}{6}(R + \frac{1}{R})(sinh\frac{2d}{\delta} - cos\frac{2d}{\delta} \cdot sinh\frac{2d}{\delta})$$

Combining equation B.50 and B.51 gives:

$$\frac{1}{3}(R + \frac{1}{R})sinh\frac{2d}{\delta} \tag{B.52}$$

$$-2Yac = -\frac{2}{3}(R - \frac{1}{R}) \cdot cos\frac{d}{\delta} \cdot cosh\frac{d}{\delta} \cdot sin\frac{d}{\delta} \cdot cosh\frac{d}{\delta} = -\frac{2}{3}(R - \frac{1}{R}) \cdot \frac{1}{2}(cosh\frac{2d}{\delta} + 1) \cdot \frac{1}{2}sin\frac{2d}{\delta} \tag{B.53}$$

$$= \frac{1}{6}(R - \frac{1}{R})(-sin\frac{2d}{\delta} - sin\frac{2d}{\delta} \cdot cosh\frac{2d}{\delta})$$

$$2Ybd = \frac{2}{3}(R - \frac{1}{R}) \cdot sin\frac{d}{\delta} \cdot sinh\frac{d}{\delta} \cdot cos\frac{d}{\delta} \cdot sinh\frac{d}{\delta} = \frac{2}{3}(R - \frac{1}{R}) \cdot \frac{1}{2}(cosh\frac{2d}{\delta} - 1) \cdot \frac{1}{2}sin\frac{2d}{\delta} \tag{B.54}$$

$$= \frac{1}{6}(R - \frac{1}{R})(-sin\frac{2d}{\delta} + sin\frac{2d}{\delta} \cdot cosh\frac{2d}{\delta})$$

Combining equation B.53 and B.54 gives:

$$-\frac{1}{3}(R - \frac{1}{R})sin\frac{2d}{\delta} \tag{B.55}$$

Combining the founded equations of B.42, B.49, B.52 and B.55 gives the expression of equation B.56

$$\frac{1}{9}(R^2 + \frac{1}{R^2})(cosh\frac{2d}{\delta} - cos\frac{2d}{\delta}) \tag{B.56}$$

$$+\frac{1}{3}R(sinh\frac{2d}{\delta} - sin\frac{2d}{\delta}) + \frac{1}{3}\frac{1}{R}(sinh\frac{2d}{\delta} + sin\frac{2d}{\delta})$$

$$+\frac{1}{2}(cosh\frac{2d}{\delta} + cos\frac{2d}{\delta})$$

C

PROTOTYPE AND PLATE FIGURES

Figure C.1: Rectangular steel box of 200x200x120 mm

Figure C.2: Stainless steel plate of 230x125x2 mm

Figure C.3: Rectangular steel box under corona discharge test

Figure C.4: Stainless steel plate under corona discharge test

D

MATLAB CODES

D.1. SAGGING CURVE

```
1   %Matlab Code to simulate the effect of temperature increase and
2   %to the sagging curve
3   %Gert-Jan van Raamsdonk
4   %04-09-2017
5
6   %Parameters pf Aluminium conductor steel reinforced: 402-AL1/52-ST1A
7   A = 454.5;                % Conductor cross section [mm^2]
8   mc= 1.5205;               % Conductor mass per length [kg/m]
9   H = 123.75e3;             % Conductor tensile stress [N]
10  E = 68000;                % Conductor elasticity [N/mm^2]
11  et= 19.3e-6;              % Conductor linear expansion  [1/K]
12  g = 9.81;                 % Gravitational acceleration [m/s^2]
13  h = 32.5;                 % height supporters [m]
14
15  G = 0 ;                   % Concentrated load in the middle of the span [N]
16  T2= 100;                  % Conductor end temperature [degree Celsius]
17  T1= 50;                   % Conductor begin temperature [degree Celsius]
18
19  a1 = 300;                  % span length [m]
20  a2 = 500;
21  a3 = 200;
22
23  aeq = ((a1^3 + a2^3 + a3^3)/(a1+a2+a3))^0.5;
24
25  x1 = linspace(-a1/2, a1/2);
26  x2 = linspace(-a2/2, a2/2);
27  x3 = linspace(-a3/2, a3/2);
28  H1 = 0.2*H;
29
30  B1 = (E*A*(mc*g*aeq)^2)/(24*H1^2);
31  B2 = E*A*et*(T2-T1);
32
33  Q_term = (E*A*(mc*g*aeq)^2)/(24);
34  H2 = [1 (-H1+B1+B2) 0 -Q_term];
35
36  H2 = roots(H2);
37  H2 = real(H2(3));
38
39  f_1_original = mc*g*a1^2/(8*H1);
40  f_2_original = mc*g*a2^2/(8*H1);
41  f_3_original = mc*g*a3^2/(8*H1);
42
43  y_1_original = mc*g/(2*H1) * x1.^2;
44  y_2_original = mc*g/(2*H1) * x2.^2;
45  y_3_original = mc*g/(2*H1) * x3.^2;
46
47
48  f_1_new = (1/H2)*((mc*g*a1^2)/8 + (G*a1)/4);
49  f_2_new = (1/H2)*((mc*g*a2^2)/8 + (G*a2)/4);
50  f_3_new = (1/H2)*((mc*g*a3^2)/8 + (G*a3)/4);
51  mc_1_new = f_1_new/(g*a1^2) * 8*H2;
52  mc_2_new = f_2_new/(g*a2^2) * 8*H2;
53  mc_3_new = f_3_new/(g*a3^2) * 8*H2;
54  y_1_new= mc_1_new*g/(2*(H2)) * x1.^2  ;
```

```matlab
55  y_2_new= mc_2_new*g/(2*(H2)) * x2.^2  ;
56  y_3_new= mc_3_new*g/(2*(H2)) * x3.^2  ;
57
58
59  plot(x1+a1/2,y_1_original-y_1_original(1)+h,'b','LineWidth',2)
60  hold on
61  plot(x2+a1+a2/2,y_2_original-y_2_original(1)+h,'b','LineWidth',2)
62  hold on
63  plot(x3+a1+a2+a3/2,y_3_original-y_3_original(1)+h,'b','LineWidth',2)
64  hold on
65  plot(x1+a1/2,y_1_new-y_1_new(1)+h,'r','LineWidth',2)
66  hold on
67  plot(x2+a1+a2/2,y_2_new-y_2_new(1)+h,'r','LineWidth',2)
68  hold on
69  plot(x3+a1+a2+a3/2,y_3_new-y_3_new(1)+h,'r','LineWidth',2)
70  title('Sagging Curve')
71  xlabel('Distance x[m]')
72  legend('Original','','','New','','','','Location','southwest')
73  ylabel ('Distance y[m]')
74  grid on
75  ylim([0 35])
76  ax = gca;
77  ax.TitleFontSizeMultiplier = 3;
78  ax.LabelFontSizeMultiplier = 3;
```

D.2. CUSTOM SLOT ANTENNA

```matlab
1  %MATLAB code to simulate a custom slot antenna (Antenna Toolbox required)
2  %Gert-Jan van Raamsdonk
3  %23-08-2017
4
5  f = 868e6;                %Frequency [Hz]
6  c = 3e8;                  %Wave propagation speed [m/s]
7  feed_in = feed_in;        %[m]
8
9  %Fixed dimension stainless steel plate
10 steel_x = 23e-2;          %[m]
11 steel_y = 12.5e-2;        %[m]
12
13 %Dimension slot
14 wavelength = c/f;         %[m]
15 slot_x = wavelength/2;    %[m]
16 slot_y = wavelength/40;   %[m]
17
18 %Design slot antenna and ground place dimensions
19 space_from_top = 40e-3;   %[m]
20 space_from_bottom = steel_y-space_from_top-slot_y;
21 space_from_sides = 0.5*(steel_x-slot_x);
22 rec1 = em.internal.makerectangle(slot_x,slot_y);
23 rec1_m = em.internal.translateshape(rec1,[(0.5*slot_x+space_from_sides)...
24                                  (0.5*slot_y+space_from_bottom) 0]);
25 ground = em.internal.makerectangle(steel_x,steel_y);
26 ground_m = em.internal.translateshape(ground,[0.5*steel_x 0.5*steel_y 0]);
27
28 %Feed in location
29 feed = [(space_from_sides+feed_in) (0.5*slot_y+space_from_bottom) 0];
30 rec2 = em.internal.makerectangle(1e-3,slot_y);
31 rec2_m = em.internal.translateshape(rec2,feed);
32
33 %Combine slot antenna and ground plance
34 slot_antenna = customAntennaGeometry('Boundary',{ground_m',rec1_m',rec2_m'},...
35                                  'Operation','P1-P2+P3');
36 slot_antenna.FeedLocation = feed;
37
38 %Simulate S11 parameter
39 freq = (150e3:10e6:4000e6);
40 S11 = sparameters(slot_antenna, freq);
41 rfplot(S11);
```